EVALUATION OF THE EFFICIENCY INCREMENT POTENTIAL FOR FRANCIS TURBINES USING CFD ANALYSIS

A THESIS SUBMITTED TO
THE GRADUATE SCHOOL OF NATURAL AND APPLIED SCIENCES
OF
MIDDLE EAST TECHNICAL UNIVERSITY

BY

ARSLAN ÖMÜR ÖZCAN

IN PARTIAL FULFILLMENT OF THE REQUIREMENTS
FOR
THE DEGREE OF MASTER OF SCIENCE
IN
MECHANICAL ENGINEERING

SEPTEMBER 2016

Approval of the thesis:

EVALUATION OF THE EFFICIENCY INCREMENT POTENTIAL FOR FRANCIS TURBINES USING CFD ANALYSIS

submitted by **ARSLAN ÖMÜR ÖZCAN** in partial fulfillment of the requirements for the degree of **Master of Science in Mechanical Engineering Department, Middle East Technical University** by,

Prof. Dr. Gülbin Dural Ünver _____
Dean, Graduate School of **Natural and Applied Sciences**

Prof. Dr. Tuna Balkan _____
Head of Department, **Mechanical Engineering**

Prof. Dr. M. Halûk AKSEL _____
Supervisor, **Mechanical Engineering Department, METU**

Examining Committee Members:

Prof. Dr. Kahraman ALBAYRAK _____
Mechanical Engineering Dept., METU

Prof. Dr. M. Halûk AKSEL _____
Supervisor, Mechanical Engineering Dept., METU

Assoc. Prof. Dr. M. Metin YAVUZ _____
Mechanical Engineering Dept., METU

Assoc. Prof. Dr. Cüneyt SERT _____
Mechanical Engineering Dept., METU

Assist. Prof. Dr. Ö. Uğraş BARAN _____
Mechanical Engineering Dept., TED UNI.

Date:20.09.2016

I hereby declare that all information in this document has been obtained and presented in accordance with academic rules and ethical conduct. I also declare that, as required by these rules and conduct, I have fully cited and referenced all material and results that are not original to this work.

Name, Last name: Arslan Ömür ÖZCAN

Signature :

ABSTRACT

EVALUATION OF THE EFFICIENCY INCREMENT POTENTIAL FOR FRANCIS TURBINES USING CFD ANALYSIS

ÖZCAN, Arslan Ömür
M.S., Department of Mechanical Engineering
Supervisor : Prof. Dr. M. Halûk AKSEL

September 2016, 106 pages

Francis turbine is a widely used hydraulic turbine in hydropower plants. This thesis analyzes a Francis turbine using Computational Fluid Dynamics (CFD) analysis and offers an improved design in case of energy production. First the initial performance of the turbine is analyzed using CFD analysis, possible cavitation regions are evaluated and design point of the turbine is found using hill chart method and compared with the on-site efficiency measurement results. Then an optimization study is held to improve overall efficiency and the cavitation free working range. Energy production performances of the existing and new designed turbine are compared for 2 different rehabilitation scenarios. Calculations show that 2.84 percent increment in overall energy production and 2.2 percent increment in maximum efficiency is possible. Finally the method for rehabilitation is offered.

Keywords: Francis turbine, Hydroelectric, CFD, Optimization, Rehabilitation

ÖZ

FRANCİS TİPİ TÜRBİNLERİN VERİM ARTIŞ POTANSİYELLERİNİN HAD ANALİZİ İLE İNCELENMESİ

ÖZCAN, Arslan Ömür
Yüksek Lisans, Makina Mühendisliği Bölümü
Tez Yöneticisi: Prof. Dr. M. Halûk AKSEL

Eylül 2016, 106 sayfa

Francis türbini hidroelektrik santrallerde sıklıkla kullanılan bir hidrolik türbin tipidir. Bu tezde Francis tipi bir türbin Hesaplamalı Akışkanlar Dinamiği (HAD) analizi kullanılarak analiz edilmiş ve enerji üretim performansı açısından daha iyi bir tasarım önerilmiştir. İlk olarak mevcut türbinin performansı HAD ile analiz edilmiş, muhtemel kavitasyon bölgeleri belirlenmiş ve türbinin tasarım noktası tepe eğrileri kullanılarak bulunarak santralde yapılmış olan verim ölçümü sonuçlarıyla karşılaştırılmıştır. Daha sonra türbinin genel verimini artırmak ve kavitasyonsuz çalışma aralığını genişletmek için iyileştirme çalışması yapılmıştır. Mevcut türbinin ve yeni tasarlanan iyileştirilmiş türbinin enerji üretim performansları 2 farklı senaryo için karşılaştırılmıştır. Hesaplamalar toplam enerji üretiminde yüzde 2.84, en yüksek verim değerinde ise yüzde 2.2 artış göstermiştir. Son olarak yenileme çalışmaları için bir yöntem önerilmiştir.

Anahtar Kelimeler: Francis türbini, Hidroelektrik, HAD, Optimizasyon, Rehabilitasyon

To My Beloved Family

And My Friends

ACKNOWLEDGEMENTS

I would like to express my deepest pleasure to my supervisor Prof. Dr. M. Halûk AKSEL, for his useful supports, comments, advices and their guidance throughout this master thesis.

I wish to express my gratitude to the team of Institute of Hydraulic Fluid Machinery TU GRAZ, especially to Prof. Dipl.-Ing. Dr. techn. Helmut Benigni, Prof. Dipl.-Ing. Dr.techn. Helmut JABERG and Dipl.-Ing. Dr.techn. Jürgen SCHIFFER for their support and understanding.

I also wish to express my deepest gratitude to my family and friends for their support, love and courage.

Finally, yet importantly, I wish to thank all my colleagues in Electrical Power Technology Group of TÜBİTAK MAM Energy Institute, for their support, friendship and the great working environment.

TABLE OF CONTENTS

LIST OF FIGURES

FIGURES

LIST OF TABLES

TABLES

NOMENCLATURE

g	Gravitational acceleration (m/s^2)
n	Rotational speed (rev/s)
p	Pressure (bar)
p_a	Atmospheric pressure (bar or Pa)
p_v	Vapor pressure (bar or Pa)
t	Time (s)
C	Absolute velocity (m/s)
C_m	Meridional absolute velocity (m/s)
C_u	Angular absolute Velocity (m/s)
E	Specific Hydraulic Energy (J/kg)
H	Head (m, bar or Pa)
N	Rotational speed (rev/min)
NPSE	Net positive specific energy (J/kg)
P	Power (W)
Q	Flow rate (m3/s)
R	Radius (m)
Re	Reynolds number
T	Torque (Nm)
U	Peripheral velocity (m/s)
W	Relative velocity (m/s)
β	Blade angle (˚)
γ	Distributor opening angle (˚)
ω	Rotational speed (rad/s)

ψ	Specific energy coefficient (J kg^{-1})
σ	Thoma number
μ	Dynamic viscosity (kg/ms)
η_h	Hydraulic efficiency
ρ	Density (kg/m^3)
ν	Specific Speed (kg/m^3)

CHAPTER 1

INTRODUCTION

Hydroelectric power has an important role in Turkey's energy production. New Hydro Power Plants still being constructed and the old plants are under rehabilitation.

A hydro power plant has two main characteristics effecting the turbine design, head and discharge. [**12]** Because of this for each power plant a new turbine has to be designed. In this thesis optimization of an existing turbine is issued. The existing geometry is taken by laser scanning technology and using Computational Fluid Dynamics analysis, performance of the existing turbine is evaluated and detailed explanations are given in Chapter 2. Modifications for optimization started over the existing geometry and 25 different versions are created to reach the optimum design. Details of optimization studies are given in Chapter 3.

In Figure 1.1, overview of a hydropower plant is shown. In a hydro power plant, water is stored in a reservoir. Size of the reservoir depends on the design of the dam and geological conditions. Main purpose of the reservoir is to collect to water from different rivers and store it when necessary. Also, incoming water needs to rest for some period for sediments to settle. These sediments can damage the turbine runner in long term due to particle erosion. Collected water is transferred into the penstock which is a steel pipe carrying the water through the turbine. Just before the turbine there is a valve, which is able to stop the flow when necessary. After the valve water gets into the spiral case. Spiral case has a narrowing geometry which provides equal flow velocity and pressure at the stay vanes inlet. Stay vanes are constant pitch blades and their main purpose is to transfer the water through guide vanes equally distributed and to provide structural strength to the spiral case. After passing

through the stay vanes, water goes into the guide vanes. Guide vanes are varying pitch blades. Discharge and power of a Francis turbine can be altered by changing the guide vane angles. Runner is the rotating part. Water generates torque on the runner and with the turbine shaft this torque is transferred to generator to generate electrical power. Draft tube is a diverging pipe after the runner. The main purpose of the draft tube is to diffuse the water and transfer it to the lake or river.

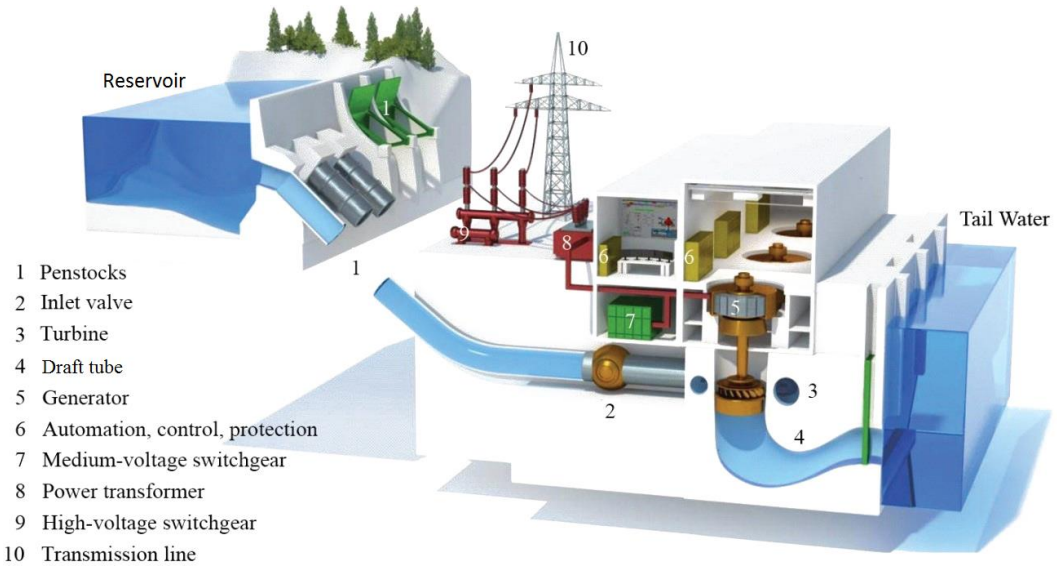

Figure 1.1 : Overview of a hydropower plant

In Figure 1.2, parts of Francis turbine are shown. The necessary parts for CFD analyses are as follows : 1-Spiral Case, 2-Stay Vane, 3-Guide Vane, 5-Suction Flange, 6-Upper Ring, 7-Bottom Ring, 8-Draft Tube Cone, 9-Draft Tube Wall, 10-Runner, 11-Runner Blade, 12-Hub, 13-Shroud, 14-Runner Cone, 18-Turbine Shaft.

The rest of the parts are given informatively which are : 4-Turbine Cover, 15-Flange, 16-Cover Ring, 17-Support Ring, 19-Joint Flange, 20-Guide Bearing, 21-Guide Bearing Cover, 22-Labyrinth Seal, 23-Guide Vane Bearing, 24-Guide Vane Bearing Sealing, 25-Lever, 26-Lever brake protection, 27-Regulation Ring, 28-

Servomotor Rod, 29-By-pass, 30-Drainage Pipe, 31-Leakage Water Drainage, 32-Oil Supply, 33-Oil Discharge, 34-Runner Gap

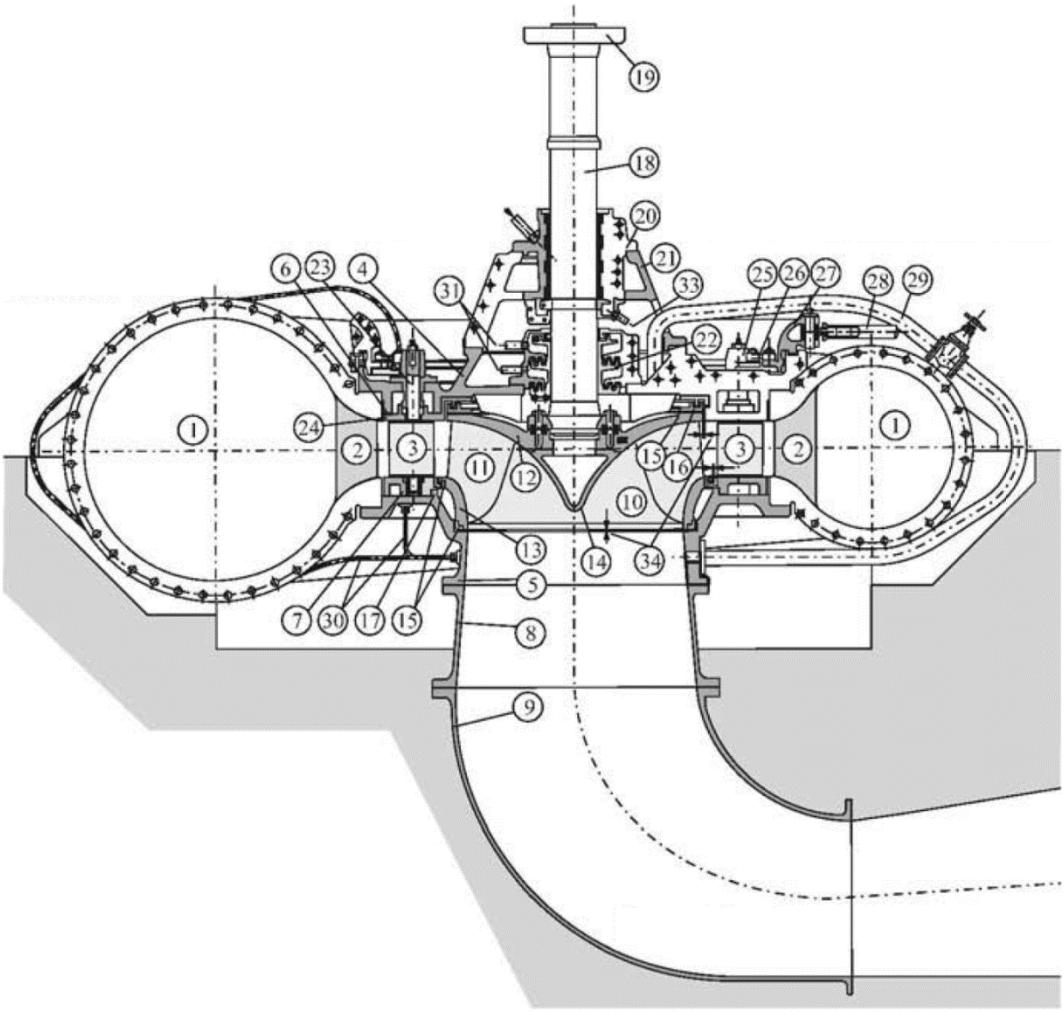

Figure 1.2: Francis turbine parts [13]

1.1 Literature Review

The literature about the Francis turbines can be separated into two topics which are: early design studies and modern design studies. Early design studies has started with the empirical equations which defines the main dimensions and flow parameters of the turbines. These equations are based on the model test results of many turbines. Many different designs are tested and compared with each other and main dimensions are related to the empirical formulas for different specific speeds. Flow is assumed to be ideal, incompressible and inviscid. The 2D view of the turbine, also called meridional view, is used for the initial design phase and Euler equations are applied on the meridional geometry.

Prof. Th. BOVET [5] has generated an equation to calculate the hub and shroud curves and also the leading and trailing edges of the runner. These curves which are shown in Figure 1.3 can be taken as the initial geometries for further improvement. There are also formulas for each of the parameters shown in Figure 1.3. The shape of the meridional contour depends on the specific speed of the turbine and in the paper there are several meridional contour examples for different specific speeds.

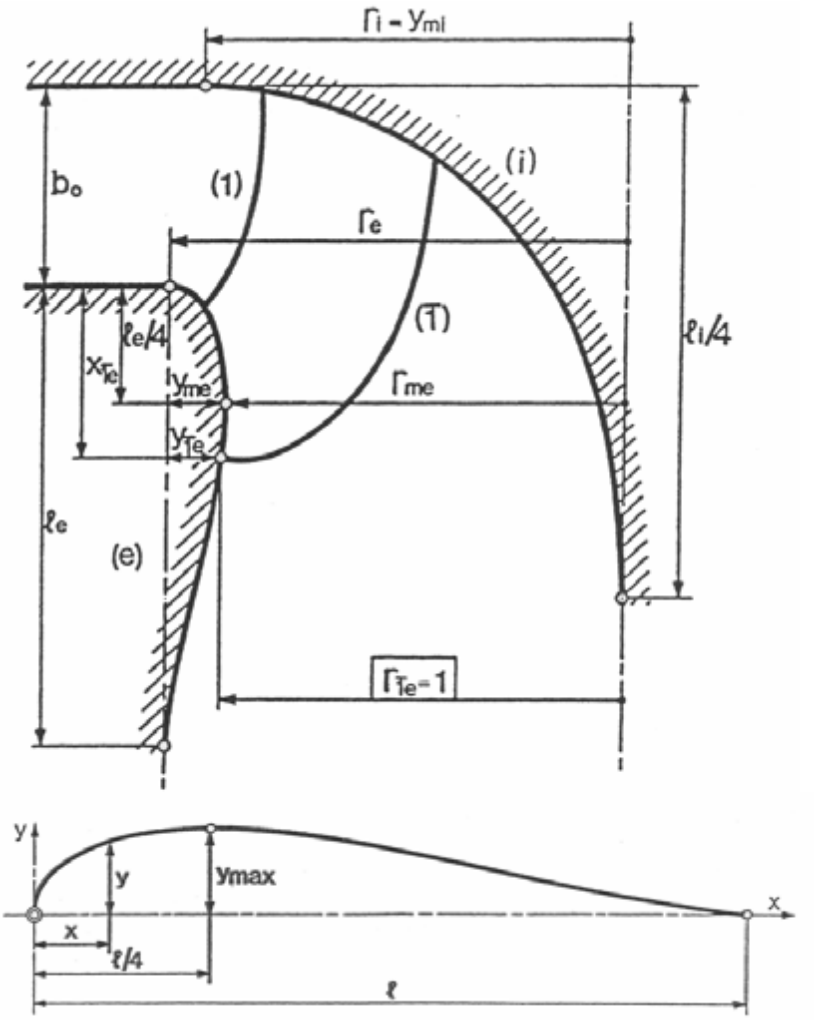

Figure 1.3 : Meridional view parameterization of a Francis turbine [5]

Prof. De Siervo and Prof. De Leva [1] also performed more than 100 Francis turbine model tests and offered some empirical formulas for calculation of meridional contour based on the specific speed of the turbine. All the dimensions are referred to the outlet diameter of the runner and outlet diameter is calculated using the discharge (*Q*) and rotational speed (*w*) of the runner.

Prof. L. Quantz [2], Prof. L. Vivier [3] and Prof. P. Henry [4] have also their own empirical formulas for meridional contour dimension calculations. Each of these 5 design methods starts with defining the meridional contour and calculation of the

blade area using Euler equations. After determining the meridional contour sizes and shapes, blade design starts. First the inlet and outlet β angles are calculated using Euler equations and velocities in each 3 directions are calculated assuming infinitely thin blades. Next the streamlines are calculated on the meridional contour and for a defined number of blades the blade thickness effect on the flow area is taken into account. Finally, the 3D geometry of the blades are generated using conformal mapping transformation. These 3D geometries are manufactured and tested on the models test stands and iteratively the final shape of the turbine is reached. Model testing of the each version is very time consuming and also very expensive. Nowadays this iterative process is fastened and simplified using CFD and optimization techniques.

In 1990's a Norwegian Professor H. Brekke [27] has offered a new design method called X-blade design. The design is tested and used in the world biggest hydropower plant Three Gorges Dam. Fundamentals of this design are still in use. Details on this design method are given in Chapter 3.3.2.

With the help of the computer technology it is now possible to automatically generate different new designs for specified parameters and analyze these designs using computer software instead of model testing. There are some different methods for designing the turbine blades such as Bezier curves [7-8], B splines and NURBS [10-11]. Genetic algorithm is also used for generating new design versions using the analysis results [6]. These parametric geometry definitions give an opportunity to generate smooth and precise 3D models of the blades. It is also possible to transform these geometries to widely used 3D modeling formats such as STEP, IGS, etc.

1.2 Motivation

The new trend in hydro turbines is the rehabilitation studies due to the fact that a hydro power plant has average of 50 years lifetime. After this lifetime a rehabilitation study is necessary for both safe operation of the turbine parts and the better turbine performance with the new design methods. The main motivation of

this thesis is: to analyze the existing turbine performance, detect the faults and improving it by a new design. This provides an efficiency increment and it can provide wide and cavitation free operation range for the turbines resulting more energy generation and long operation years.

For this study, an actual power plant is considered according to the demand from Turkish Electricity Generation Company. Outcome of this study is the improved turbine design for this power plant and its energy production calculations which to be used in feasibility calculations.

1.3 Information about the power plant

The hydropower plant is located in Tarsus/Mersin. It was built from 1970 to 1973 and consists of one Francis turbine with 56 MW of power. The turbine built by Escher Wyss which is now belongs to Andritz Hydro. Power plant has a reservoir size of 1.000.000 m^3 and open to a horizontal tunnel with a length of 6253 m. A surge tank is installed to prevent water hammer and it is followed by a steel penstock with a length of 345 m. Turbine nominal diameter is 2.58 m with a flow rate of 48 m^3/s. Power plant has an average annual production of 184.6 Mio. kWh in the last 10 years.

In April 1974, cavitation damages detected on the turbine blades after 1200 hours of operation. There is a triangle area between runner shroud and trailing edge in the direction of the flow approx. 50 mm with a depth of approximately 3 mm. A second area could be detected as well with a lower depth. At that time, the tail water level (H=58.75m) was lower than expected in part-load operation.

In May 1974, after preliminary efficiency tests, modifications regarding the hydraulic shape of the turbine had to be considered. This examination revealed that the nose-plate area of the spiral case due to the narrow cross-section at stay vane number 23 (last but one before the nose plate) the flow was substantially retarded. After modifications the witness test was carried out once again. The resulting efficiency was 1.6% lower than the guaranteed value (measurement inaccuracy +/-

1.5%). In 1983, a runner change was carried out and cavitation damages were detected during an inspection. Furthermore, an aeration device was mounted downstream the runner to improve turbine's suction performance. In 2007, comprehensive measurements were carried out by SOCOIN. In 1984, another power plant is constructed downstream of this power plant and the tail water lever is increased to 66.9 m from 59 m. This level change increased the outlet pressure of the draft tube and the aeration device was not necessary anymore. Aeration device is shut off since then. However the stand pipe remained in the draft tube.

1.4 Cavitation

Francis turbines have fixed runner blades, so no pitch change is possible and rotational velocity of the runner is also constant. At different operating conditions discharge of the flow changes, so inlet and outlet flow angles varies on runner blades. That causes a complex flow phenomenon called cavitation. Cavitation is a dangerous flow phenomenon in hydraulic turbines and has to be analyzed carefully during design studies. In Chapter 1.4 cavitation in Francis turbines is explained in detail.

When an area in the liquid is exposed to a pressure lower than the vapor pressure, liquid transforms to gas phase and it forms cavities [14] subsequently it is exposed to higher pressures so gas bubbles collapses and generates shockwaves [15].This phenomenon is called cavitation and it has a very important role in both safe and efficient operation of hydraulic turbines.

Unsteady cavity generations cause pressure oscillations with low frequencies and collapsing of cavity bubbles produces high frequency pressure pulses. These pressure oscillations and pulses yields to flow instabilities, severe vibrations, material surface damages and deterioration of turbine performance. Different parts of hydraulic turbines are exposed to cavitation such as runners and draft tubes of Francis, Kaplan, Bulb and Pump turbines, also buckets, nozzles and needles of Pelton turbines.

The knowledge of cavitation phenomena in hydraulic turbines is always valuable. The first reason is, manufacturers intend to reduce the manufacturing costs by scaling down the turbine sizes, consequently the flow speed in the turbine increases and cavitation number decreases. Second reason, hydro power plants with small reservoirs or without any reservoir (run-off river type) intend to use the whole available power and operate mostly at part-load, also plants with dam sometimes prefers to operate at part-load to generate profit from the energy market. But cavitation mostly reveals at part-load regimes.

Cavitation is hardly fixable at existing units so required care has to be taken at the design phase. Runner design has a very important role on cavitation performance of turbines. Also the selection of turbine setting level and part-load flow conditions has to be concerned.

1.4.1 Cavitation in Francis Turbines

There are 5 different types of cavitation behavior in Francis turbines, which are mainly related to the head coefficient (ψ) and flow coefficient (φ) [16].These cavitation behaviors are described below.

- **Leading edge cavitation**

Leading edge cavitation is an attached cavity, forms at both sides of blade leading edge. If the turbine operation head is higher than the design head (high ψ), a positive incidence angle at the blade inlet causes leading edge cavitation at the suction side of the blade as it is shown in Figure 1.4 **[17]**. If the turbine operation head is lower than the design head (low ψ), a negative incidence angle at the blade inlet causes leading edge cavitation at the pressure side of the blade. Thoma cavitation number (σ) doesn't have much influence on this type of cavitation and it is very dangerous because it has strong erosive power and it can prompt pressure fluctuations especially when it is unstable.

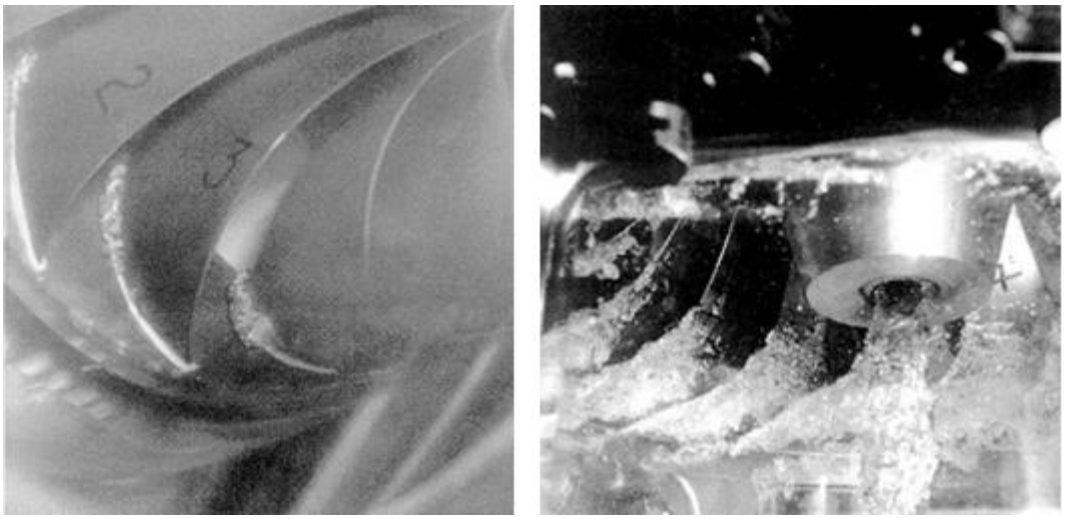

Figure 1.4 : Leading Edge Cavitation (left), travelling bubble cavitation (right)

- **Travelling bubble cavitation**

Unlike the leading edge cavitation, travelling bubble cavitation occurs at the design head of the turbine. It is strongly dependent on the cavitation nuclei content and the plant Thoma cavitation number (σ_p) and it occurs at low σ_p. Cavitation amount advances with increasing discharge and is reaches maximum level at full load (over load). Due to this fact, Net Positive Suction Energy (NPSE) of plant is selected based on this cavitation type. It is seen at the middle of suction side of the blade close to the trailing edge as shown in Figure 1.4 **[18]**. It is a strong and noisy cavitation type and the most important effect is the reduction in efficiency. It also causes erosion on blades.

- **Vortex Rope at Draft tube**

Vortex rope occurs below the runner down to the draft tube. Depending on the flow coefficient, it can have a helical or axially centered shape. At part load it takes a helical shape and it rotates in the same direction as the runner. At over load it takes axially centered shape and it rotates at the opposite direction of the runner rotation. Model test visualizations of these vortices are given in Figure 1.5 **[19]**. The changes

in the volume of the vortex rope are based on the σ_p value. At part load fluctuations can cause strong pulsations especially when the rope frequency (0.25 to 0.35 times the runner rotation speed) matches with draft tube or penstock natural frequency **[20]**.

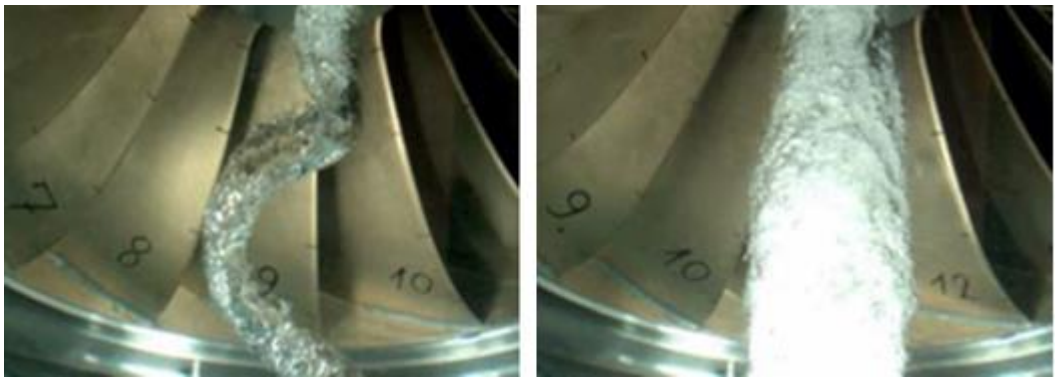

Figure 1.5 : Vortex Rope at part load (left), at over load (right)

- **Inter blade vortex**

At low flow coefficient values or very high operation heads, angular difference of hub and shroud geometries causes flow separation between runner blades and generates secondary vortices. Vortex generation starts at the hub side of the leading edge or in the middle of the hub between runner blades and extends to the runner outlet region. It has an erosive power if the tip of the vortex is on the blade at very high heads it is unstable and causes vibrations. Model test visualization of this vortex type is given in Figure 1.6 **[21]**.

Figure 1.6 : Inter Blade Vortex

- **Von Karman vortex cavitation**

Trailing edge geometry is very effective on this type of vortex generation. If not designed carefully, periodic vortex shedding can happen at the trailing edge with pressure pulsation and noise and can have a damaging effect. Operating limits that we can avoid these cavitation types are plotted in a single hill chart and given in Figure 1.7. Number ① refers to limit of leading edge cavitation at suction side of blade, number ② refers to limit of leading edge cavitation at pressure side of blade, number ③ refers to cavitation limit of interblade vortex and number ④ refers to limit of draft tube vortex rope.

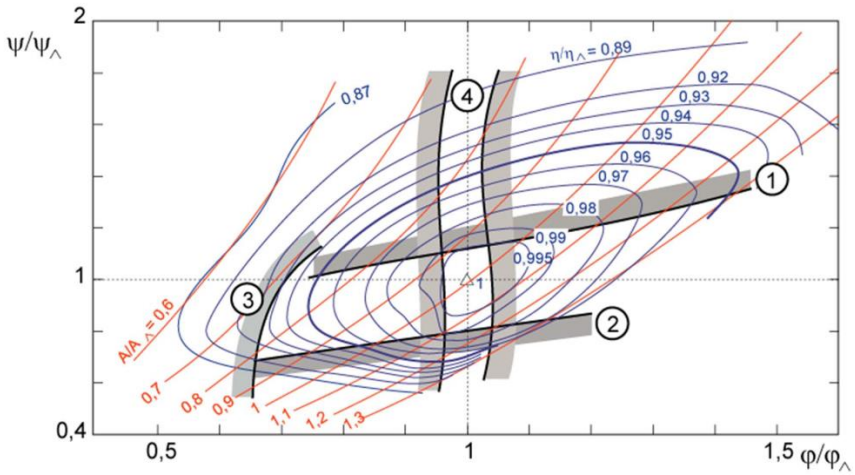

Figure 1.7 : Cavitation limits on a hill chart

CHAPTER 2

PERFORMANCE EVALUATIONS

In this chapter, 3D modelling of the existing turbine is described, then CFD analyses study is performed to evaluate the performance of the existing turbine. 3D geometry of the existing turbine is modeled using the Faro scan arm laser scanning device and the metrology software Polyworks. Existing turbine geometry is analyzed using commercial CFD program ANSYS CFX. In all analyses steady state model is used. ANSYS Meshing, ANSYS Design Modeler, ANSYS Icem CFD and CFX Solver are used for all CFD analysis steps.

2.1 CAD Model

3D geometry of the existing turbine was not available in the power plant archives, since turbine manufacturers tend to protect their know-how. There is a spare part turbine runner and guide vanes available in the power plant. These spare runner and guide vanes are used for laser scanning studies.

Faro Scan Arm laser scanner has a single point tolerance of 0.029 mm and volumetric tolerance of +/- 0.041 mm. Considering the runner diameter of 2.58 m, this tolerance values are acceptable. Polyworks software is coupled with the laser scanner and gives 3D visualization during the scanning. The outcome of the scanning is the point cloud and when the geometry is big, there will be millions of points and that use so much memory and is should be simplified after the scanning. When the scanning is done, it is possible to mesh the surface with tetragonal cells to simplify the data. When the scanning angle is too narrow and there is no possibility to reach all of the areas, some holes appears in the scanned data. In

Polyworks it is possible to fill these holes according to the surrounding surfaces. This final data is exported in STL format to CAD programs.

In Figure 2.1 the scanned guide vane is shown. Scanning the whole guide vane geometry is not necessary since it has a constant geometry in whole span. Using this scan data, a 2D coordinate file is generated and used for 3D modeling of the guide vane.

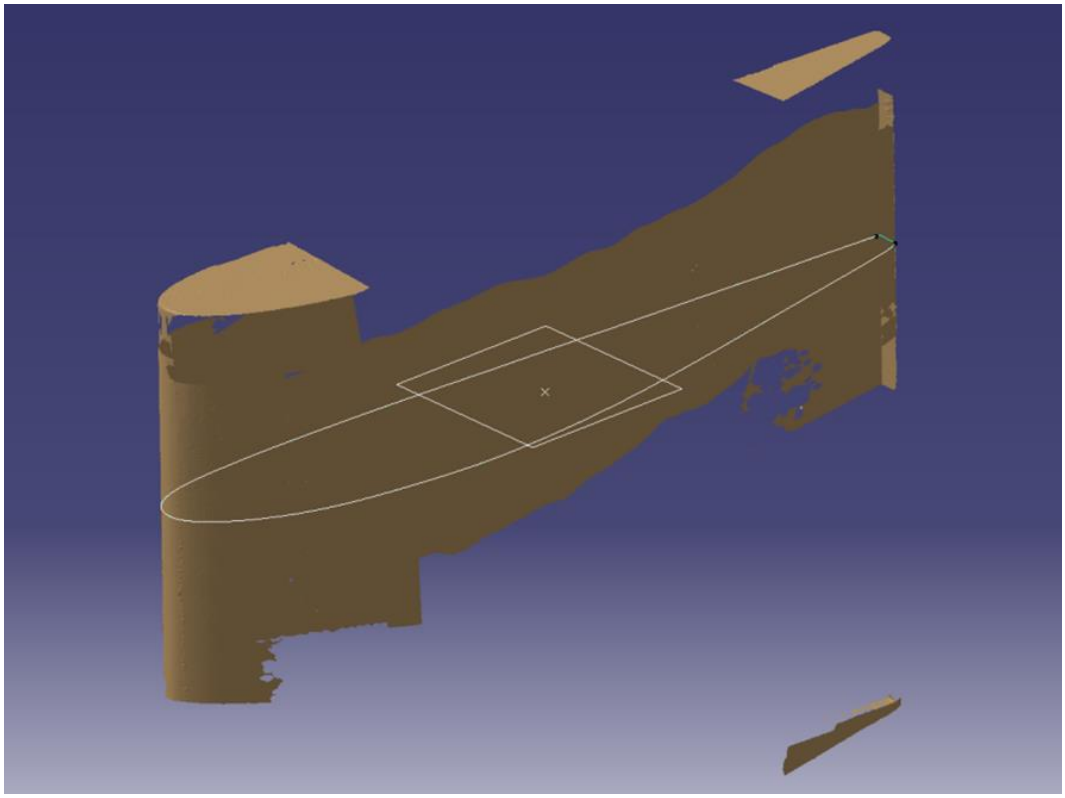

Figure 2.1 : Guide vane scan in STL format

This coordinate information is imported in a CAD program and the blade is moved to the correct diameter and angle. The fully closed guide vane angle is found using the CAD program as is it shown in Figure 2.2. Fully closed position is where the guide vane blades are touched to each other. This is a necessary condition in a power plant because stopping the flow in the turbine should be possible by closing the guide vanes. The turbine inlet and outlet valves are not able to directly stop the flow but guide vane is.

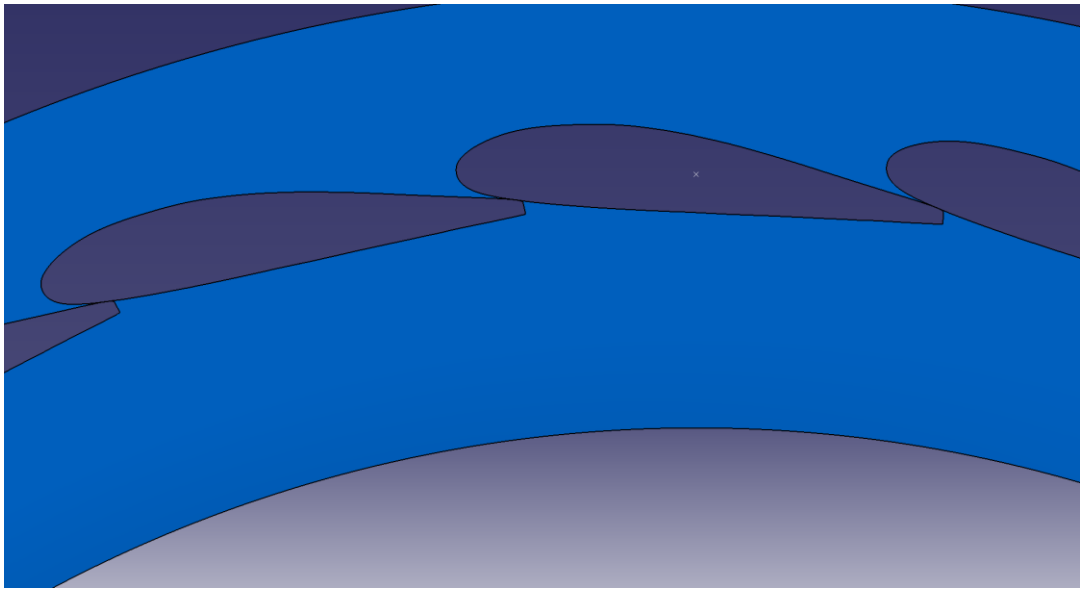

Figure 2.2 Guide vane closed position

Runner blades are also scanned with the same laser scanner. The difference is, for the runner 3 different blades are scanned and compared with each other. In 1970's manufacturing of the turbine was not as precise as it is now. So there might be some manufacturing differences. In Figure 2.3 comparison of 3 different blades are given. Blue, pink and yellow colors represent different blades that are scanned and moved over each other. Laser scanner has a 1.4 meter long scan arm with 3 joints, but it is still not possible to move between the blades and scan the whole surface. Due to the fixing point of the laser scanners tripod, it was not possible to scan the exact same areas of the blade. Comparison of these 3 different scans shows that there are maximum of 5 mm difference between the blades at some small regions. Since there is no detailed drawing of the runner, it is not possible to evaluate the correctness of the blades. Finally the blade that has the largest scanned area is selected for 3D modeling.

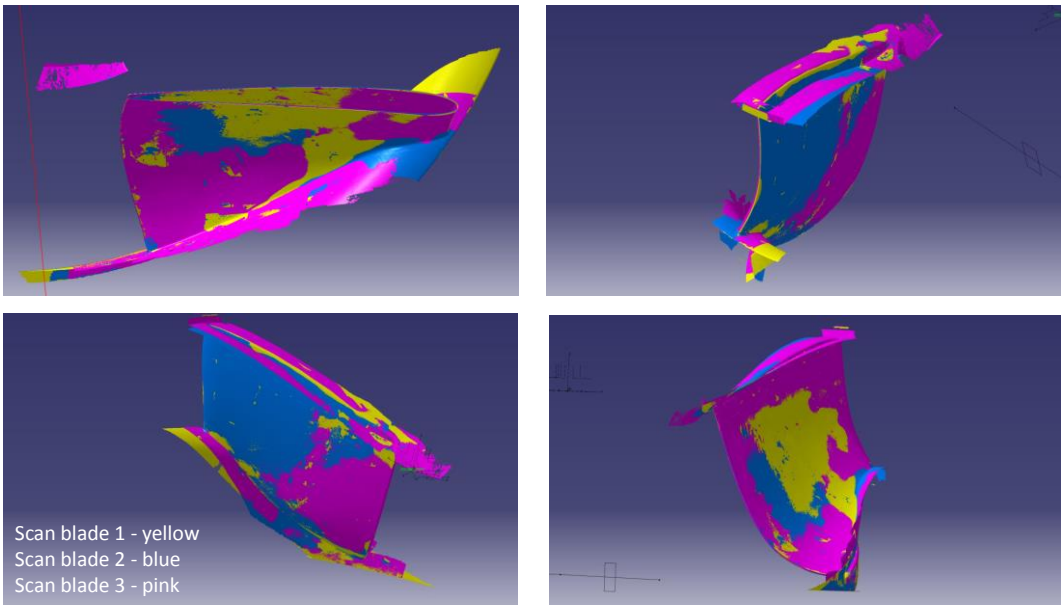

Figure 2.3 : Runner blades scan comparison

In Catia, turbo surfaces were generated for 22 different spans which are shown in Figure 2.4. First 22 different curves are drawn between runner hub and shroud. These curves basically follow the hub and shroud geometries and divide the area equally in between hub and shroud. Then these curves are revolved around turbine rotation axis to get surfaces. Runner blades are intersected with these surfaces and cross section is a 3D curve for each turbo surface. These curves are exported as coordinate files.

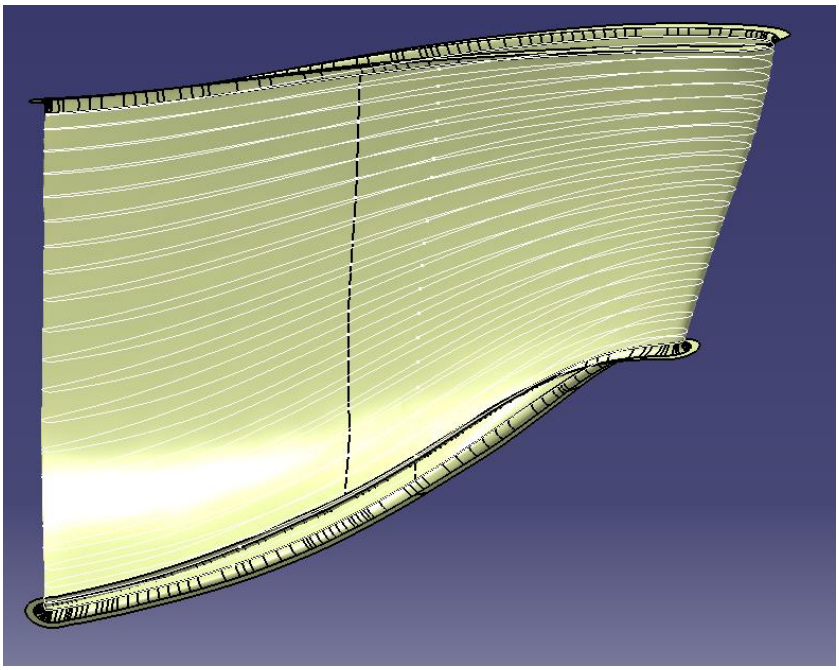

Figure 2.4 : Intersection of the runner blade and turbo surfaces

For spiral case, stay vanes and draft tube, basic geometric measurements are held with laser meters and tape measure. Measurements are in good correlation with the technical drawings so geometries are modeled according to the technical drawings.

2.2 Mesh Generation

In Figure 2.5 (left) the guide vane passage mesh block is shown and on the right side of Figure 2.5 the runner grid block is shown. Furthermore, the mesh statistics for each mesh are displayed in these figures. In general, for CFD calculation purposes the free volume between the blades has to be modelled and a fine mesh density is needed in regions with expected high gradients of variables (e.g. velocity and pressure). So, fine grid density close to the walls (inflations) like hub and shroud and of the blade itself is required.

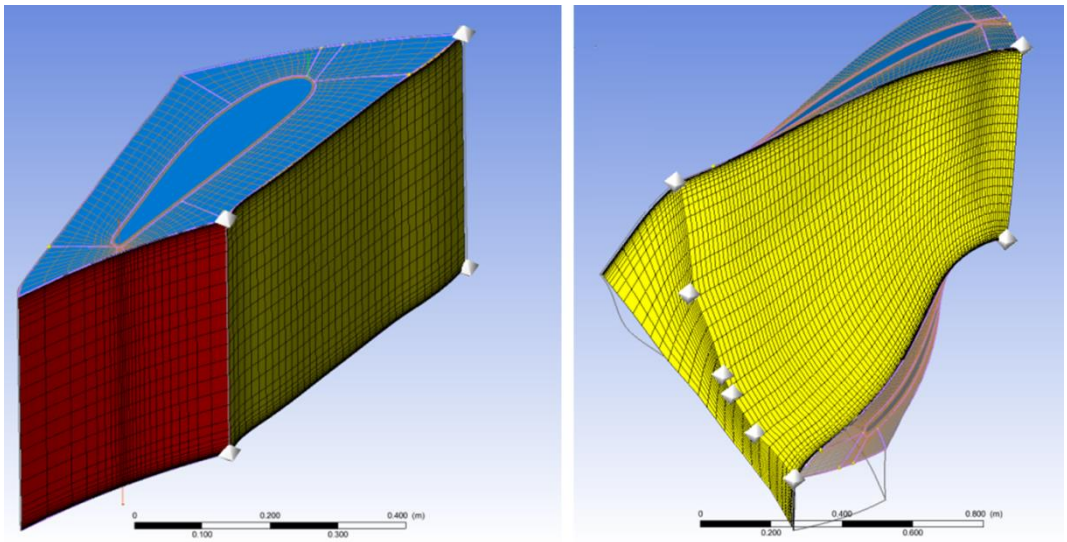

Figure 2.5 : Guide vane and runner mesh generation using Turbogrid

The mesh generation for guide vane and runner is carried out in Turbogrid ® in a structured way.

In order to avoid highly skewed elements at the leading edge of the blade, Turbogrid® mesh-generation was applied in the HJCL mode. The HJCL mode follows a so-called automated block topology depending on the blade wrap angle that includes full periodicity and applies an algebraic, semi-isogeometric surface mesh generation procedure.

In Figure 2.6 (left) the block structure for the draft tube is shown. The structure is a double butterfly (O-grid) in the cross section whereas this structure is segmented in streamwise direction at every elbow segment. For the stand pipe an additional O-grid must be set around the pipe, which is shown in Figure 2.6 (right).

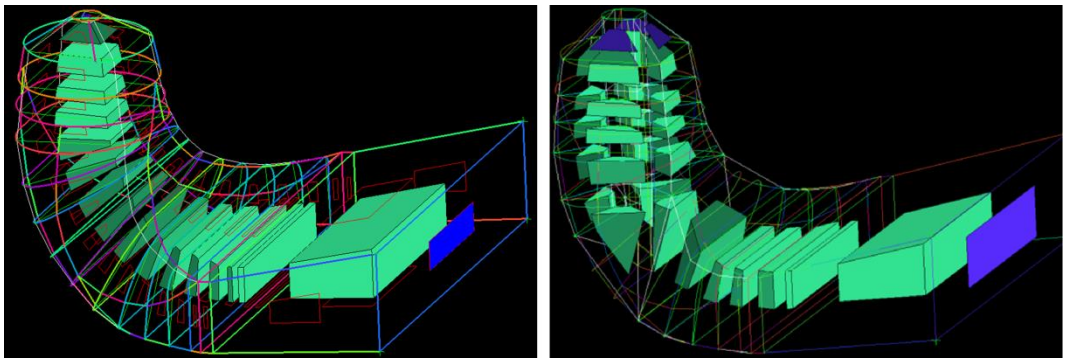

Figure 2.6 : Draft tube mesh generation in ICEM®, structured mesh, block structure (left), surface mesh (right)

The spiral domain was meshed with ICEM® in an unstructured mode and is shown in Figure 2.7.

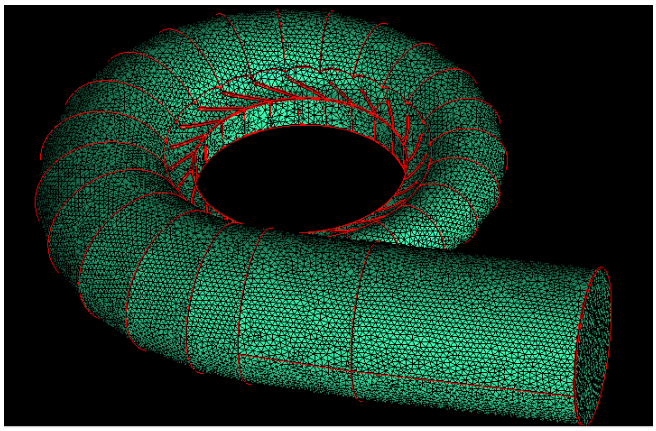

Figure 2.7 : Spiral Case mesh generation, ICEM ® unstructured mesh

Finally, the outblock mesh was generated block-structured in ICEM as well. Statistics of the generated meshes for the guide vane are displayed in Table 2-1 for 3 different mesh densities.

2.2.1 *y*+ values of the mesh

In general, there are two methods for the calculation of the boundary layer flow situation.

Low-Reynolds-Number method:

The mesh in the boundary layer region gets such a fine density that nodes are available in the viscous sub-layer. For the *y*+ value of the nearest node to the wall a value of around *y*+ = 1 is requested. In Figure 2.8 boundary layer regions are described. For fluid situations with high Reynolds numbers, the viscous boundary layer is extremely thin. So, the amount of nodes is very high and the cells in that region become very flat (high aspect ratios) and thus convergence is worse.

Wall function method:

With this method, empirical equations are used to model the viscous boundary layer and the transition layer area. Therefore, a higher y^+ value is requested and less mesh inflations are needed. These wall functions need a y^+ value of at least $y^+ = 30$, because the closest node to the wall has to lay inside the turbulent outer layer region (inside the region with the logarithmic law).

Automatic wall treatment:

CFX offers the possibility/option to use a hybrid model: "the automatic wall treatment". For the regions where the mesh resolves the viscous sub-layer, the low Reynolds model is applied, and for the other regions the logarithmic wall functions are used. Thus, the y^+ value of the meshes is of minor importance. For the simulation of this Francis turbine structured meshes of the runner, guide vane and draft tube region were used with good element angles and aspect ratios for all regions.

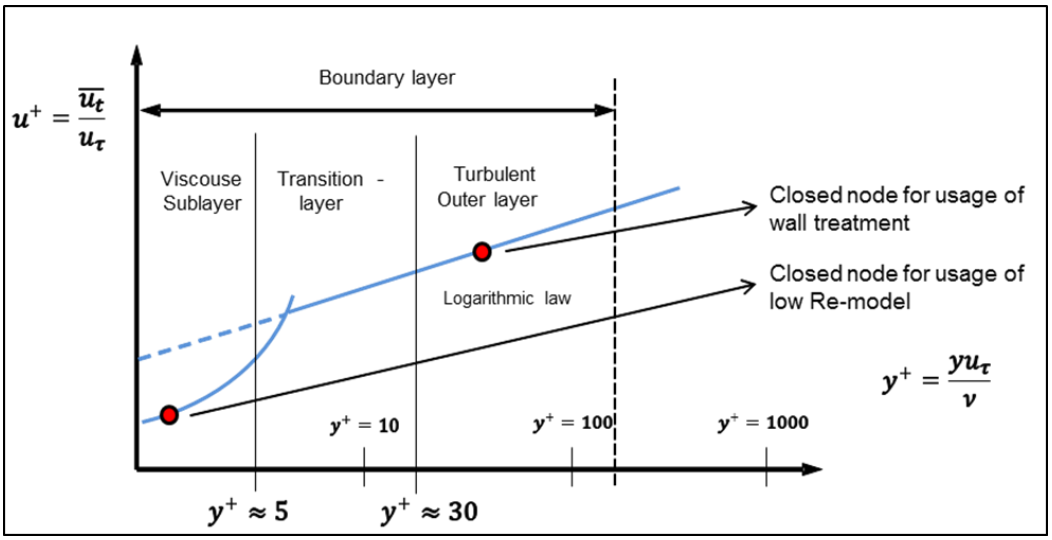

Figure 2.8 : Boundary Layer region

The changes in the mesh generation settings concerning *y*+ and numbers of layers are also included in this table. The same data can be found in Table 2-2 for the runner passage. The highest value is about *y*+ = 37 for the fine grid and occur at the runner – draft tube interface at the shroud.

Finally, the statistics for the full model of the total machine are presented in Table 2-4. Models with up to 33 million nodes were generated. In this table, in the upper part the nodes are displayed in millions and the elements are displayed in millions in the lower part of the table.

Table 2-1 : Mesh statistics for guide vane passage

Opening	Fine Mesh						
[degrees]	No. Of nodes	No. of elements	No. of layers near wall	Spanwise Elements	O-grid width factor	Min/Max Face Angles	Max. edge length ratio
5.00	220044	204880	10	65	0.05	7.5° / 173.5°	15000
7.50	257400	241410	10	65	0.1	8° / 182°	12000
10.00	238590	223470	10	65	0.1	11° / 169.5°	13000
12.50	231264	216450	10	65	0.1	19° / 160.5°	13000
15.00	231264	216450	10	65	0.1	23.5° / 155.5°	13000
17.50	216414	203190	10	65	0.1	21.5° / 157°	9000
20.00	216414	203190	10	65	0.1	28.5° / 150.5°	9000
22.50	220968	20748	10	65	0.1	32.5° / 147°	9000
25.00	225522	211770	10	65	0.1	28.5° / 156.5°	9000
27.50	225522	211770	10	65	0.1	18° / 166°	9000
Opening	Medium Mesh						
[degrees]	No. Of nodes	No. of elements	No. of layers near wall	Spanwise Elements	O-grid width factor	Min/Max Face Angles	Max. edge length ratio
5.00	203374	189120	10	60	0.05	7.5° / 174°	8000
7.50	128588	119040	10	60	0.1	12.5° / 169.5°	6000
10.00	119926	110880	10	60	0.1	15.5° / 164.5°	6000
12.50	116876	108000	10	60	0.1	21.5° / 157.5°	7000
15.00	116876	108000	10	60	0.1	26° / 152°	7000
17.50	108458	100560	10	60	0.1	26° / 151°	5000
20.00	108458	100560	10	60	0.1	33° / 145.5°	5000
22.50	110776	102720	10	60	0.1	36° / 151.5°	5000
25.00	113094	104880	10	60	0.1	27.5° / 160.5°	5000
27.50	113094	104880	10	60	0.1	19.5° / 168°	5000
Opening	Coarse Mesh						
[degrees]	No. Of nodes	No. of elements	No. of layers near wall	Spanwise Elements	O-grid width factor	Min/Max Face Angles	Max. edge length ratio
5.00	139380	128160	8	45	0.05	7.5° / 174°	4000
7.50	71668	64980	8	45	0.15	10° / 170.5°	4000
10.00	69552	63000	8	45	0.15	16.5° / 164°	4000
12.50	67436	61020	8	45	0.15	21.5° / 157°	4000
15.00	57684	52380	8	45	0.15	21° / 161°	3000
17.50	59064	53640	8	45	0.15	26° / 154.5°	3000
20.00	59064	53640	8	45	0.15	30° / 148.5°	3000
22.50	60444	54900	8	45	0.15	36° / 143°	3000
25.00	67620	61920	8	45	0.15	25° / 166°	2000
27.50	77004	70560	8	45	0.15	26° / 161.5°	3000

Table 2-2 : Mesh statistics for runner passage

Mesh Density	No. Of nodes	No. of elements	No. of layers near wall	Spanwise Elements	O-grid width factor	Min/Max Face Angles	Max. edge length ratio
Coarse	120258	108900	8	50	0.25	8.5° / 173.5°	3000
Medium	227436	210600	10	65	0.2	14° / 167.5°	4000
Fine	400824	375300	10	75	0.2	18° / 166°	5000

Table 2-3 : Mesh statistics for draft tube

Mesh Density	No. Of nodes	No. of elements	No. of layers near wall	Height ratio
Coarse	557568	543781	10	1.35
Medium	1202696	1179748	10	1.25
Fine	2507436	2471284	12	1.2

Table 2-4 : Mesh statistics for full model

	Very Fine	Fine	Medium	Coarse
Domain	No. Of Nodes (millions)	No. Of Nodes (millions)	No. Of Nodes (millions)	No. Of Nodes (millions)
Draft Tube	5.68	4.04	1.59	0.95
Guide Vane	9.46	5.19	2.6	1.42
Runner	11.59	6.81	3.87	2.04
Spiral Case	6.39	2.75	1.33	0.93
Total	33.13	18.8	9.39	5.33
Domain	No. Of Elements (millions)	No. Of Elements (millions)	No. Of Elements (millions)	No. Of Elements (millions)
Draft Tube	5.59	3.96	1.55	0.92
Guide Vane	8.97	4.88	2.41	1.29
Runner	10.95	6.38	3.58	1.85
Spiral Case	18.33	8.4	3.98	2.76
Total	43.84	23.62	11.53	6.81

2.3 Pre-Processing

With the help of the commercial CFD code Ansys CFX the Navier-Stokes equations were solved. These Navier-Stokes equations describe the fluid motion in all three dimensions and were used with a Reynolds averaged Navier stokes (RANS) formulation. RANS uses equations where the instantaneous variables are decomposed into mean and fluctuating values with the help of a Reynolds decomposition, whereas these variables are time-averaged. Additionally, a MFR (multiple frames of references) approach was used for the rotating domain (runner).

The SST turbulence model by Menter is often used for simulations in general and is a combination of the two well-known k-ε- and k-ω-models. This SST-model was used with automatic wall functions.

2.3.1 Full Model

Turbine unit was split into components (domains) for the purposes of CFD-calculation. Computational domain starts with the spiral case inlet**.** This domain also contains the stay vanes. This stay vane region is not rotationally periodic (different sizes of stay vanes, cut-out stay vane and cutwater) and thus the stay vane region was integrated into the spiral domain. Due to the complex geometry situation as described above, an unstructured grid was generated for this component. To separate the spiral case and stay vane for post-processing studies, a cylindrical surface is generated in between.

After the spiral domain the guide vane domain was connected to the spiral with a general grid interface (GGI). The guide vane mesh passage was generated by means of Turbogrid®, copied into the model 24 times and connected by means of a 1:1 interface. In post-processing, single guide vane is used for evaluations.

Between the guide vane and the runner domain the domain interface was set to frozen rotor. The mesh for the passage of the runner domain itself was also generated with Turbogrid® and connected by means of a 1:1 grid interface. The

mesh of the runner domain consists of the main passage which includes the blade and an outflow block which is automatically generated by Turbogrid to implement the HJCL topology easier. Outblock is internally connected by a 1:1 interface to the main block.

The draft tube domain was then connected with a frozen rotor domain interface. The stand pipe geometry, including the conical part at the bottom of the draft tube is generated according to the measurement on power plant. These dimensions are not available in the technical drawings. The existing internal aeration device was neglected. This device is out of operation since more than two decades. This information provided by the power plant operators.

Downstream of the draft tube an additional component, the so-called outblock, was connected to the draft tube. The function of this component is not to represent the effect of tail water. Its aim is to avoid the setting of boundary conditions directly at the draft tube outlet. This would prevent the backflows and cause and unrealistic outlet condition. In Figure 2.9, components of the full model are displayed in different colors. The inflow region is shown in green, the spiral and stay vanes in grey, the guide vane in orange – followed by the runner in red and the draft tube in blue The outblock is depicted in light blue. On the small picture in Figure 2.9, the additional post-processing plane for the stay vane performance is visualized in yellow.

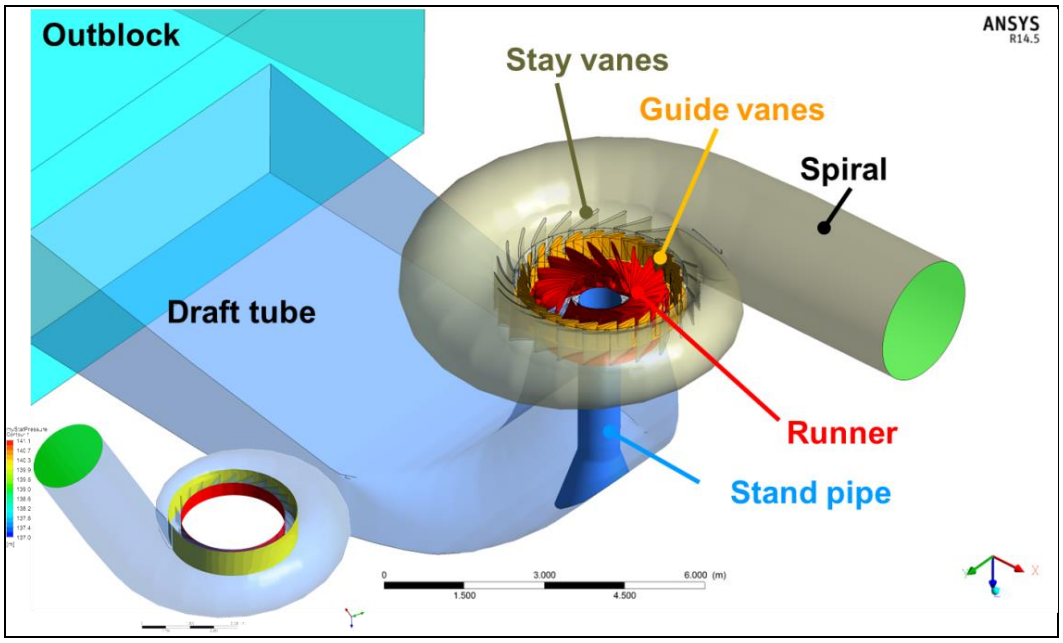

Figure 2.9 : Different domains of turbine used for analysis

The position of the interfaces between guide vane with runner and runner with draft tube is displayed in Figure 2.10. There are two lines for the interface between runner and draft tube: one thicker dotted orange line, which marks the interface for the draft tube including the standpipe, and one thinner dotted orange line, which marks the interface when using the draft tube without the standpipe. This figure also includes the leading and trailing edges of the runner which are shown together with the stand pipe. It has to be mentioned that the machine axis is the vertical axis (displayed at the right side) and the radius is the horizontal axis. As one requirement for grid generation is to have some space behind the trailing edge of the runner, the end point of the rotor – stator interface is a bit more downstream than the runner – draft tube gap in reality. This is shown in Figure 2.11, where the runner– draft tube gap is just behind the trailing edge. On the other side, the gap between runner hub and standpipe was set directly to the intersection between runner hub and standpipe during CFD simulation. In reality, the gap is also a bit more downstream (see Figure 2.11). With reference to the boundary conditions it has to be mentioned that the runner shroud surface in the simulation is a bit longer (and thus larger) than the real one and that the runner hub surface is a bit smaller than the real one. The aeration

device and the holes for the fastening bolts are neglected (see small photo in Figure 2.11 right).

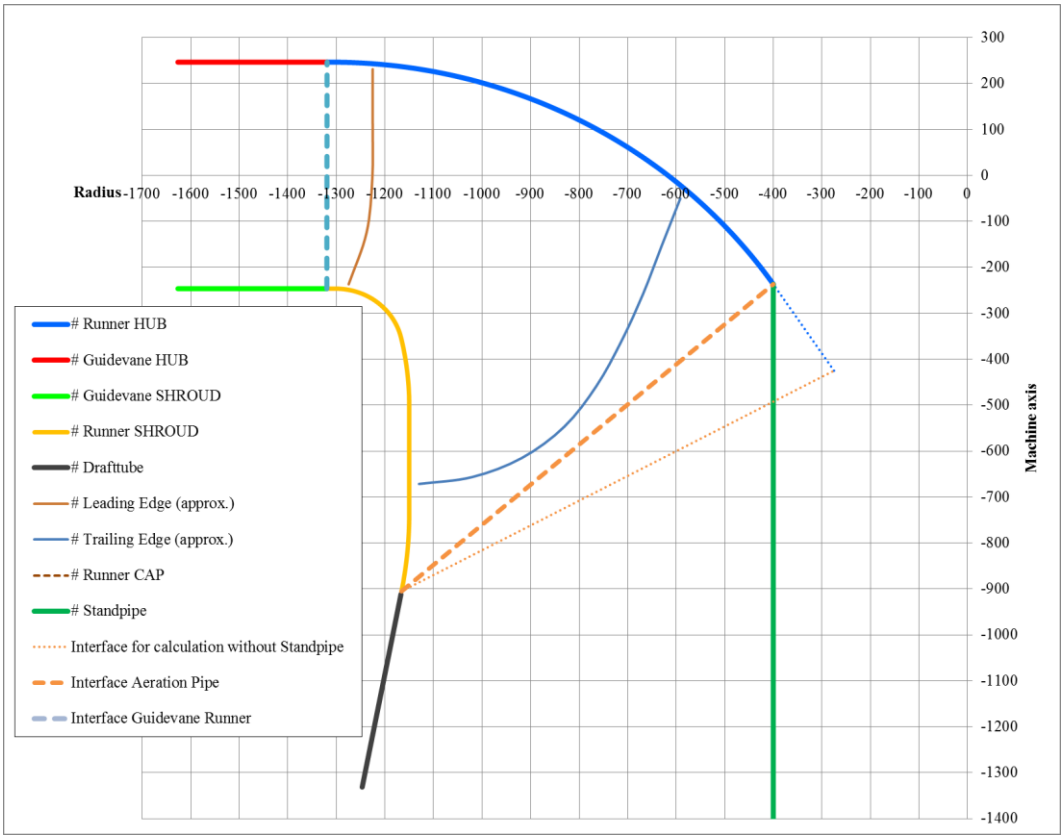

Figure 2.10 : Meridional view of existing runner with domain interface definitions

Generated stand-alone meshes are combined to a complete unit for different guide vane positions. Pressure is set as a boundary condition for inlet (green surface in Figure 2.9) and outlet and thus desired flow rate is obtained.

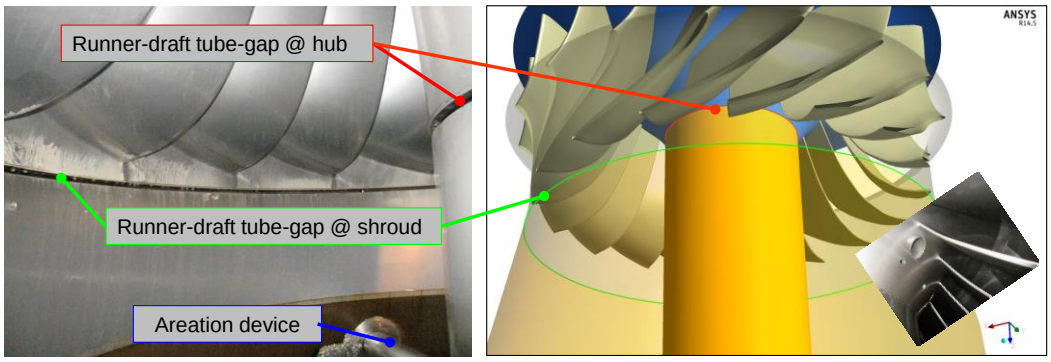

Figure 2.11 : Comparison between actual turbine and CFD model

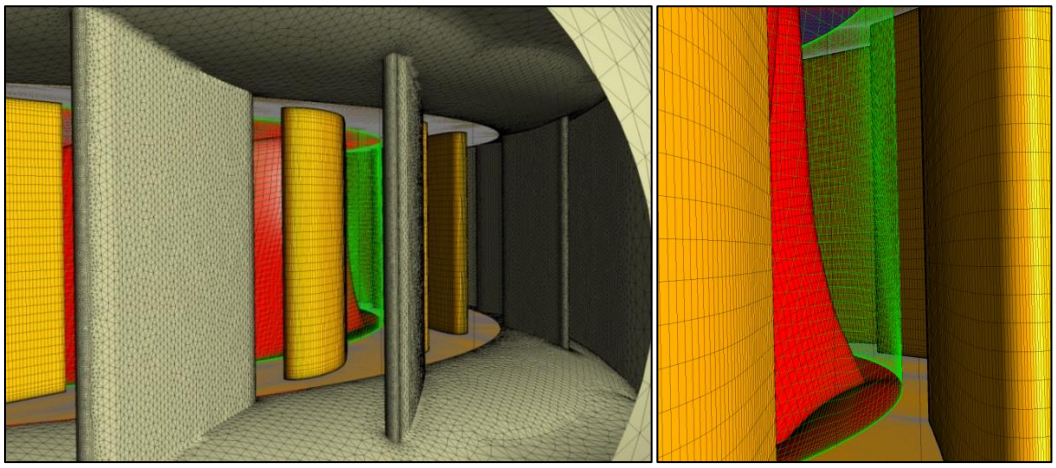

Figure 2.12 : Guide vane - runner interface

Menter's SST turbulence model [5] with automatic wall functions was applied, and in order to achieve a satisfying convergence level all sensitive variables and imbalances were monitored. When the analysis setup is prepared, all steps are recorded as macro, which is a powerful tool of CFX. This macro is used for generating the setups for other analysis files with different heads and guide vane openings. This provides avoiding mistakes and to allow for easy changes of meshes and other settings.

2.3.2 Simple Model

For the optimization process a simple model was generated as well. This model consists of only one guide vane, one runner passage and the draft tube. For this model the same basic meshes were used as for the full model. Main purpose of using the simple setup is shortening the computational time. This model is only used for comparing the optimization versions between each other. The successful versions then analyzed with the full setup for comparison with the existing turbine.

2.3.3 Definition on output expressions

For the evaluation of the hydraulic performance of a unit, the key figures as mentioned in the following are of interest. In general, the net head is the difference between total pressure at the inlet of the spiral and total pressure at the outlet of the draft tube. According to the IEC standard [22], the net head represents the difference between the total pressure at the inlet (inflow of spiral) and the static pressure at the outlet (end of draft tube) where the mean kinetic energy head is added to the outlet pressure (eq. 1). In order to analyze each component separately, a head loss analysis (eq. 2) was performed to calculate a cumulative figure of the total unit. In this case, the total pressure difference between inlet and outlet of each component was set in comparison to the net head. For the runner, the shaft power was also taken into account and subtracted from the losses (eq. 3). For the determination of the cavitation performance a histogram analysis was performed to evaluate minimum blade pressure. This minimum blade pressure was recalculated in non-dimensional form as the Thomas cavitation parameter (eq. 4), and then this σ-value was compared to a $\sigma_{plant,allowed}$-value, whereas the local pressure at the blade was set to vapor pressure and the altitude of the machine axis against the tail water was applied (eq. 5). As σ_{turbine} is lower than $\sigma_{plant,allowed}$, cavitation free operation could be stated.

$$H = \frac{p_{Total–Inlet} - p_{Total–Outlet}}{\rho g} = \frac{p_{Total–Inlet} - \left(p_{Static–Outlet} + \frac{\rho}{2}\left(Q / A_{Outlet}\right)^2 \right)}{\rho g} \quad \textbf{(Eq. 1)}$$

$p_{Total–Inlet}$ is the total pressure at the spiral case inlet. $p_{Total–outlet}$ is the total pressure at draft tube outlet. A_{Outlet} is the draft tube outlet area.

$$\eta_{Total} = 1 - \frac{\Sigma H_{Loss}}{H} = 1 - \frac{H_{Loss–Intake} + H_{Loss–Guidevane} + H_{Loss–Runner} + H_{Loss–Drafttube}}{H} \quad \textbf{(Eq.2)}$$

H_{Loss} is the total head loss in turbine in meters. $H_{Loss–Intake}$ is the spiral case and stay vane losses in meters. $H_{Loss–Guidevane}$ is the total head loss in guide vanes in meters. $H_{Loss–Runner}$ is the total loss in the runner in meters. $H_{Loss–Drafttube}$is the total loss in the draft tube in meters.

$$H_{Loss–Runner} = \frac{p_{Total–Runner–Inlet} - p_{Total–Runner–Outlet}}{\rho g} - \frac{M_{Runner}\omega}{\rho g Q} \quad \textbf{(Eq. 3)}$$

M_{Runner} is the runner rotational torque. ω is the rotational speed (ms^{-1}).

$$\sigma_{Turbine,p\_Histogram} = \frac{\frac{p_{Total–Drafttube-Outlet} - p_{Histogram}}{\rho g}}{H} \quad \textbf{(Eq. 4)}$$

$\sigma_{Turbine,p_Histogram}$is the Thoma cavitation coefficient of the turbine.

$$\sigma_{plant,allowed} = \frac{\frac{p_{Total–Drafttube-Outlet} - p_{Vapour}}{\rho g} - (H_{TailWaterLevel} - H_{MachineAxis})}{H_{Def}} \quad \textbf{(Eq. 5)}$$

The net head of the turbine is the difference between the headwater level (HWL) and the tail water level (TWL) minus the losses in the penstock from the water intake to the inflow of the spiral (just behind the valve). These losses are system losses and depend on the actual flow rate.

Additionally, the velocities were split into their components in circumferential direction c_u, radial direction c_r and axial direction c_{axial} in order to visualize the flow situation more in detail.

The swirl (eq. 7) is calculated by the y-component of the velocity multiplied by the distance in x-direction minus the x-component of the velocity multiplied by the distance in y-direction. The resulting difference is then divided by the radius (eq. 6) to calculate the c_u-component (eq. 8).

The radial velocity c_r (eq. 9) is calculated as follows: the x-component of the velocity is multiplied by the distance in x-direction plus the y-component of the velocity is multiplied by the distance in y-direction. The sum of these two multiplications is then divided by the radius (eq. 6) to calculate the radial velocity component. The axial velocity is directly the *z*-component of the velocity (eq. 10).

$$\boldsymbol{R = (X^2 + Y^2)^{0.5}} \quad \textbf{(Eq. 6)}$$

$$\boldsymbol{swirl = v_{stn}X - u_{stn}Y} \quad \textbf{(Eq. 7)}$$

$\boldsymbol{v_{stn}}$ is the y component of the velocity in stationary frame. $\boldsymbol{u_{stn}}$ is the x component of the velocity in stationary frame.

$$\boldsymbol{c_u = \frac{v_{stn}X - u_{stn}Y}{R}} \quad \textbf{(Eq. 8)}$$

$$\boldsymbol{c_r = \frac{u_{stn}X - v_{stn}Y}{R}} \quad \textbf{(Eq. 9)}$$

$$\boldsymbol{c_{axial} = w_{stn}} \quad \textbf{(Eq. 10)}$$

$$M_{11} = \frac{M_{Guidevane,Coord}}{D_{GV-trunnion} \cdot H_{Def}} \quad \textbf{(Eq. 11)}$$

M_{11} is the normalized guide vane torque. Whereas $M_{Guidevane,Coord}$ is the torque of one guide vane around the guide vane axis and $D_{GV\text{-}trunnion}$ is the diameter of the guide vane adjustment axis.

2.4 Mesh Independency

The mesh study was carried out before the on-site measurements during which the modifications at the draft tube (stand pipe) were identified in detail. The main differences occur at the spiral guide vane domains, where the runner is almost constant. However, even as the largest model is not mesh-independent, the influence is now on a minor level. At present, it is not possible to run calculations with higher mesh numbers due to limitations in RAM and CPU hours needed. The overall efficiency becomes higher but for all mesh densities the flow rate does not change. In the next step, the optimization was done for the unit and therefore always a relative improvement will be discussed.

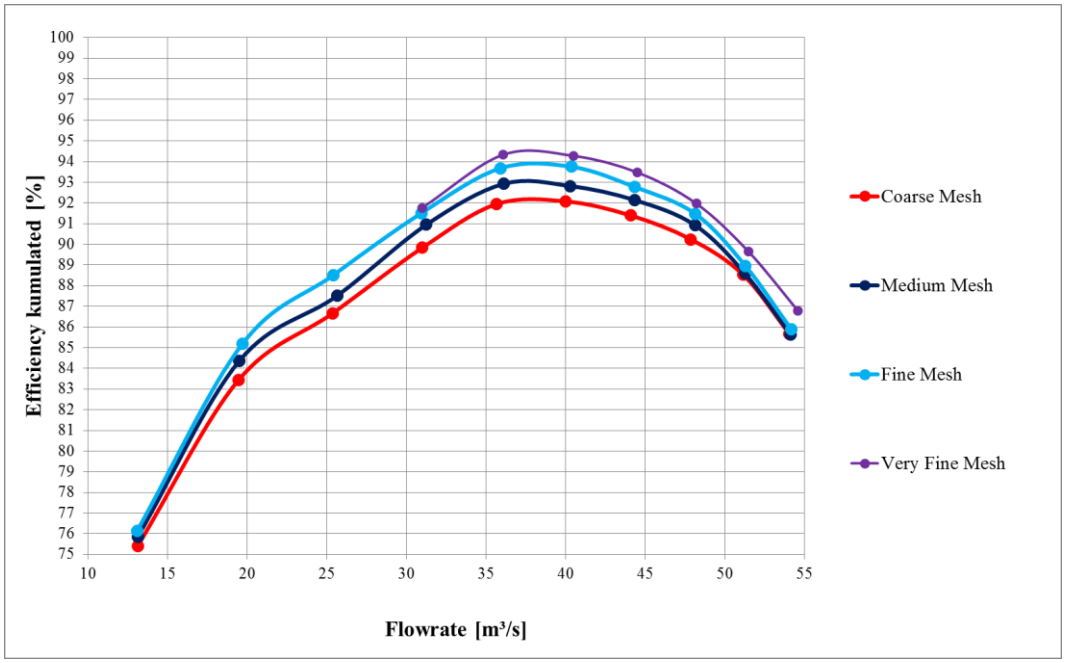

Figure 2.13 : Mesh study for full model

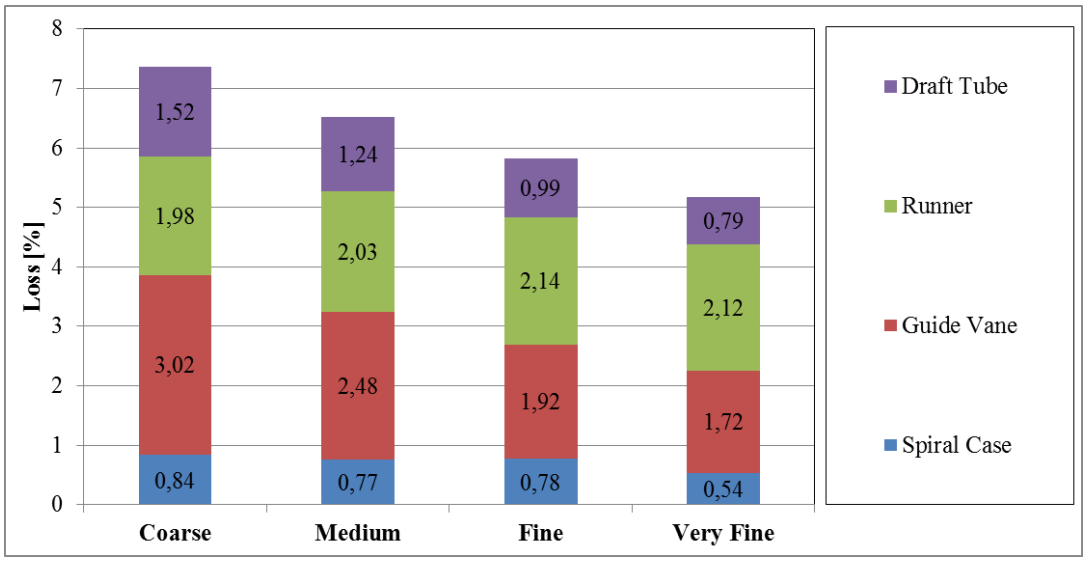

Figure 2.14 : Loss analysis for different mesh densities for the same operation point

2.5 Results

2.5.1 Overall Results

The overall performance is displayed in Figure 2.15 for the accumulated efficiency and in Figure 2.16 for the cavitation performance. In Figure 2.15, the losses for each component are between the accumulated efficiency curves, which are drawn against the flow rate. Also, the efficiency curve for the measurement in 2007 is depicted.

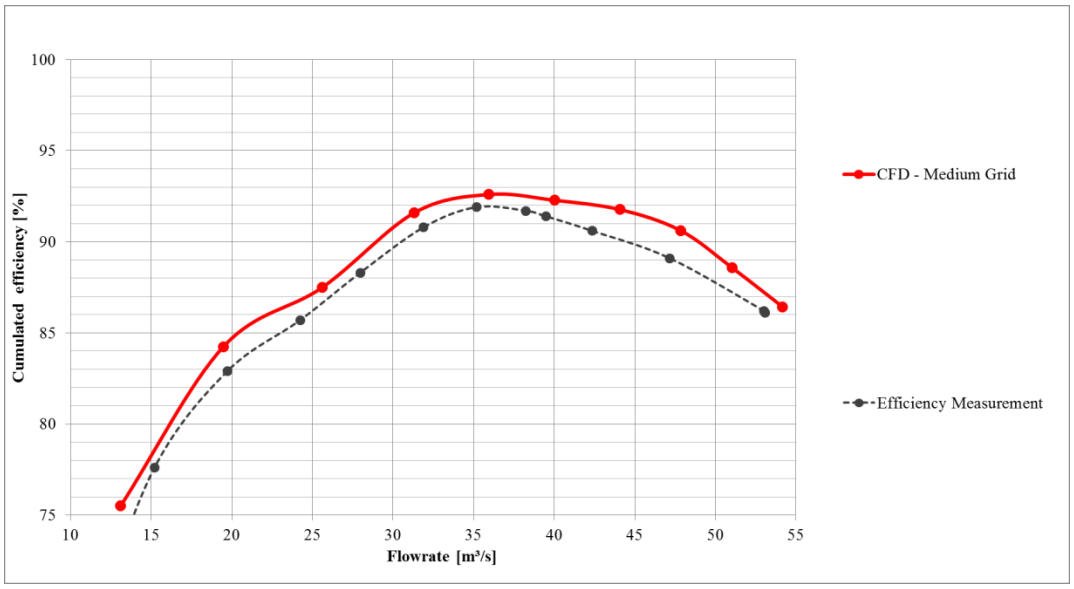

Figure 2.15 : Efficiency splitting, full model, medium grid

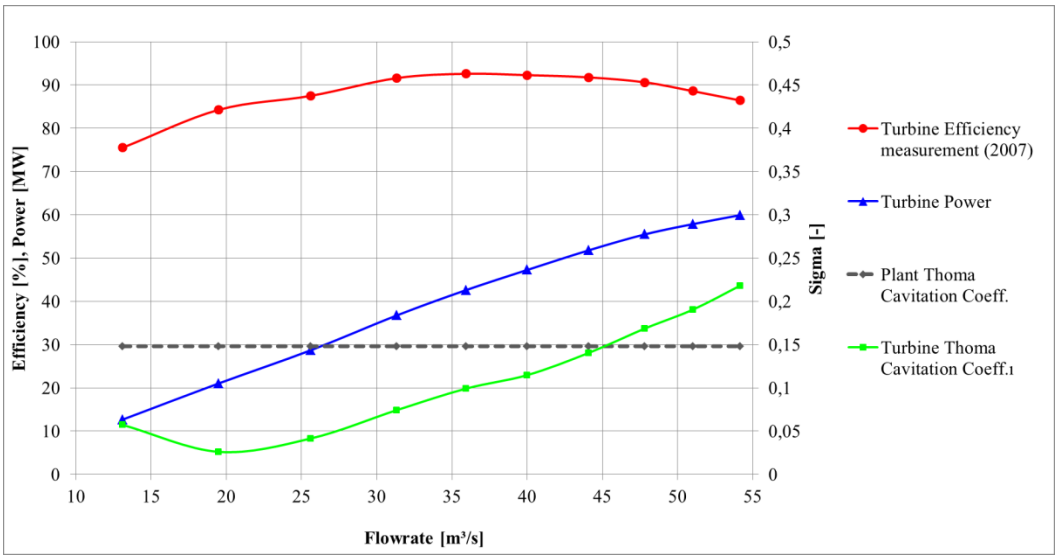

Figure 2.16 : Cavitation behavior, full model, medium grid

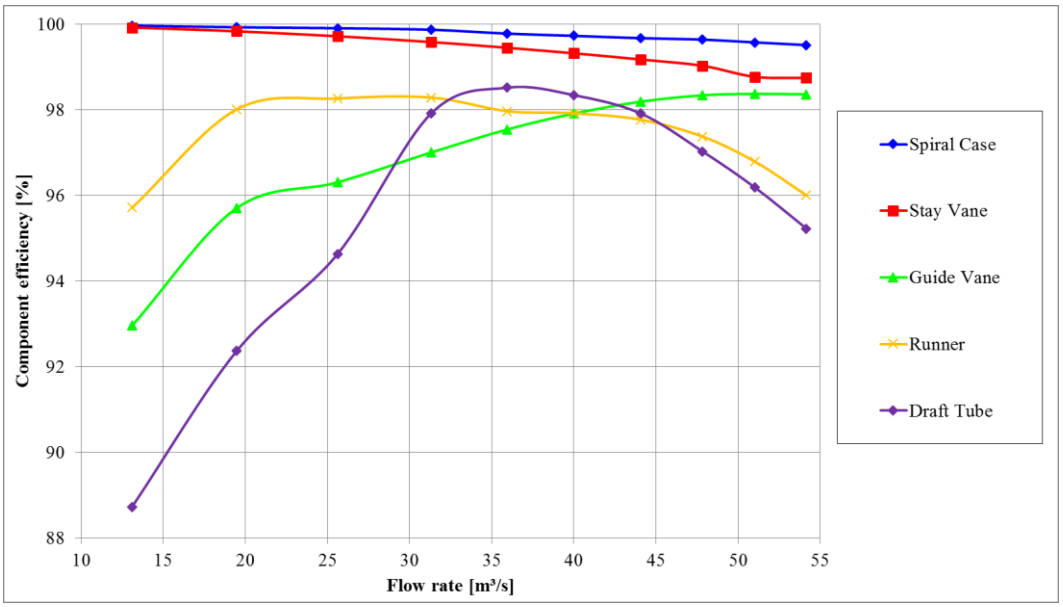

Figure 2.17 : Single component efficiency, full model, medium grid

In Figure 2.17, the efficiency for each component is shown. Regarding the spiral and stay vanes, a decrease of the efficiency when increasing the flow rate could be detected. The runner itself has its best efficiency point between 25 and 30 m³/s flow rate with a decreasing efficiency at higher flow rates. For the guide vane the best efficiency point is at full load (maximum power) and the optimum of the draft tube is at a flow rate of about Q = 35 m³/s. All components together yield performance characteristics which are also shown in Figure 2.15. The best efficiency is at a flow rate of about 35 to 40 m³/s. At maximum flow rate the power is also increasing. During the measurement campaign the highest flow rate was Q = 52 m³/s.

The cavitation performance is also presented in Figure 2.16, where the risk for cavitation is visible for flow rates higher than Q = 45 m³/s. There, the cavitation coefficient $\sigma_{turbine}$ is higher than the σ_{plant} value. The flow situation through the runner (as a result of the hydraulic contour) leads to a low pressure zone at the leading edge of the runner (at the suction side) and also to low pressure zones at the trailing edge. This can be seen in Figure 2.18 and Figure 2.19. Blade loading graphs are shown for different span-wise locations in Figure 2.20 and Figure 2.21. Especially

at the shroud region, there is a large zone with low pressure just behind the leading edge (suction side marked with red). For higher stream wise locations the pressure increases again which means that there is a pump effect. For locations after 60% stream wise the pressure is decreasing again. For a span of 50% and less the hydraulic shape works correctly from a high pressure at the leading edge to a low pressure at the trailing edge.

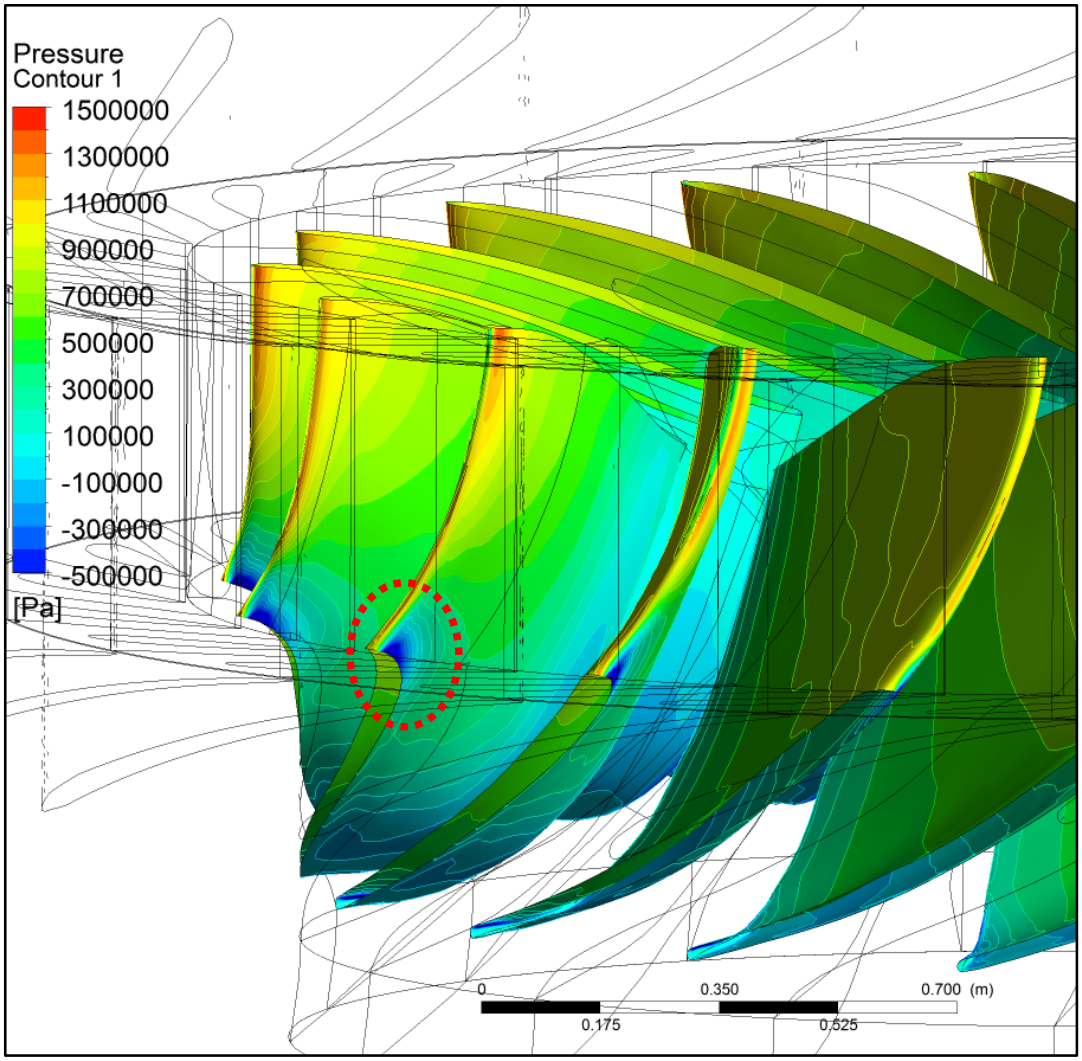

Figure 2.18 : Pressure contour plot with low pressure zones at the leading edge

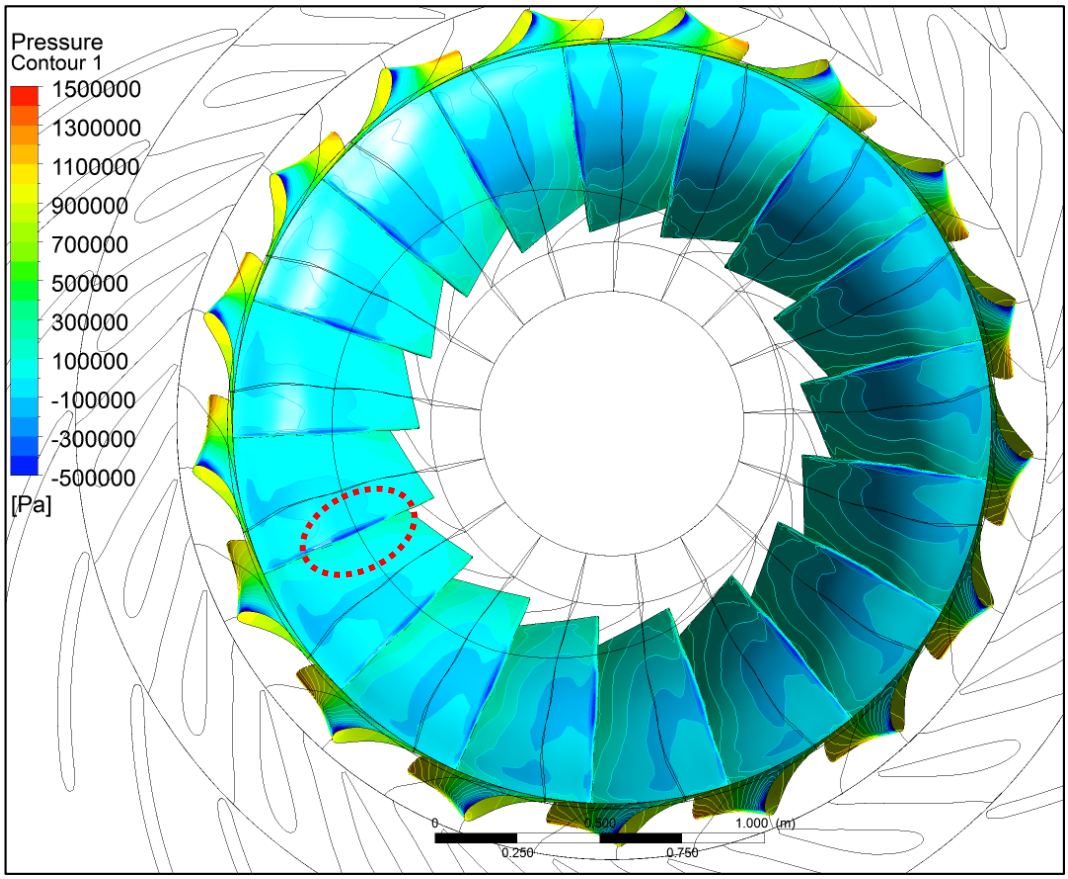

Figure 2.19 : Pressure contour plot with low pressure zones at the trailing edge

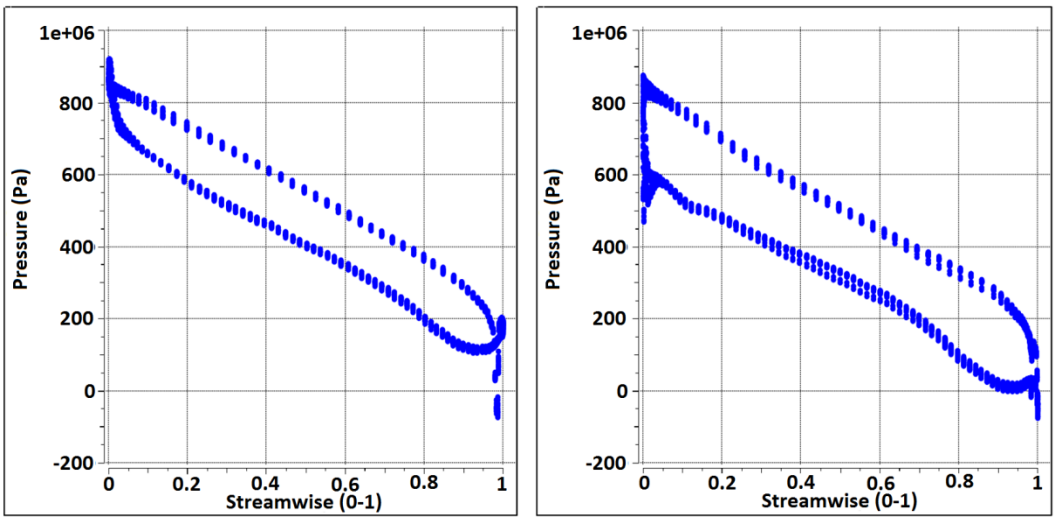

Figure 2.20 : Blade loading for 0.05 (left) and 0.5 (right) blade height

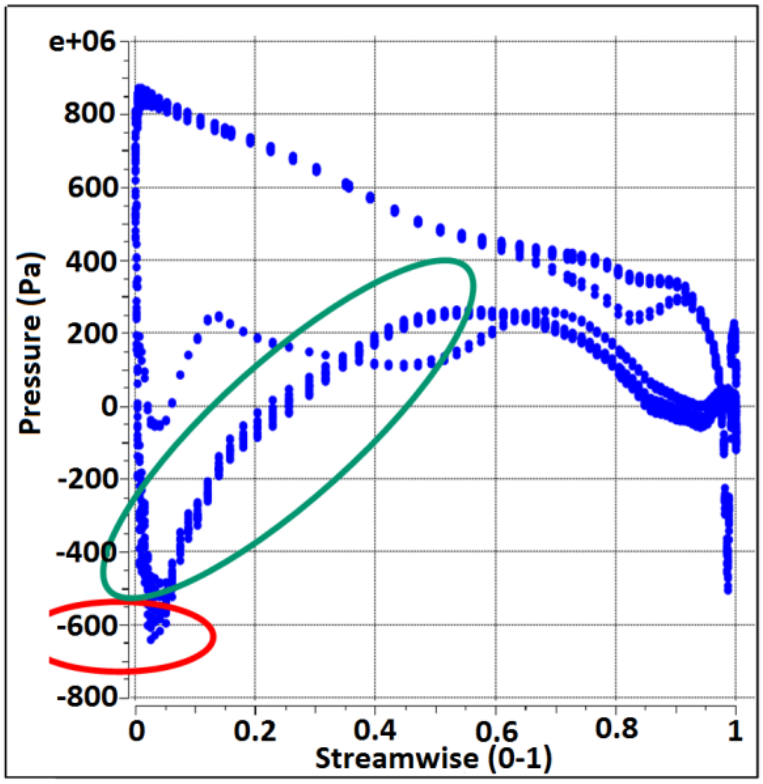

Figure 2.21 : Blade loading for 0.95 (right) blade height

2.5.2 Spiral Case Results

To post-process the spiral, several planes were generated in the domain spiral as shown in Figure 2.22. A plane was generated at every 15°, whereas at the inlet of the spiral additional 3 parallel planes were generated. Those planes include the stay vane region. The stay vane area is then subtracted from each plane area and depicted as the red dotted line in Figure 2.23. The area distribution is almost linear.

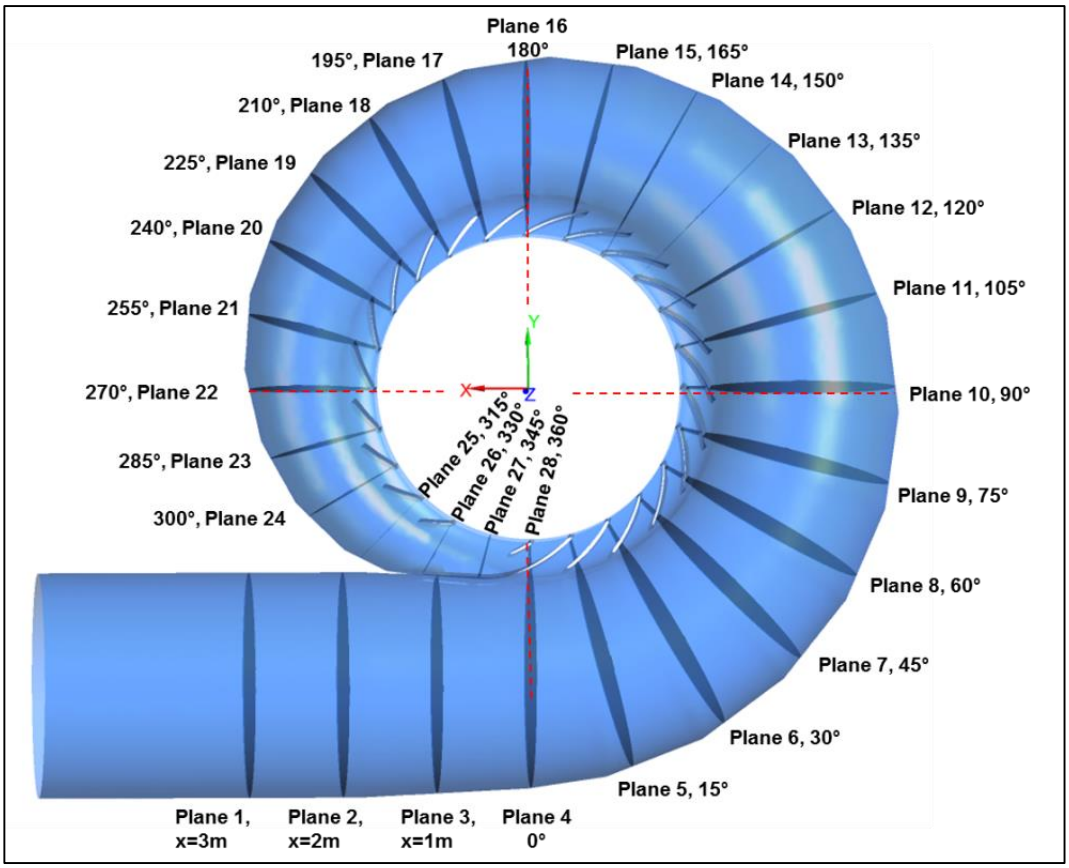

Figure 2.22 : Post-processing planes of spiral

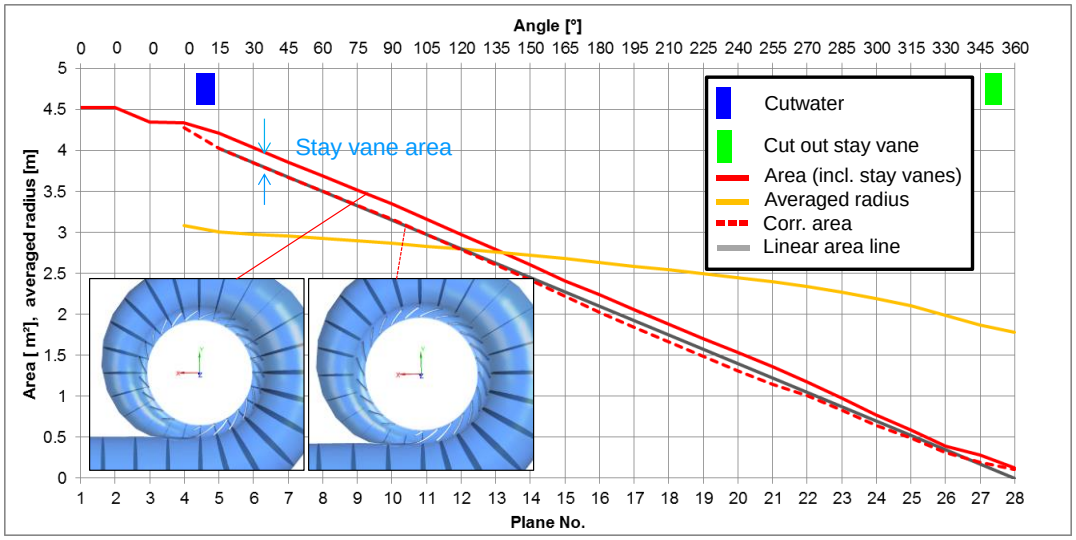

Figure 2.23 : Area distribution of the spiral case

The grey line in Figure 2.23 marks a linear area distribution and the deviation of the corrected area line is minor. A spiral design with constant swirl leads to a non-linear area distribution.

The radius is an area-averaged radius of the whole plane and decreases stronger for larger angles. This radius has its minimum at the end of the cutwater (approx. at plane 5 in Figure 2.22) at about 1.625 m.

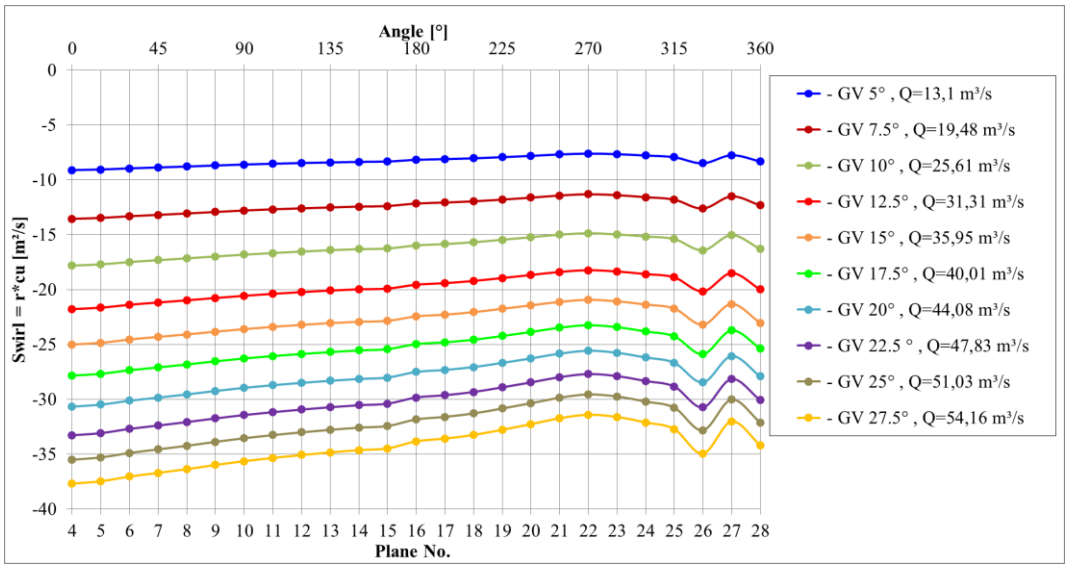

Figure 2.24 : Swirl (=rc_u) for different operation points

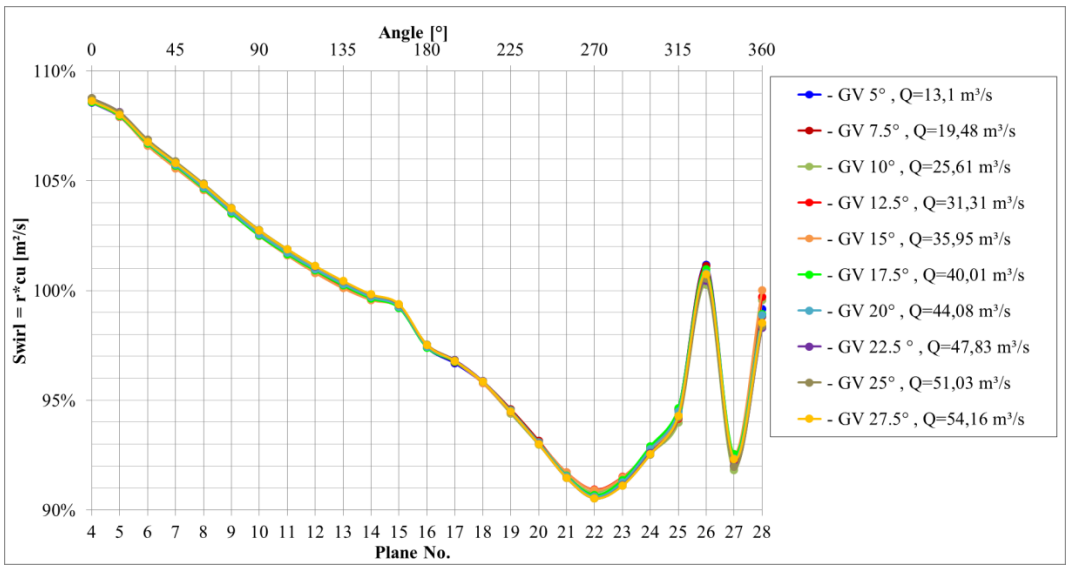

Figure 2.25 : Normalized Swirl (=rcu) for different operation points

In Figure 2.24 the swirl, which is rc_u, is shown for different operation points. Therefore, for every plane an area-averaged value of the swirl (rc_u) was calculated. From extreme part load in blue (GV 5°, Q=13.1 m³/s) to overload in yellow (GV 27.5°, Q= 54.16 m³/s) eight additional operation points are post-processed. The area-averaged value of the swirl was generated, and this was done for every plane and plotted in Figure 2.25.

When this value is normalized with the averaged value of each operation point, all of the curves are identical. The value of rc_u is not constant over the volute. The swirl has its highest value at the beginning of about +8% of the averaged value and its lowest value at plane 22 (270°) with -9% (see Figure 2.25 bottom). For different heads (in the range of variation on-site) there is no difference in the shape, only the averaged value is different (Figure 2.26).

Figure 2.26 shows different velocities on the same post-processing planes. The velocity is a scalar variable, therefore this variable has no "direction" and all values are positive (see Figure 2.27 left). The component velocity w is a vector component and thus positive and negative values could occur (see Figure 2.27 right. The highest values of the velocity w are marked with the red dotted rectangle in Figure 2.27.

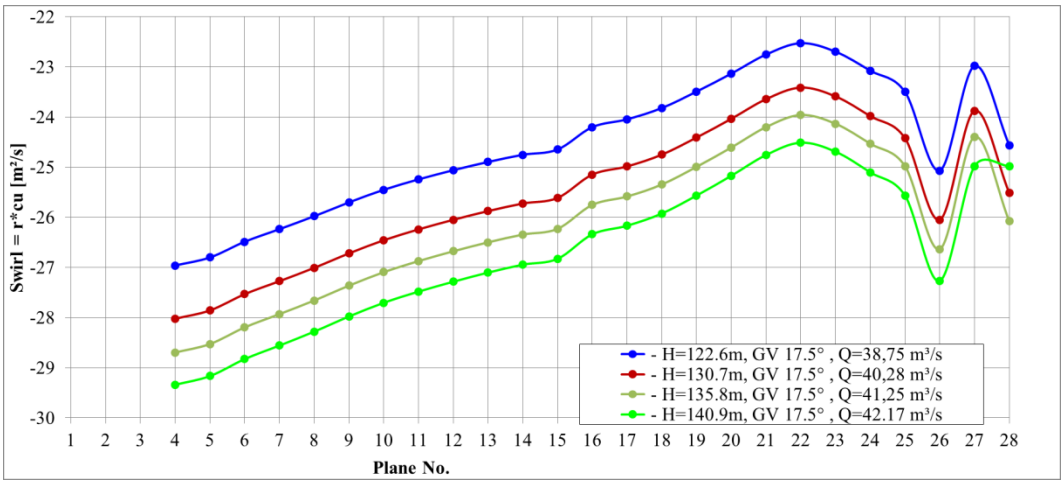

Figure 2.26 : Swirl (=rc_u) for different heads

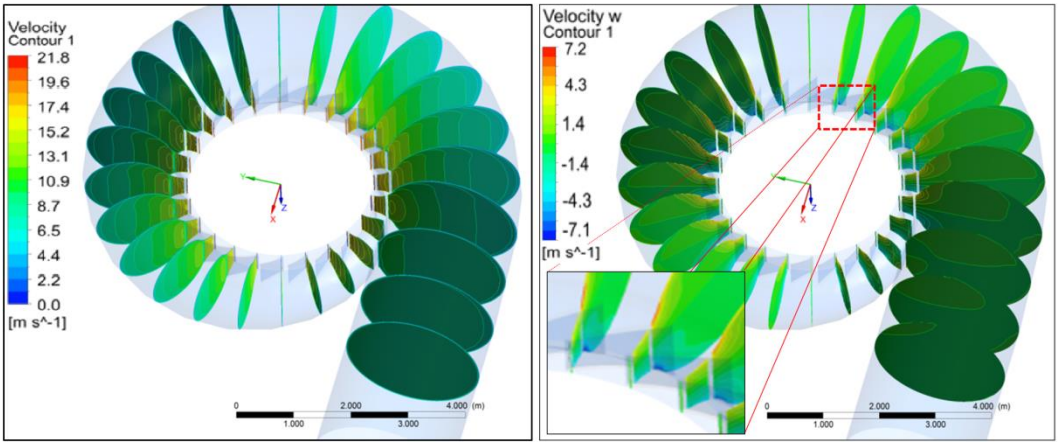

Figure 2.27 : Velocity and velocity in *z*-direction (*w*) situation for BEP (GV 17.5°, Q = 40.01 m³/s, H = 135.8 m)

2.5.3 Stay Vane

To visualize the flow situation at the entrance of the stay vanes, 5 lines were generated with a radius of 2.01 m (just upstream the stay vanes) and at different *z*-axis locations. On these lines velocities were analyzed. The cutwater ends at γ=255° and starts at γ=270°. The last guide vane is between γ=265 and γ=280°, and the cut-out guide vane is between γ=280° and γ=295°.

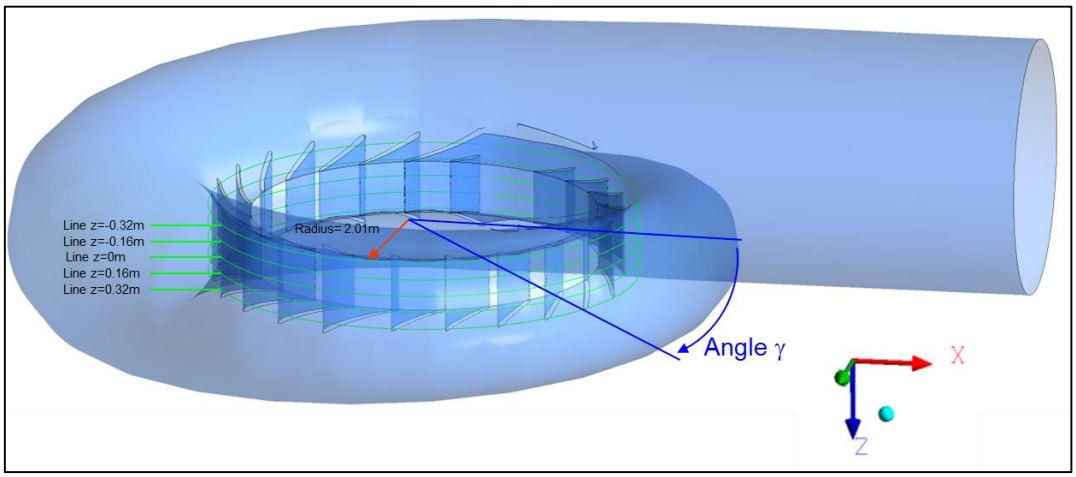

Figure 2.28 : Lines for post-processing at the entrance of the stay vanes

In Figure 2.29 the velocity is plotted against the angle γ. For the first 90° and the last section between 300° and 360° the stay vanes are a bit more downstream of the post-processing line. Thus, the influence of the stay vanes is shown as small fluctuations. Between 90° and 270°, leading edges of the stay vanes are close to the post-processing line and thus the fluctuations are even higher. The lowest velocities are exactly at the last guide vane, where the velocity at the cut-out stay vane is higher. According to the coordinate system (counter rotating machine), the components of the velocities are negative. The radial and circumferential (theta) components of the velocity are plotted in Figure 2.29. Fluctuations occur vice versa – a peak in the theta-velocity yields a minimum radial velocity.

In Figure 2.30, the radial and circumferential (theta) velocities are plotted for different operation points. The shape is completely identical, only the velocity components are scaled.

In Figure 2.29 also the axial component is plotted in green, and as the post-processing line is at the mid plane (z=0 m) the component is 0 m/s. In Figure 2.31, this axial component is plotted for different z-values, the component is no longer 0 m/s. For the best efficiency point the maximum value is about 3.5 m/s (Figure 2.31) and for the maximum flow rate (GV 25^0) it is then v_{axial} = +/-4.5 m/s (not shown).

Figure 2.32 presents the corresponding figure of Figure 2.29 at the outlet of the stay vanes. The same velocity components are displayed in the same colors. The fluctuations become higher –especially because of the radius R = 1.626 m of the line which is just downstream the trailing edge.

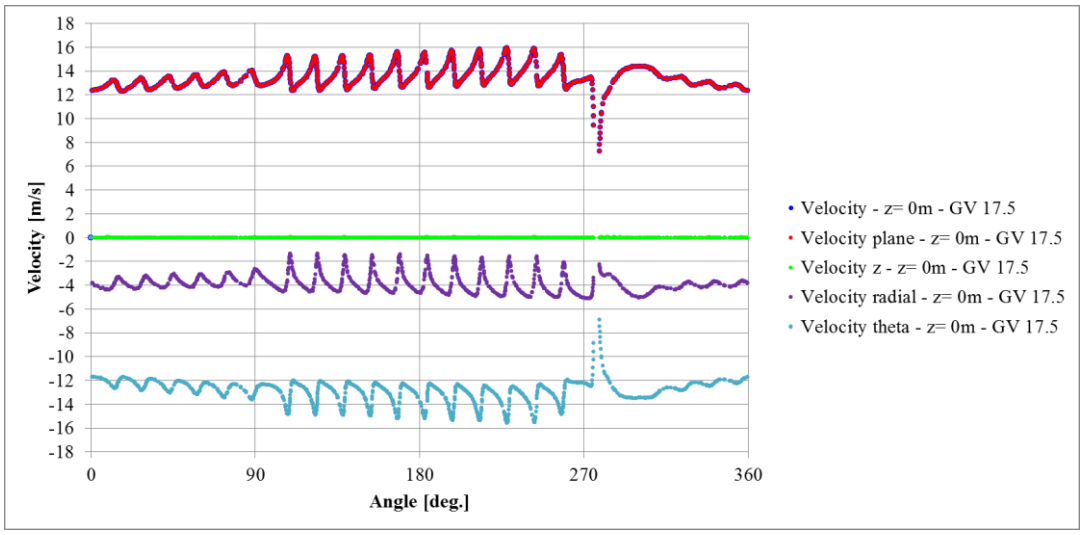

Figure 2.29 : Different velocities at the stay vane entrance, *z* = 0 m (middle), BEP point

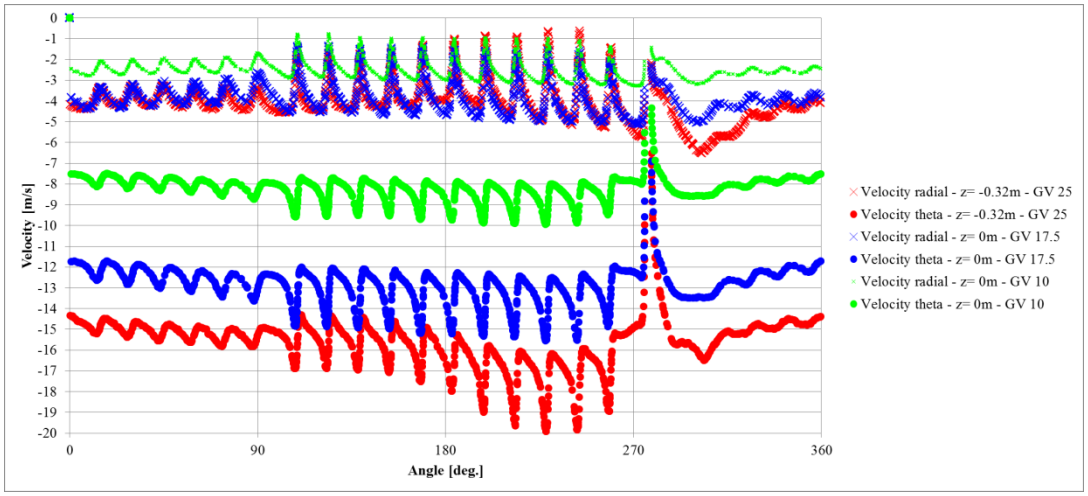

Figure 2.30 : Radial and circumferential (theta) velocities for part load (GV 10°), BEP (GV 17.5°) and overload (GV 25°)

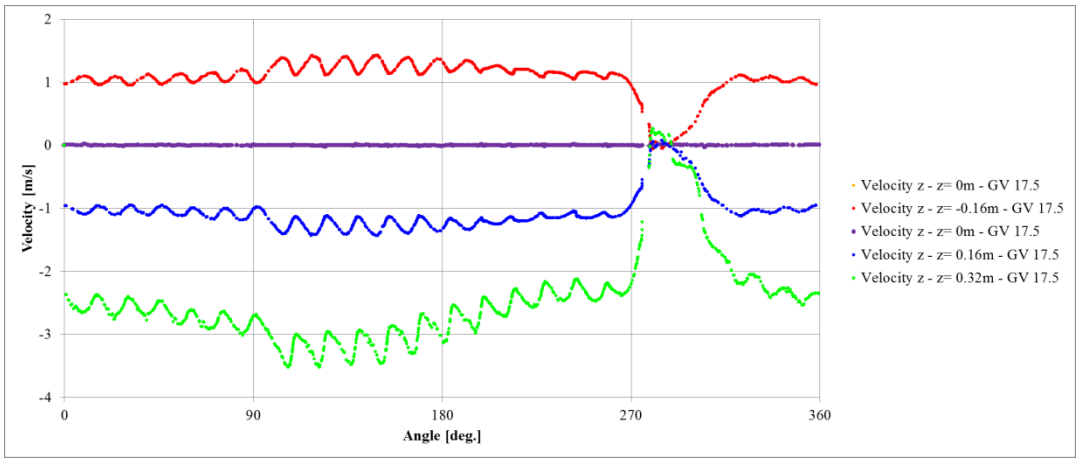

Figure 2.31 : Axial velocity components for different *z*-value

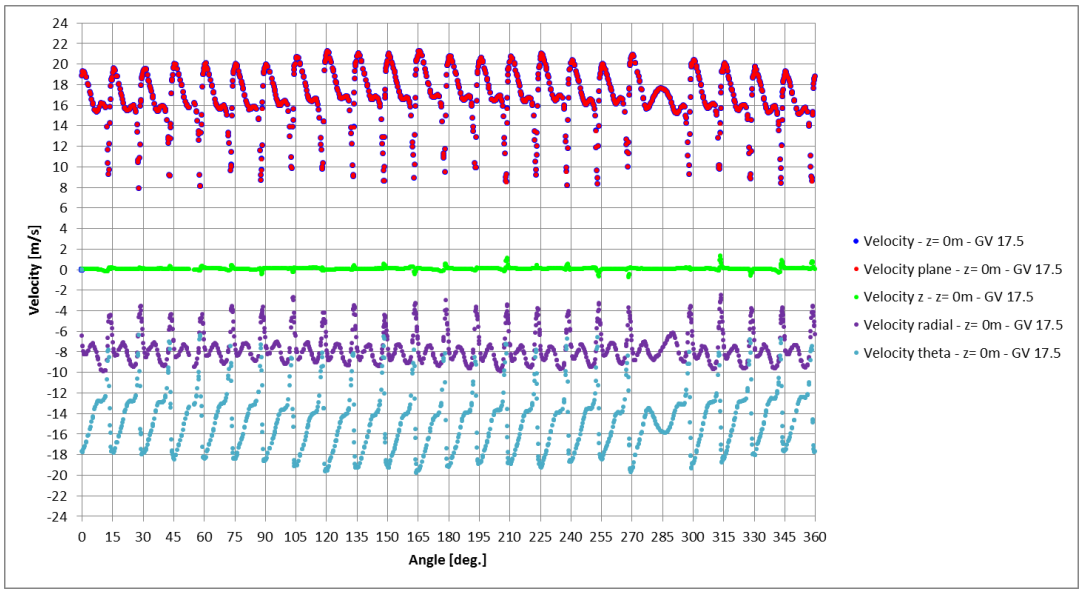

Figure 2.32 : Different velocities at stay vane outlet, *z* = 0 m (middle), BEP point

In Figure 2.34, a pressure plot is shown for the best efficiency point (BEP). It can be seen that the stagnation point of the flow is exactly at the leading edge for the first stay vanes and thus low pressure zones at the suction side of the stay vanes are

avoided. At the end of the spiral the stagnation point is no longer directly on the leading edge (a bit more on the pressure side) and thus low pressure zones occur at the suction side of the last stay vanes. There is a small optimization potential, but as the average velocities through the spiral case are almost constant, performance of the spiral case is acceptable (see Figure 2.32).

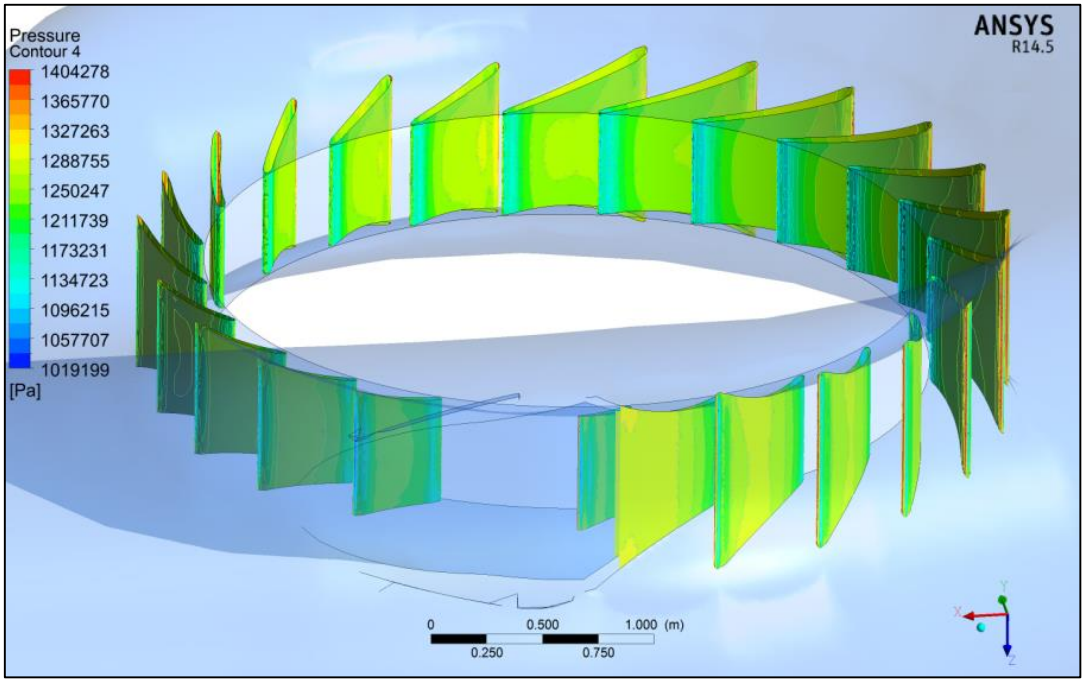

Figure 2.33 : Pressure plot of stay vanes, BEP, GV 17.5°

The velocity vector plots in Figure 2.34 are for the inlet and outlet area at part load (left), BEP (middle) and overload (right) operation points. The outlet vector plot shows a velocity situation which is strongly influenced by the stay vanes and thus a "stepped" velocity profile is the result. This effect can also be seen at the inlet zone of the area, not so strong for part load operation but definitely for overload

operation. This flow situation is then the inlet condition for the guide vanes. A rotational offset of the later discussed guide vanes against the stay vanes has to be investigated during the optimization.

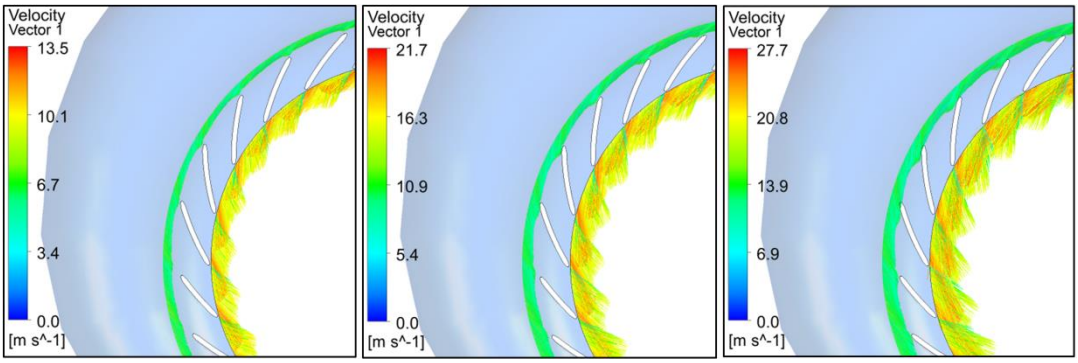

Figure 2.34 : Pressure plot of stay vanes, vector plot at inflow and outflow of stay vanes

2.5.4 Guide Vanes

For each guide vane passage the mass flow was evaluated at the inlet and at the outlet of the passage (see example passage colored green in Figure 2.35). The results were normalized with the averaged mass flow through one passage. In Figure 2.35, this is depicted for different operation points.

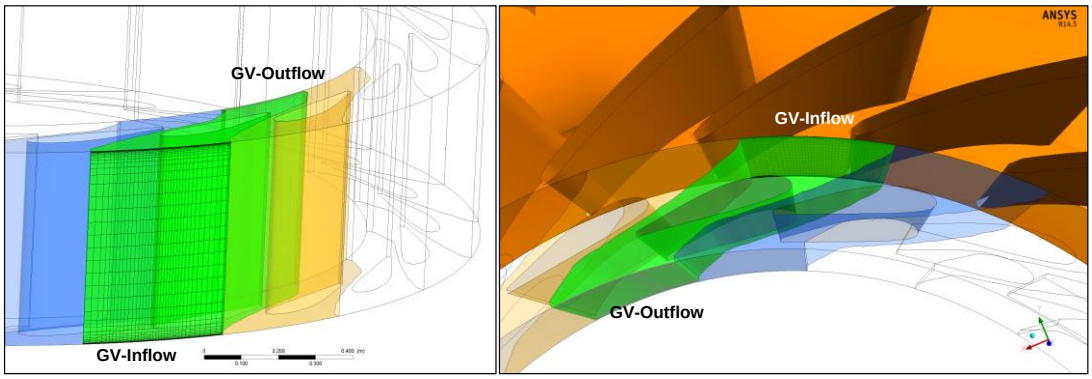

Figure 2.35 : Guide vane passage with inflow and outflow

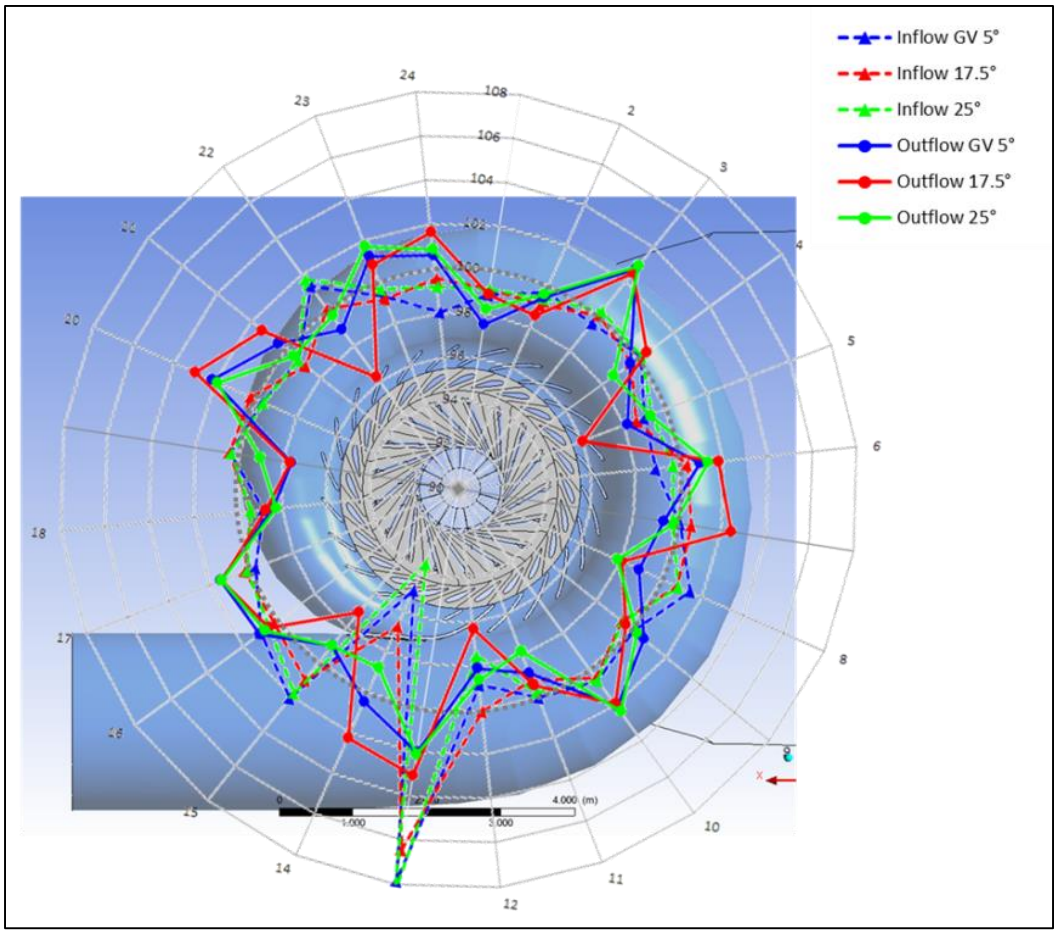

Figure 2.36 : Mass flow normalized through the guide vane

The influence of the cutwater can clearly be seen. The mass flow which enters the machine and reaches the last stay vane section (the last one after the cut-out stay vane) enters guide vane “No. 12” in Figure 2.36 and has a low mass flow, whereas guide vane “No. 13” has an extremely high mass flow rate. This guide vane position is just behind the cut-out stay vane and thus the mass flow rate is 8% higher than the averaged flow rate. The lowest values of the mass flow rate could be detected at guide vane “No.1” which is located opposite to the cutwater (180° turned). This is the situation for the inflow of the guide vane which is visualized by means of the dotted lines in Figure 2.36 for different operation points. The outflow of the guide vane is visualized by means of continuous lines with corresponding colors of the operation point. Especially for the highest fluctuation of guide vane no. 12, there is a homogenization effect through the guide vanes and the peak is lowered to 3%. A few of the other guide vanes become a bit more inhomogeneous, but at least all guide vane mass flows are in a fluctuation range of +/- 4 percent for all guide vanes at different operation points.

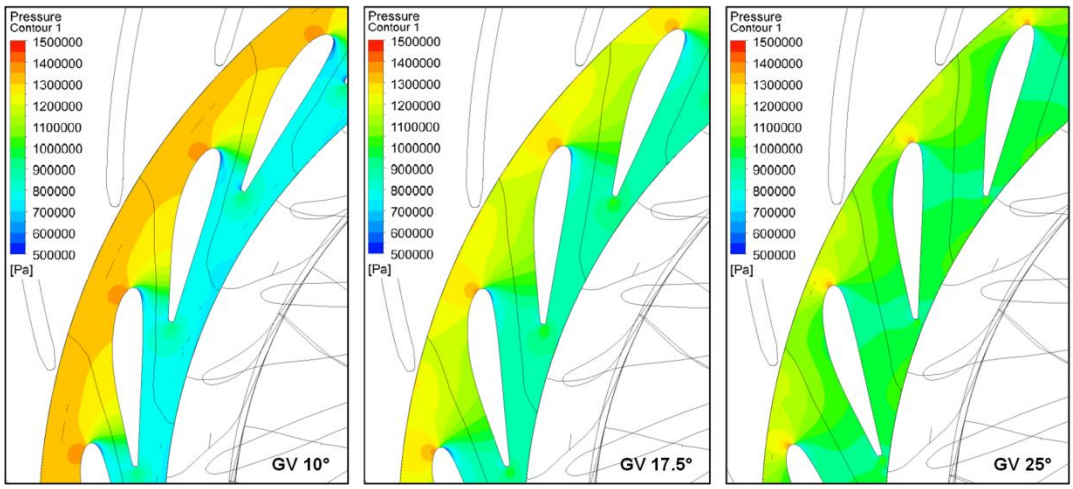

Figure 2.37 : Pressure contour plot at mid plane (z = 0 m)

Figure 2.17 presents the single efficiencies of the unit, for the guide vane the best efficiency is at highest flow rates. In the overall best efficiency point of the unit (GV 17.5°), the stagnation point is not directly on the leading edge. Therefore, the leading edge will be circulated by the water and high velocities occur, which is shown in Figure 2.38. This yields a low pressure zone which is shown in Figure 2.37 on the location opposite of the stagnation point (red and orange colored zones) at the unsymmetrical profile of the guide vane (zones colored blue)

Figure 2.38 consists of 3 planes for each operation point whereas a vector plot is displayed to visualize the flow situation. Only for maximum flow, the flow situation at the guide vane leading edge at the 3 different planes is correct (z = -0.2 m, z = 0 m and z = 0.32 m).

The velocity components at the inlet and the outlet of the guide vane are presented in Figure 2.39, Figure 2.40 and Figure 2.41 for different operation points. At the highest flow rate, the tangential velocity component c_u also has the highest absolute value at the inlet. This applies vice versa to the outlet of the guide vane, where – due to the fact that the opening is that small – most of the flow is still directed in circumferential direction. Therefore, the radial velocity component, c_r gets its highest absolute value at the highest flow rate.

Due to the symmetry of the spiral and stay vanes the axial velocity should have almost a zero value. The axial component is at a much lower level, however not zero. There is an upstream effect of the turning flow direction in the runner. Also, the c_m-distribution is higher at the shroud than at the hub.

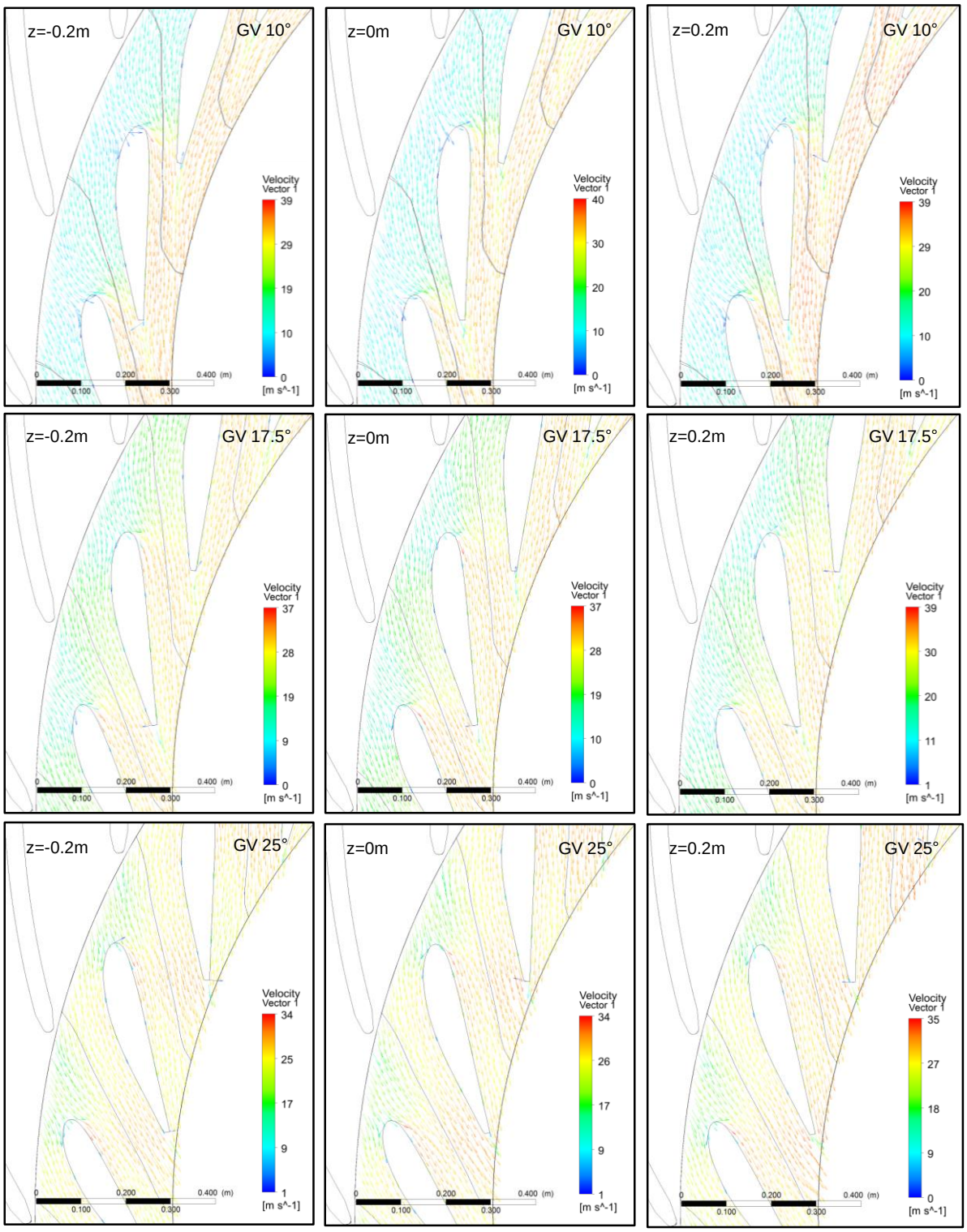

Figure 2.38 : Guide vane vector plot on planes with *z* = -0.2 m, *z* = 0 m and *z* = 0.2 m for different operation points

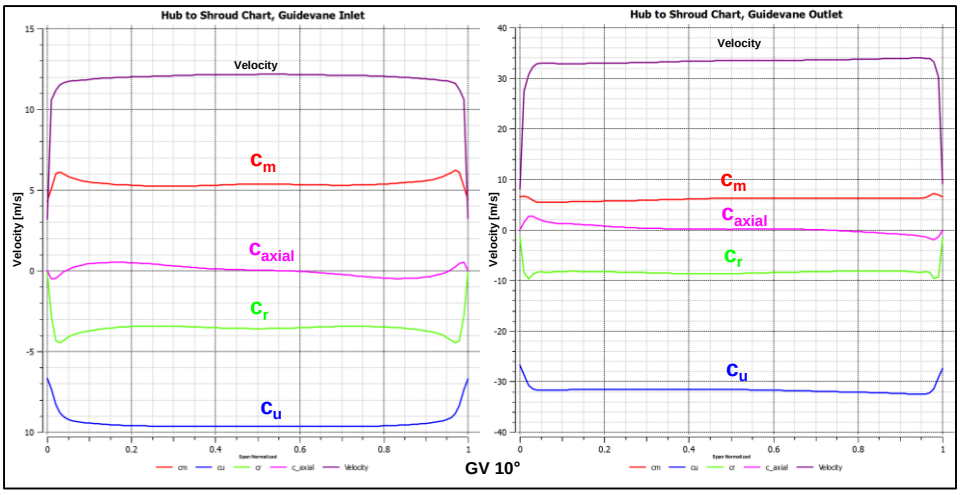

Figure 2.39 : Velocities at guide vane inlet and outlet, part load operation

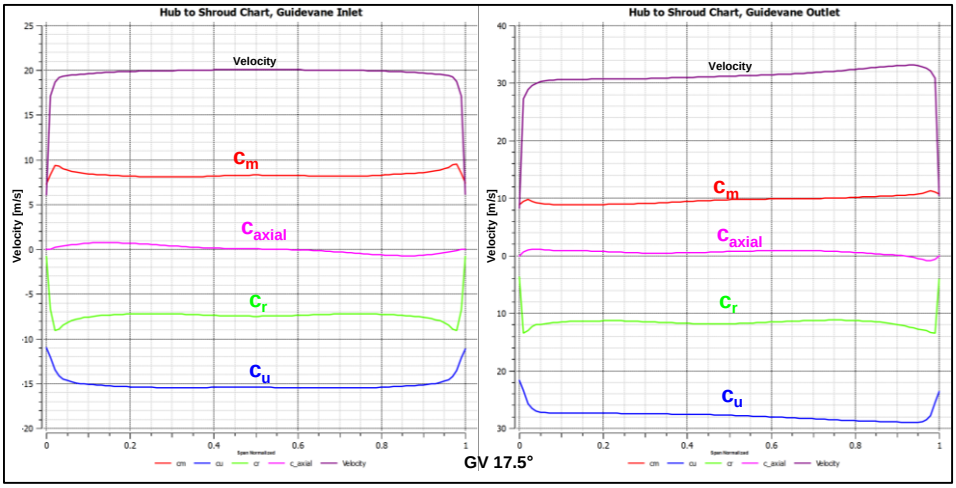

Figure 2.40 : Velocities at guide vane inlet and outlet, BEP

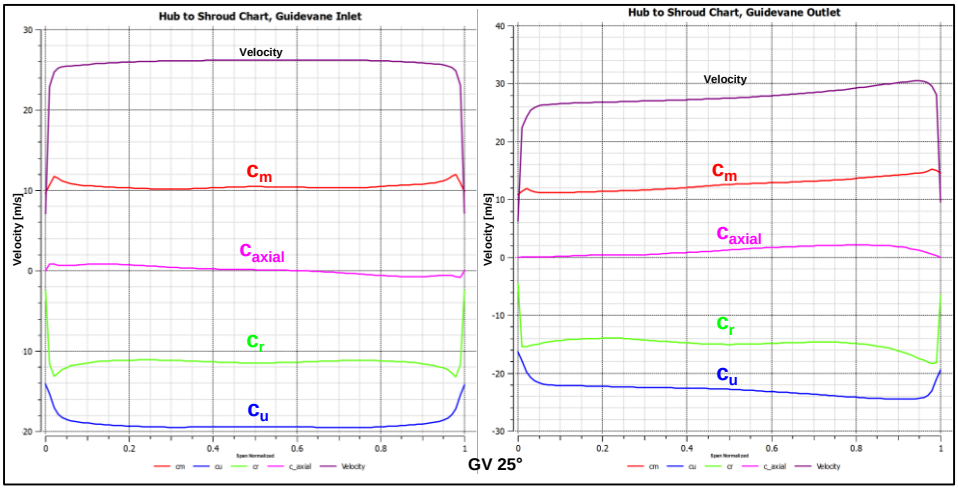

Figure 2.41 : Velocities at guide vane inlet and outlet, overload operation

The guide vane adjustment torque is shown in absolute values in Figure 2.42 and in normalized values in Figure 2.43. The maximum torque is at a guide vane opening of 12.5° (flow rate of approx. 30 m³/s).

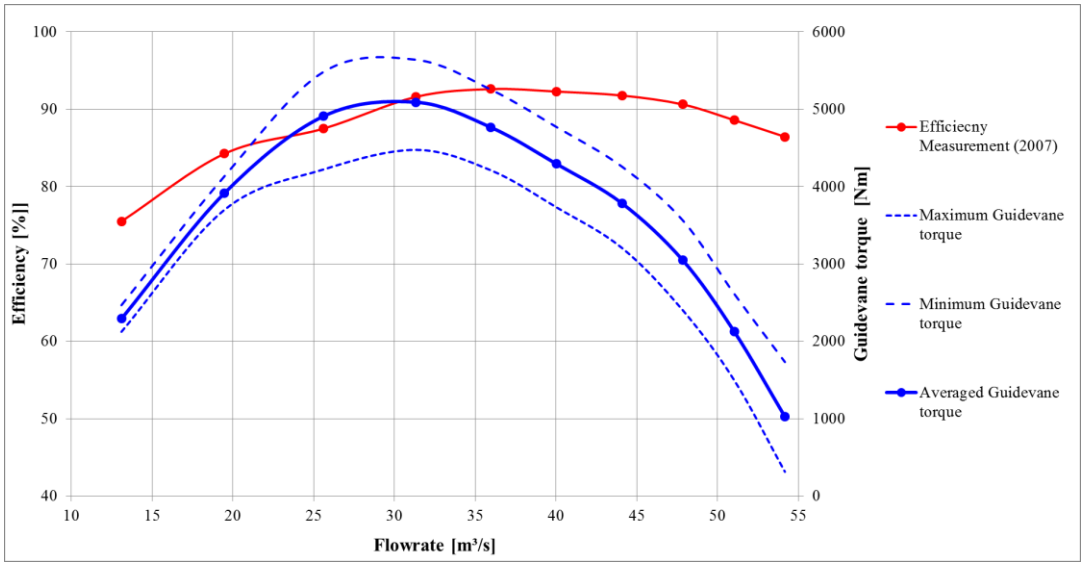

Figure 2.42 : Guide vane torque for one guide vane

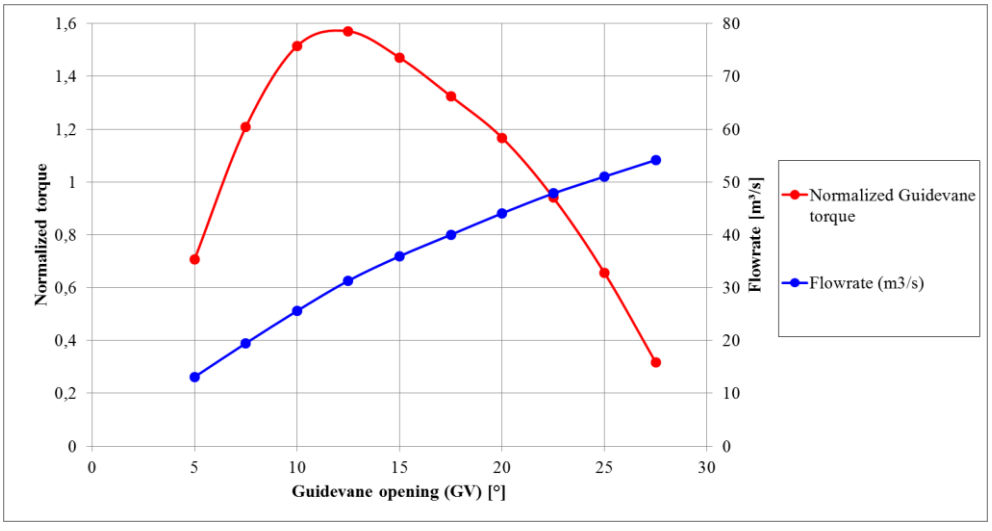

Figure 2.43 : Guide vane torque, normalized M11 for one guide vane

2.5.5 Runner

To investigate the flow situation through the runner at inlet and outlet, post-processing planes were generated (Figure 2.44). These blades are located at different streamwise locations, so-called blade aligned surfaces. For this purpose the software uses the first 25% for the area upstream the blade and from 75% to 100% for the downstream area (the blade is between 25% and 75%). A streamwise location 1.02 means just behind the guide vane to runner interface and a streamwise location 1.99 means just before the runner to draft tube interface. The streamwise location 1.23 is immediately upstream of the leading edge and 1.8 downstream of the trailing edge. Subsequently, on these planes averaged values (area-averaged circumferential) are created and analyzed in Figure 2.45.

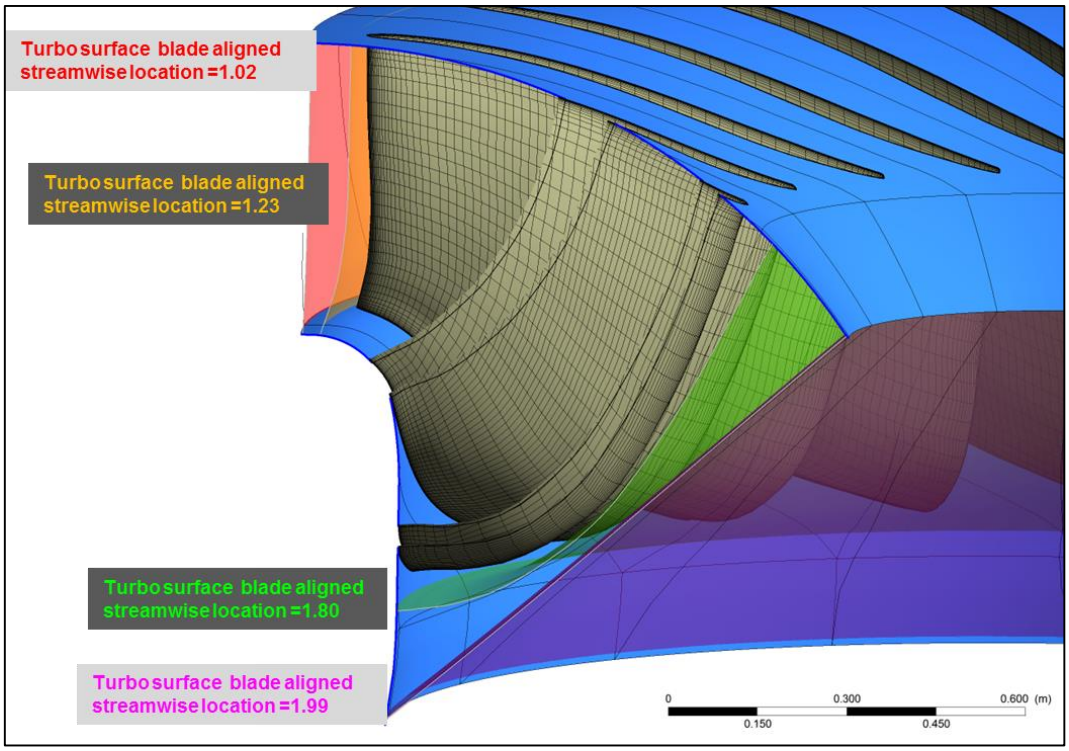

Figure 2.44 : Runner post-processing, location of turbo surfaces

As this is a counter rotating machine against the chosen coordinate system orientation, the c_u-value is negative. This c_u-value generated by the spiral and the guide vane is then the "energy" converted into torque in the runner. The c_u-value at the runner outlet is almost zero, and so almost no swirl (swirl = rc_u) remain. Taking the design point of a runner as a basis, it is also desirable to gain an almost constant c_m-distribution at the runner outlet. A small amount of remaining swirl at the shroud side of the runner is welcome, as this swirl stabilizes the draft tube flow situation downstream.

The difference between Figure 2.45 and Figure 2.46 is that for the first figure the post-processing plane is close to the leading and trailing edge and that for the second figure the planes are a bit far away from leading and trailing edge (closer to the interfaces between guide vane and runner as well as runner and draft tube). Thus, the flow situation in Figure 2.46 is a bit smoother, however tendencies are the same. The c_r-value also decreases and the higher amount of c_r in the shroud region is reduced. There is almost no media transfer normal to the main flow direction.

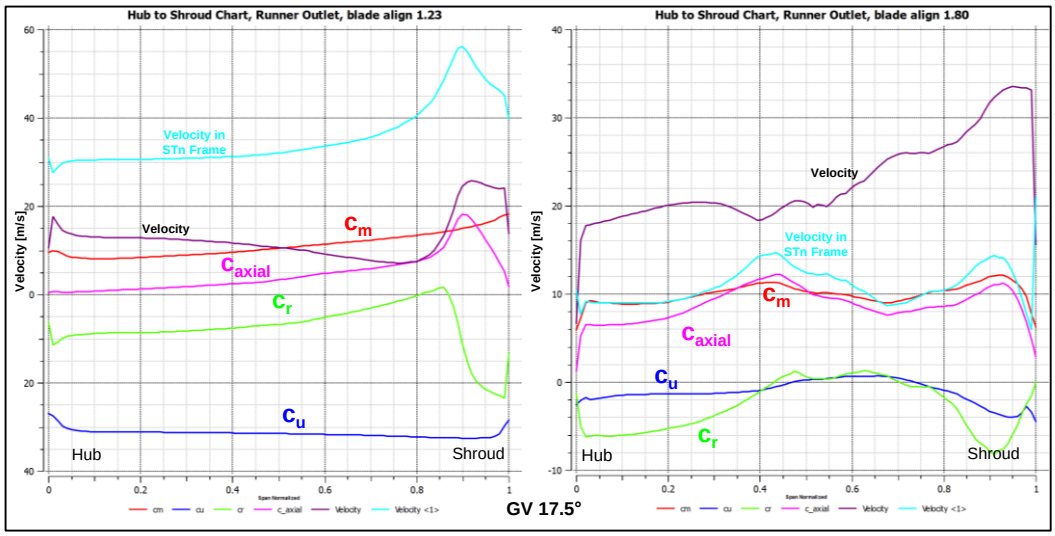

Figure 2.45 : Velocity situation at inlet and outlet of the runner, BEP, streamwise locations 1.23 and 1.80

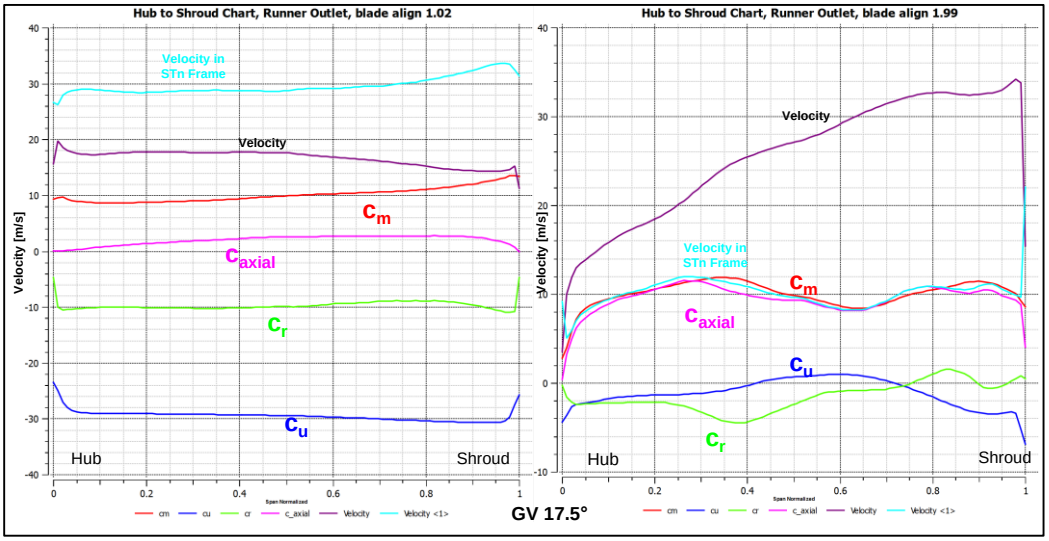

Figure 2.46 : Velocity situation at inlet and outlet of the runner, BEP, streamwise locations 1.02 and 1.99

Regarding the pressure situation, consequently there is a reduction of the head along the streamwise direction in the runner (see Figure 2.47). As this is also an averaged value there is no effect visible on the suction and pressure side. The blue line in Figure 2.47 depicts the static pressure. The red line indicates the total pressure (in this figure also an averaged value) for which the kinetic amount is added to the static pressure. The green line indicates the amount of the meridional velocity. The space between the red and the green line is almost the c_u-component of the velocity and decreases whereas the radial and meridional components are almost constant.

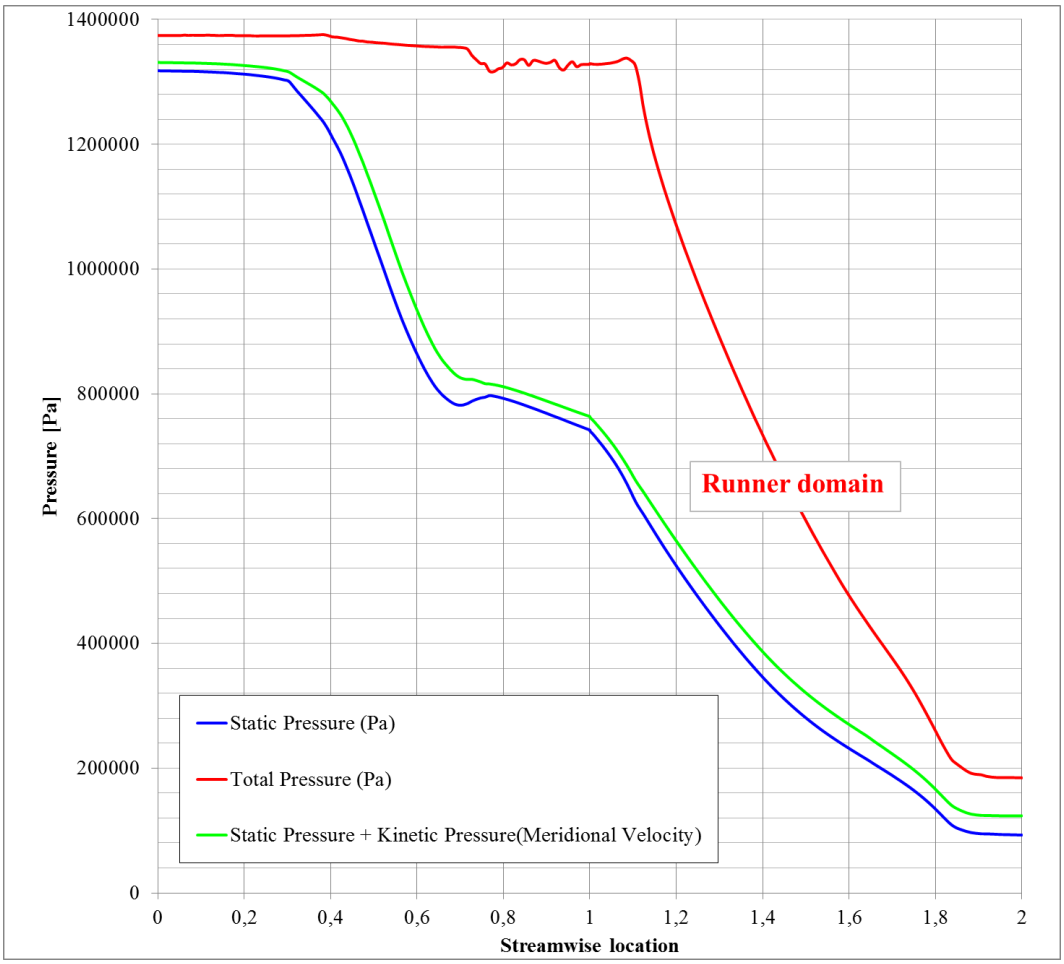

Figure 2.47 : Pressure along guide vane and runner, part load operation

The pressure plot (Figure 2.48) shows an extremely low pressure zone at the suction side of the blade close to the runner shroud. The stagnation point of the flow at the runner hub is at the pressure side and the flow circulates around the leading edge from pressure to suction side with high velocities. This effect becomes stronger for overload operation. The stagnation point moves from the pressure side closer to the leading edge, nevertheless this effect becomes stronger.

During the site visit, cracks could be found at the leading edge of the runner. These cracks could not only be found on one runner blade but on every single runner blade. Figure 2.49 shows two photos of the cracks of the runner blades at the leading edge. The high velocities realized in the numerical simulation were found exactly at these

locations. The cracks have a length of about 20 to 30 mm and are approx. 5 to 10 mm deep. Figure 2.48 shows a picture of the inspection report where the cavitation damages also could be found at the suction side.

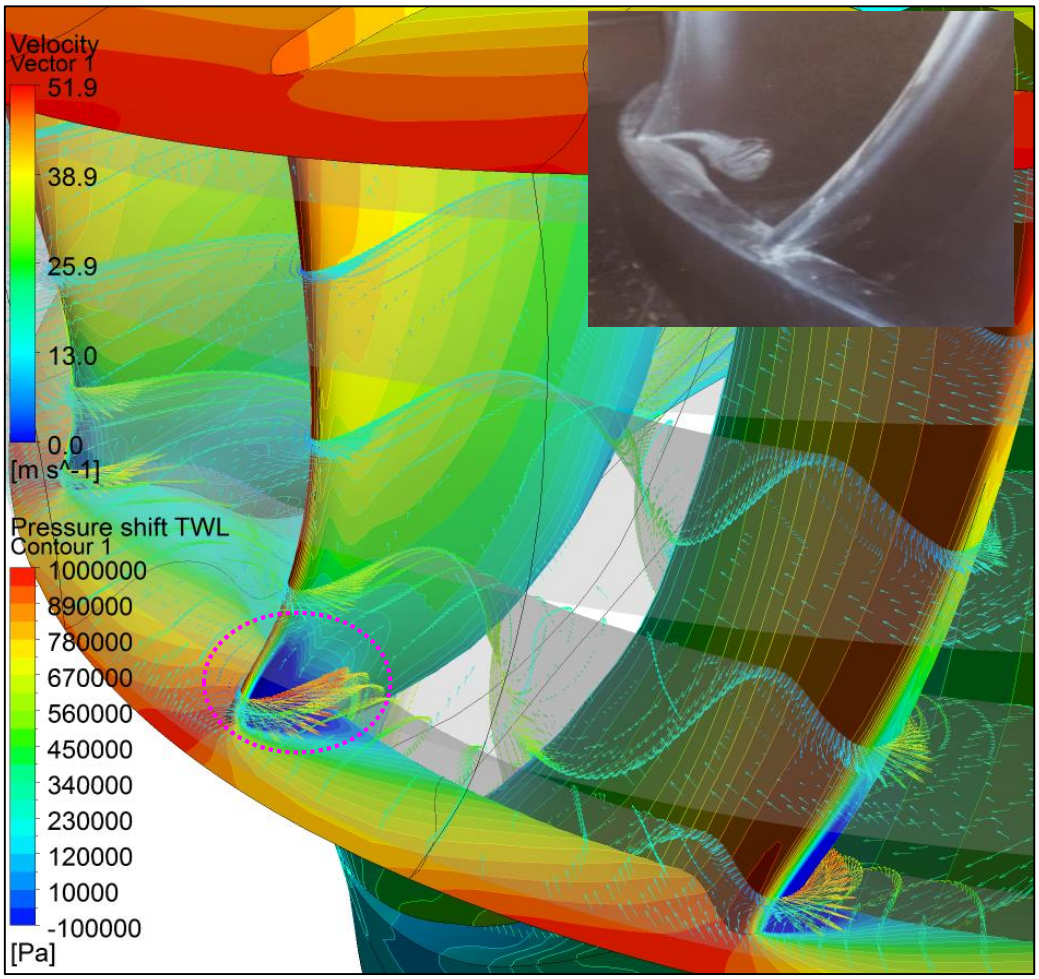

Figure 2.48 : Left – pressure and vector plot for BEP, right – report photo, both views from the suction side

Figure 2.49 : Cracks in the runner blades, view of the pressure side

2.5.6 Draft Tube

The area distribution of the draft tube was realized in a classical way for the original draft tube. After the first cone, an almost constant area distribution could be found in the L-bow. Thus, flow separations were suppressed regularly (area distributions along the draft tube length which led to accelerated mean velocities are also known). With the installation of the stand pipe, the opening angle becomes higher and steeper (see Figure 2.52). Furthermore, a second region of a constant area distribution is located in the section of the conical standpipe (see Figure 2.50). The post-processing planes are shown in Figure 2.51. At each plane, static and total pressure, area and velocities are evaluated.

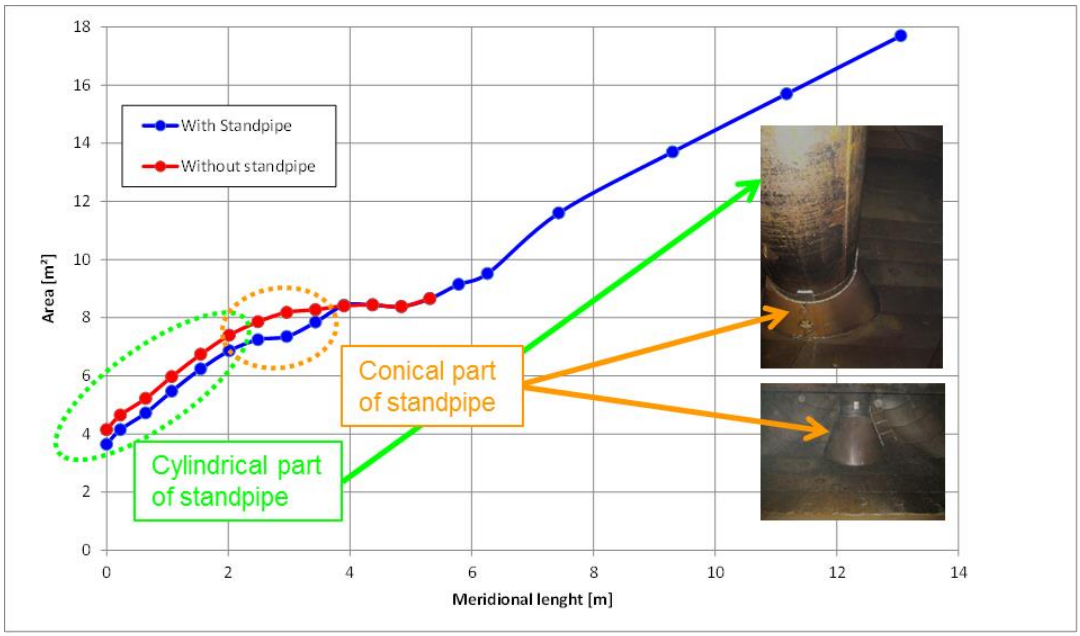

Figure 2.50 : Area distribution of the draft tube

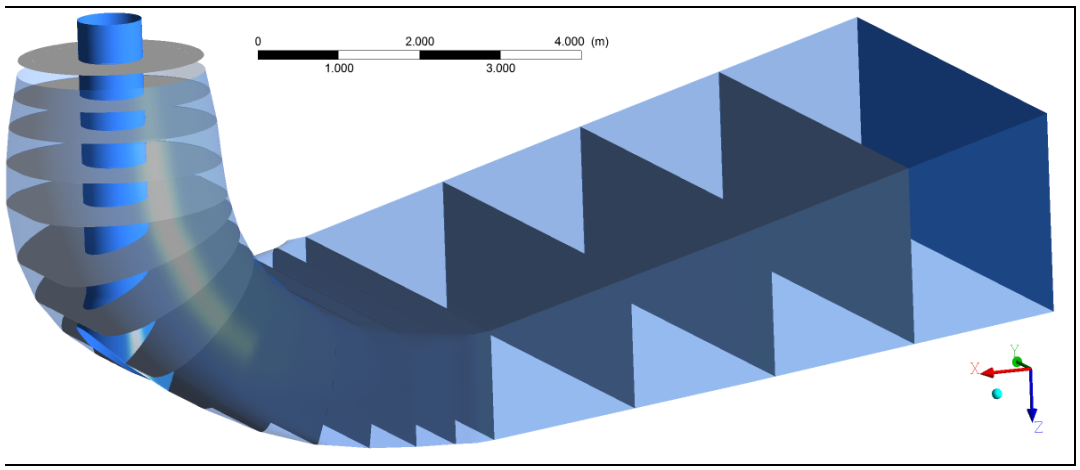

Figure 2.51 : Planes for post-processing at draft tube, draft tube with standpipe

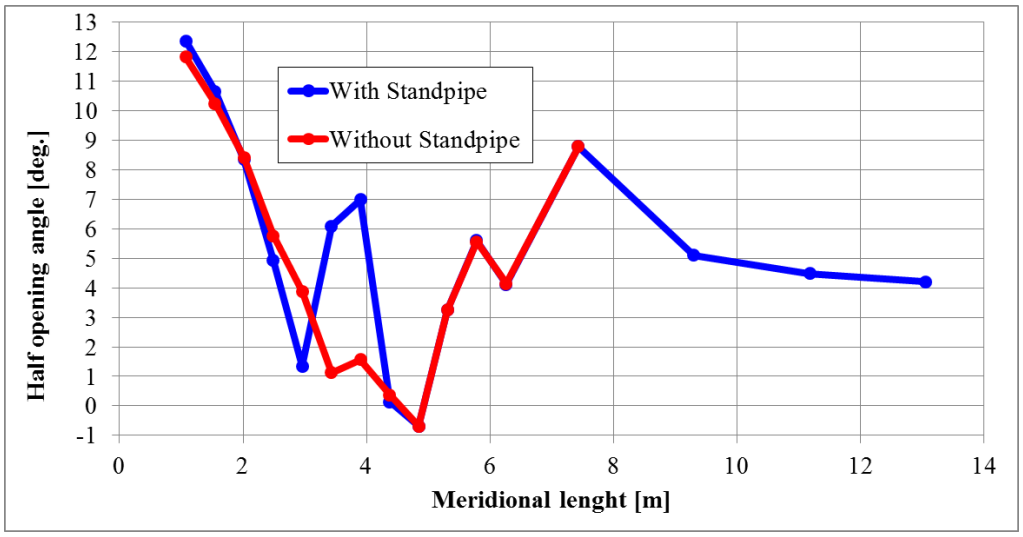

Figure 2.52 : Half opening angle of the draft tube versus meridional length

With these evaluated values, Figure 2.53 is established to understand the pressure recovery a bit more in detail. The static pressure is depicted in red (increase of static pressure for increasing length), and the total pressure in green (decreasing total pressure for increasing length) is shown. Additionally, a line with the static pressure plus the dynamic pressure is drawn in blue, whereas for the velocity the flow rate divided by the area ($V_{plane} = Q/A_{plane}$) is used. The difference between this blue line ($p + \rho V^2/2$) and the green line (total pressure) are velocities in other directions than normal to the plane.

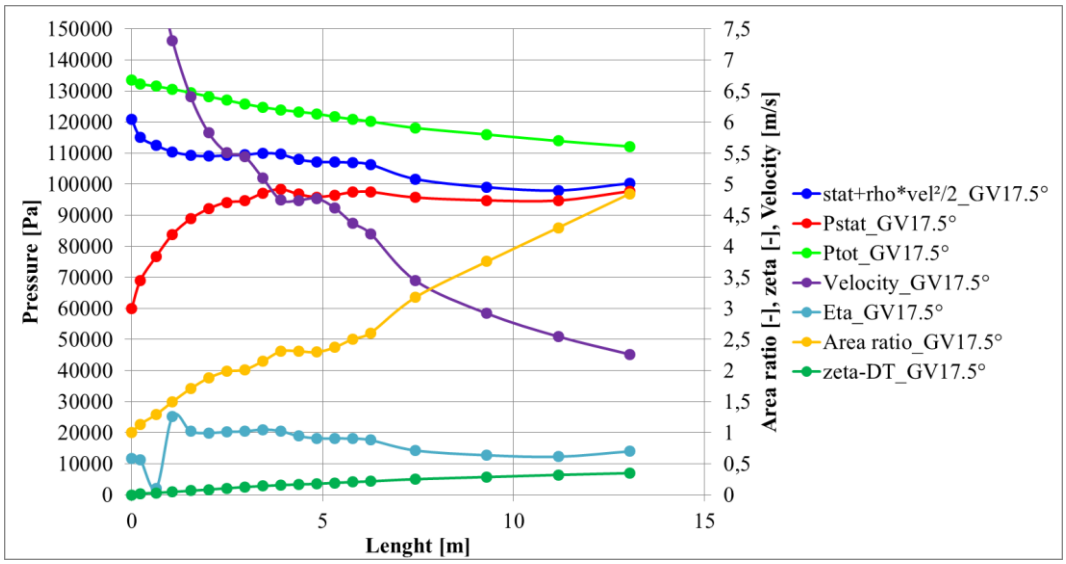

Figure 2.53 : Characteristic values along the draft tube

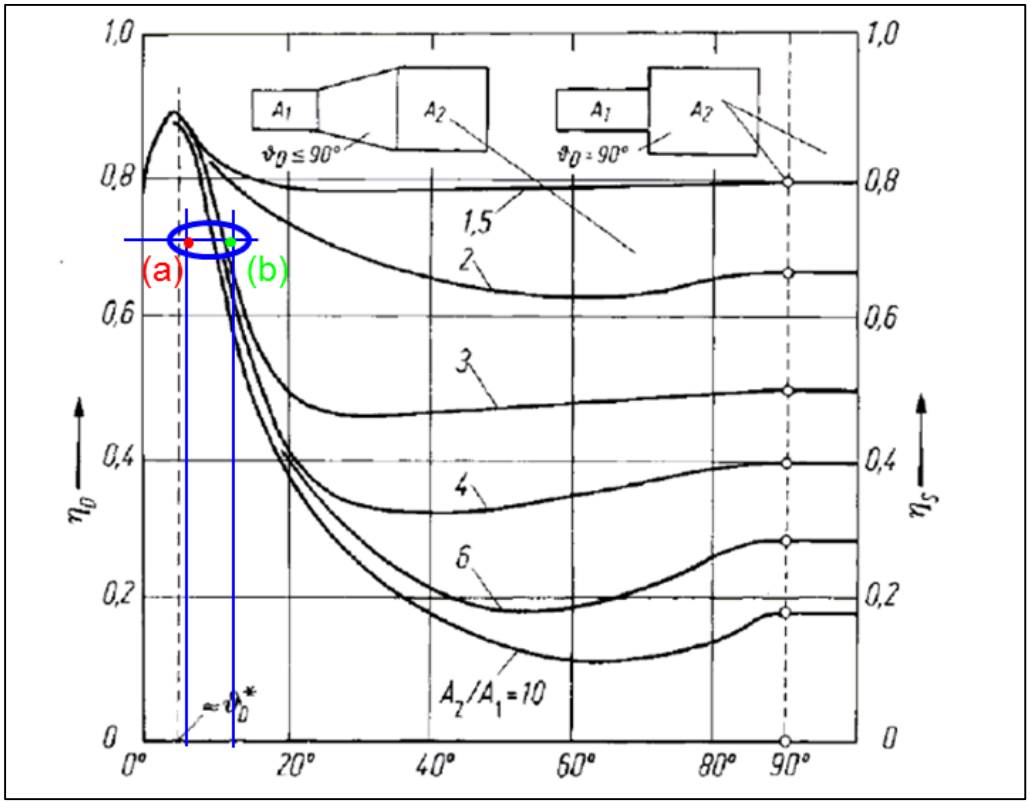

Figure 2.54 : Diffusor efficiency as function of the diffusor opening angle [23]

The η-value in Figure 2.53 is the diffuser efficiency based on Truckenbrodt, which yields values of about 0.7 after the bend. This fits to the theory stating that both the opening angle of the draft tube and the remaining swirl in the flow distribution influence the performance. In Figure 2.54, the performance $\eta_{Diffusor}$ is included into the diagram. The draft tube opening angle between the inlet and outlet draft tube area is estimated to be 5.7° when using a straight "substitution"-cone with the same area ratio (point (a) in Figure 2.54). In Figure 2.52, the opening angle is calculated from segment to segment, and it is about 12° at the beginning of the draft tube. Therefore, point (b) is marked in Figure 2.54.

In Figure 2.55, the loss coefficient ξ is plotted along the draft tube. The lowest value of ξ is for the 17.5° guide vane angle with a flow rate of $Q = 40.01$ m³/s.

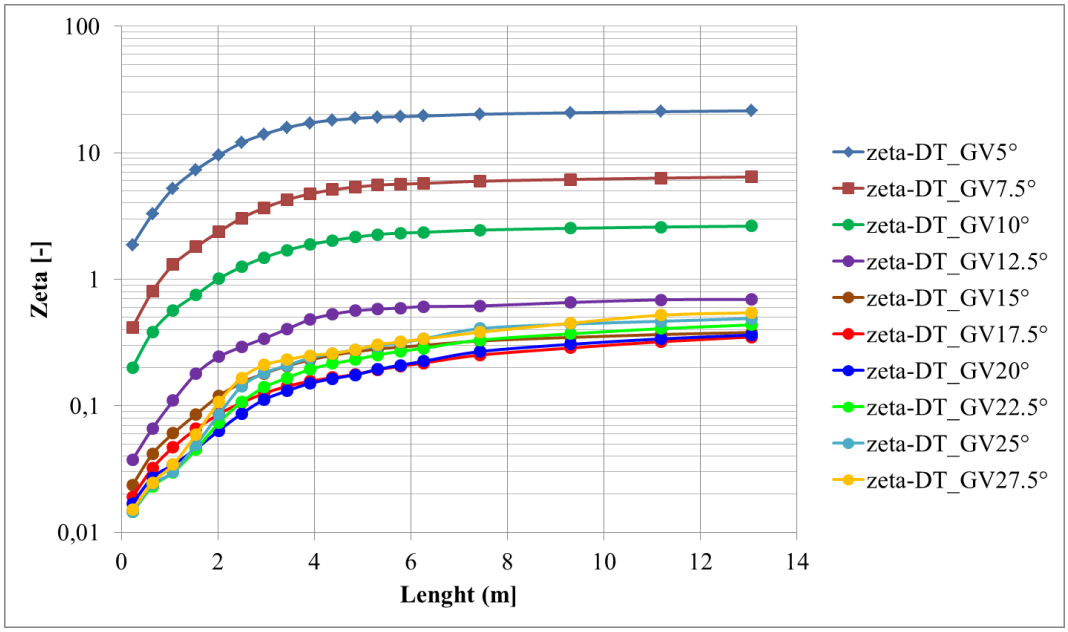

Figure 2.55 : Loss coefficient ξ for different operation points, H=130.7 m, flow rate Q=13.1 m³/s up to Q=54.2 m³/s

Streamlines were plotted in the draft tube in Figure 2.56 to Figure 2.58 for part load, best efficiency point (BEP) and overload. The turbine unit rotates anti-clockwise. (The positive z-axis follows the flow into the draft tube.)

In part load almost all of the flow went to the right side of the draft tube (in flow direction), and in overload – vice versa – a high amount of the mass flow went through the left side of the draft tube. For the nominal operation point the influence of the stand pipe can be seen, where there is a swirly flow situation in the middle of the draft tube (see Figure 2.57).

At BEP and overload conditions still backflow situations in the draft tube occur, see Figure 2.59 (part load), Figure 2.60 (BEP) and Figure 2.61 (overload).

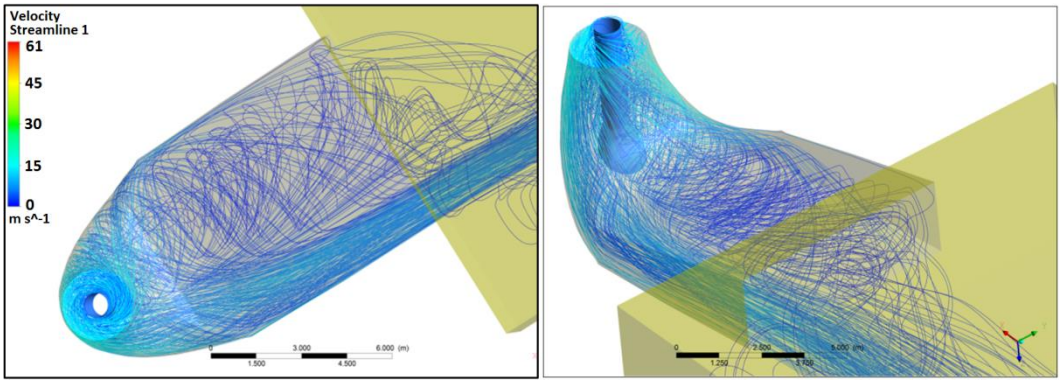

Figure 2.56 : Streamlines, GV 10°, *Q*=25.6 m³/s, part load, left – view in direction of the machine axis, right – 3D view

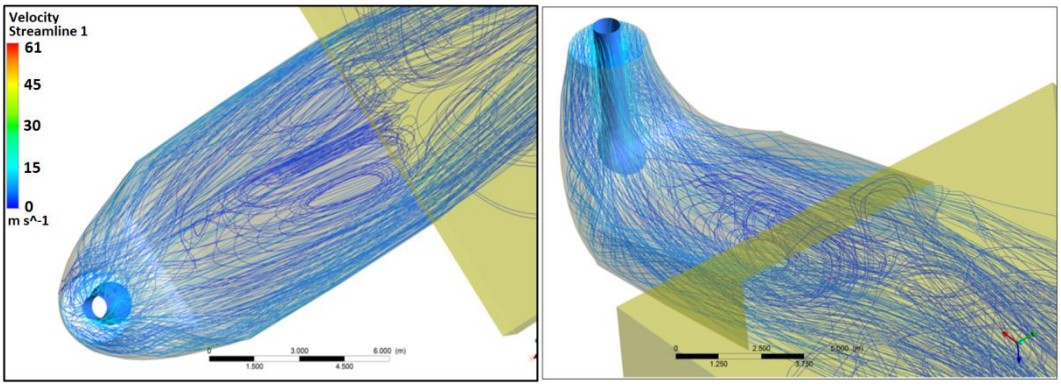

Figure 2.57 : Streamlines GV 17.5°, *Q*=40.0 m³/s, BEP, left – view in direction of the machine axis, right – 3D view

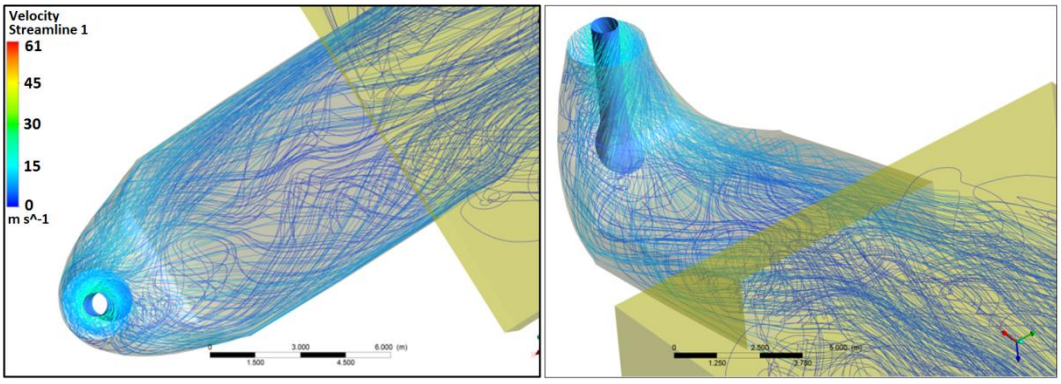

Figure 2.58 : Streamlines GV 25°, *Q*=51.0 m³/s, overload, left – view in direction of the machine axis, right – 3D view

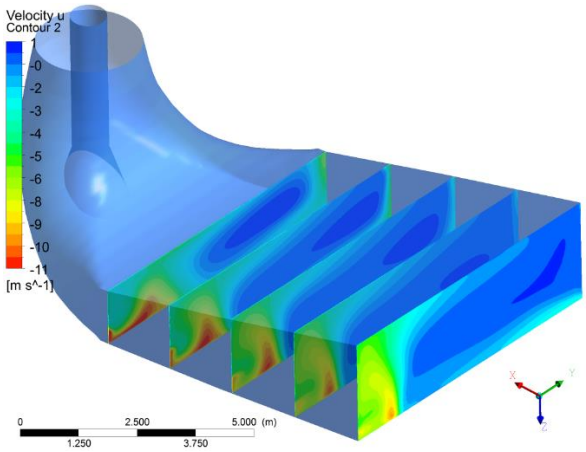

Figure 2.59 : Velocity contour plot, GV 10°, *Q*=25.6 m³/s, part load

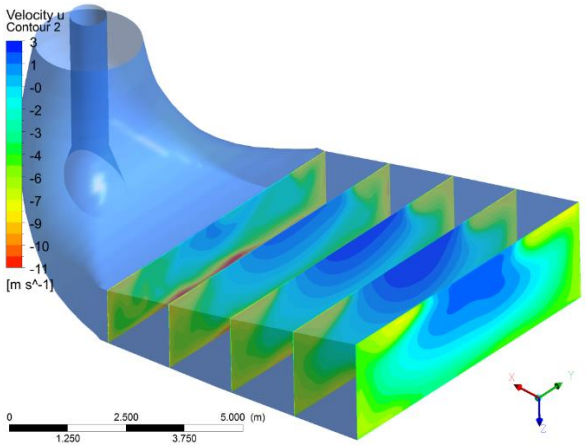

Figure 2.60 : Velocity contour plot, GV 17.5°, *Q*=40.0 m³/s, BEP

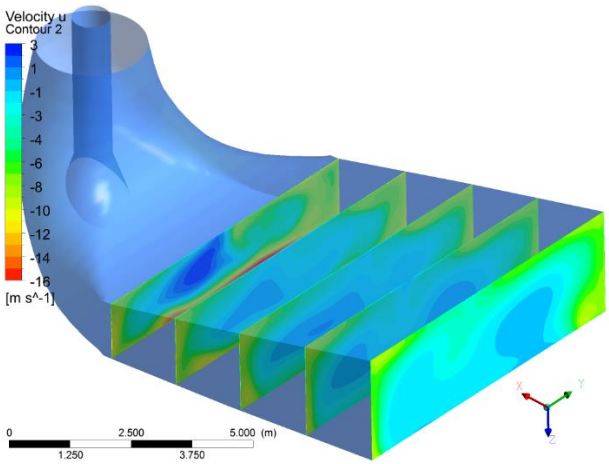

Figure 2.61 : Velocity contour plot, GV 25°, *Q*=51.0 m³/s, overload

2.5.7 Influence of the standpipe

The influence of the draft tube can be seen in Figure 2.62, where the shorter draft without standpipe tube is compared to the shorter draft tube with the standpipe as well as to the existing longer one with the standpipe. The differences between the green and blue lines characterize the influence of the standpipe and therefore in overload a small difference between these two could be found – a small negative influence of the stand pipe. The draft tube length has an influence on the system as more losses occur, simply like a longer pipe.

No influence on the other components is detectable. For the longer version of the draft tube including the standpipe, the optimum efficiency point lies closer to the measurement campaign (comparison to measurement of 2007).

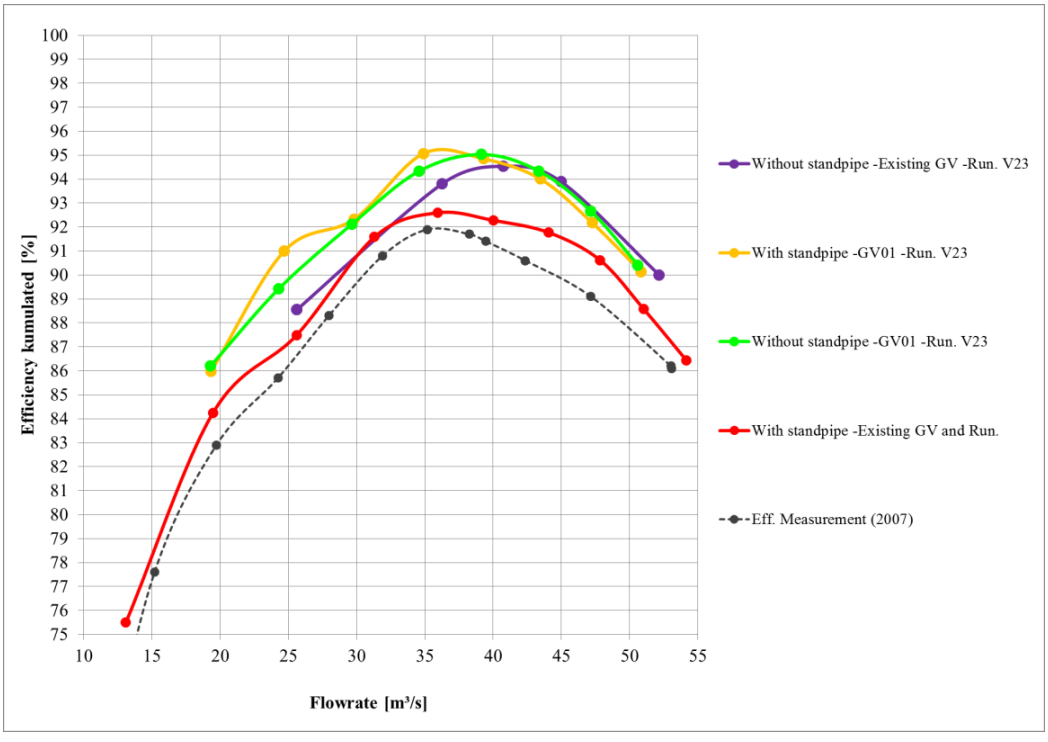

Figure 2.62 : Influence of the standpipe

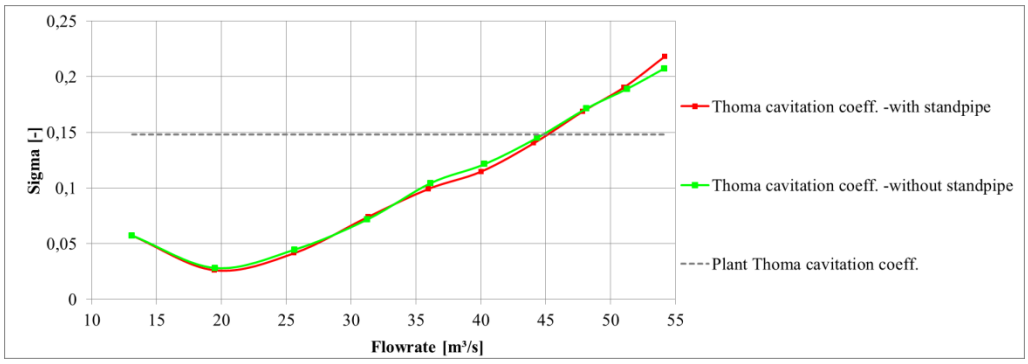

Figure 2.63 : Influence of the standpipe on Thoma Cavitation Coeff.

2.5.8 Numerical hill chart and comparison with literature

The calculations were carried out for different heads. Then, a hill chart was generated and depicted in Figure 2.64. The optimum of the machine is reached at a flow rate of 37 m³/s and a head of 125 m. The numerical efficiency is about 93% – this is the pure hydraulic efficiency without leakage losses and disc friction losses. The efficiency is normalized with the best efficiency point.

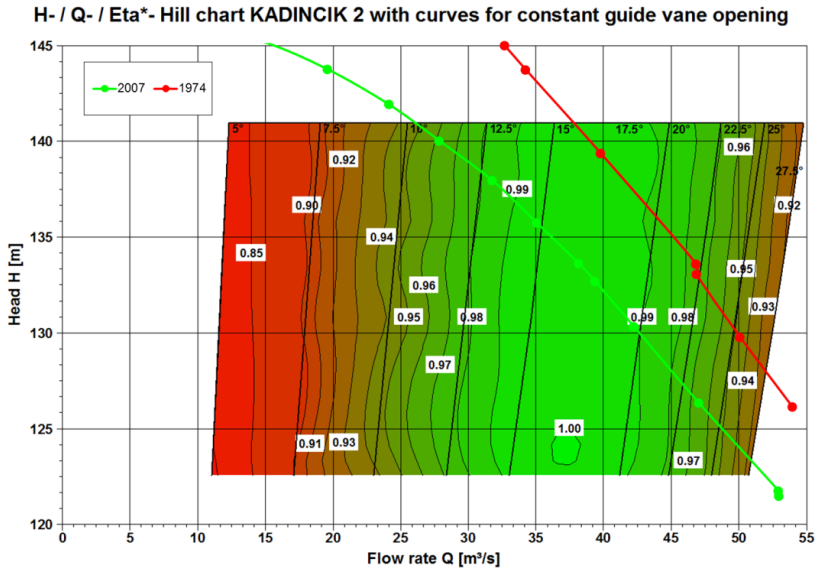

Figure 2.64 : Numerical hill chart

According to Figure 2.65, the losses in the Francis turbine are about 7.5% for the given specific speed. As this figure is about 30 years old, it is a good basis for comparison with existing power plant. As far as losses are concerned, 3.2% refer to the spiral, stay vane and guide vane. This amount corresponds to the results of the numerical simulation. Guide vane and spiral losses (including stay vanes) are about 3.1%. The losses of the runner are also at a similar level, 2.1% losses. The draft tube losses are higher in the numerical simulation as in the picture presented (Figure 2.65 left).

Figure 2.65 left is for a standardized Reynolds number of 10,000,000. For this plant, the Reynolds number is about 105,000,000 and so the overall efficiency has to decrease by 0.28% according to IEC60193 [24].

In Figure 2.66, the correlation between the flow rate *Q* and the guide vane opening angle is shown together with the servo piston travel for different heads. Additionally, the wicket gate opening *a0* is displayed.

Finally, Table 2-5 presents the results for different heads in a tabular form with calculated standardized values.

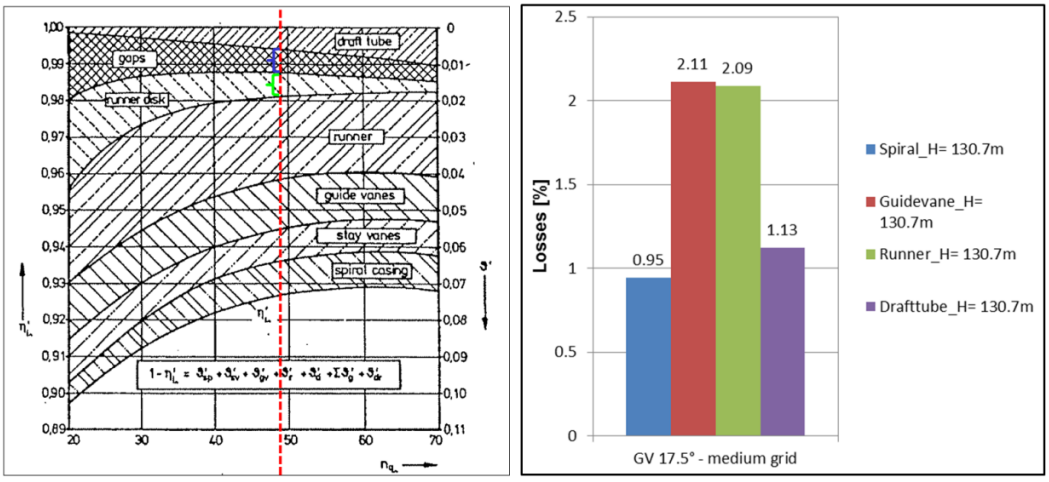

Figure 2.65 : Francis turbine losses as function of the specific speed

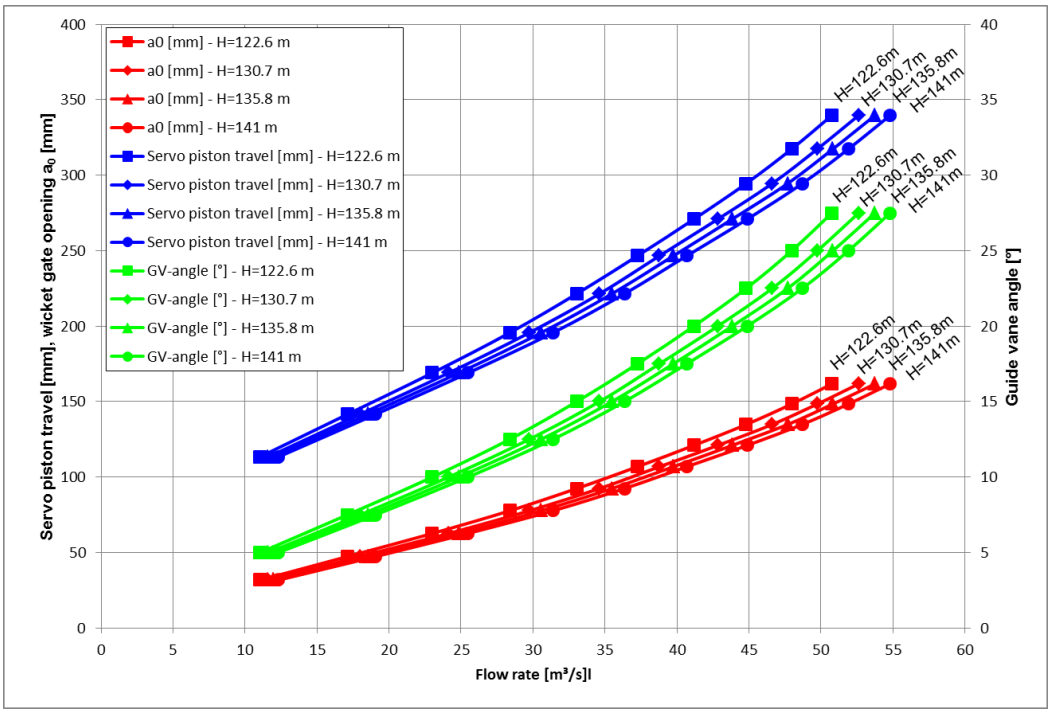

Figure 2.66 : Flow rate versus guide vane opening for different heads

Table 2-5 : Results for the numerical simulation, standardized values

Q	H	P	eff_{CFD}	PHI	PSI	n_q	Q_{ED}	Q_{11}	n_{ED}	n_{11}	GV-angle	a_0	Servo piston travel
[m³/s]	[m]	[MW]	[%]	[-]	[-]	[rpm]	[-]	[-]	[-]	[-]	[°]	[mm]	[mm]
11.04	122.57	11.09	73.18	0.05	1.46	27.06	0.05	0.15	0.37	69.91	5	31.8	113.4
17.11	122.57	18.79	83.64	0.08	1.46	33.69	0.07	0.23	0.37	69.91	7.5	47.4	141.6
23.01	122.57	25.64	86.68	0.11	1.46	39.07	0.10	0.31	0.37	69.91	10	62.7	169.0
28.38	122.57	32.43	89.93	0.13	1.46	43.39	0.12	0.39	0.37	69.91	12.5	77.7	195.6
33.03	122.56	38.27	91.85	0.16	1.46	46.81	0.14	0.45	0.37	69.91	15	92.4	221.4
37.25	122.56	43.28	92.57	0.18	1.46	49.71	0.16	0.51	0.37	69.91	17.5	106.8	246.5
41.18	122.56	47.29	91.84	0.19	1.46	52.26	0.18	0.56	0.37	69.91	20	121.0	270.9
44.81	122.56	50.58	90.52	0.21	1.46	54.52	0.19	0.61	0.37	69.91	22.5	134.9	294.5
47.98	122.56	52.88	88.58	0.23	1.46	56.41	0.21	0.65	0.37	69.92	25	148.4	317.4
50.76	122.56	54.04	85.68	0.24	1.46	58.03	0.22	0.69	0.37	69.92	27.5	161.7	339.7
11.61	130.74	12.68	75.05	0.05	1.56	26.44	0.05	160.37	0.36	510.40	5	31.8	113.4
17.99	130.74	21.04	83.85	0.08	1.56	32.91	0.08	199.59	0.36	349.12	7.5	47.4	141.6
24.14	130.74	28.72	87.01	0.11	1.56	38.12	0.10	231.19	0.36	276.52	10	62.7	169.0
29.74	130.74	36.36	90.44	0.14	1.56	42.31	0.12	256.61	0.36	231.65	12.5	77.7	195.6
34.62	130.73	42.96	92.43	0.16	1.56	45.66	0.15	276.88	0.36	204.41	15	92.4	221.4
38.78	130.73	47.85	92.32	0.18	1.56	48.32	0.16	293.03	0.36	188.54	17.5	106.8	246.5
42.84	130.73	52.29	91.64	0.20	1.56	50.79	0.18	307.99	0.36	176.41	20	121.0	270.9
46.62	130.73	56.00	90.43	0.22	1.56	52.98	0.20	321.31	0.36	167.56	22.5	134.9	294.5
49.76	130.73	58.12	88.09	0.23	1.56	54.74	0.21	331.95	0.36	162.96	25	148.4	317.4
52.62	130.73	59.33	85.15	0.25	1.56	56.29	0.22	341.36	0.36	160.46	27.5	161.7	339.7
11.97	135.85	13.71	76.03	0.06	1.62	26.09	0.05	158.21	0.35	490.64	5	31.8	113.4
18.53	135.85	22.53	84.07	0.09	1.62	32.46	0.08	196.84	0.35	338.09	7.5	47.4	141.6
24.84	135.84	30.78	87.35	0.12	1.62	37.58	0.10	227.89	0.35	267.58	10	62.7	169.0
30.56	135.84	38.89	90.71	0.14	1.62	41.68	0.13	252.76	0.35	224.53	12.5	77.7	195.6
35.48	135.84	45.62	92.25	0.17	1.62	44.91	0.15	272.36	0.35	199.20	15	92.4	221.4
39.75	135.84	50.88	92.25	0.19	1.62	47.53	0.16	288.26	0.35	183.54	17.5	106.8	246.5
43.84	135.84	55.41	91.39	0.21	1.62	49.92	0.18	302.75	0.35	172.17	20	121.0	270.9
47.69	135.84	59.35	90.22	0.23	1.62	52.07	0.20	315.78	0.35	163.51	22.5	134.9	294.5
50.84	135.83	61.41	87.73	0.24	1.62	53.76	0.21	326.02	0.35	159.38	25	148.4	317.4
53.76	135.83	62.72	84.85	0.25	1.62	55.28	0.22	335.26	0.35	156.88	27.5	161.7	339.7
12.33	140.95	14.78	76.94	0.06	1.68	25.75	0.05	156.14	0.35	472.59	5	31.8	113.4
19.07	140.95	24.02	84.12	0.09	1.68	32.02	0.08	194.21	0.35	328.28	7.5	47.4	141.6
25.49	140.95	32.69	87.28	0.12	1.68	37.03	0.10	224.55	0.35	260.49	10	62.7	169.0
31.38	140.95	41.44	90.83	0.15	1.68	41.08	0.13	249.16	0.35	218.05	12.5	77.7	195.6
36.35	140.95	48.41	92.18	0.17	1.68	44.22	0.15	268.16	0.35	194.06	15	92.4	221.4
40.67	140.95	53.85	92.04	0.19	1.68	46.77	0.16	283.64	0.35	179.16	17.5	106.8	246.5
44.88	140.94	58.78	91.34	0.21	1.68	49.13	0.18	297.97	0.35	167.77	20	121.0	270.9
48.71	140.94	62.61	89.87	0.23	1.68	51.18	0.20	310.40	0.35	160.02	22.5	134.9	294.5
51.91	140.94	64.80	87.41	0.25	1.68	52.84	0.21	320.46	0.35	155.95	25	148.4	317.4
54.81	140.94	65.93	84.36	0.26	1.68	54.30	0.22	329.27	0.35	153.93	27.5	161.7	339.7

CHAPTER 3

DESIGN IMPROVEMENT

In this chapter, based on the CFD analysis results of the existing turbine, new guide vane and runner blade are designed and results are compared. 25 different optimization versions are prepared progressively. At the end two different optimization scenarios are offered based on their energy production performances for further feasibility studies.

3.1 Guide Vanes

Performance of the existing guide vane is already evaluated in Chapter 2.5.4. It seen that the stagnation point of the existing guide vane is not directly on the leading edge for all guide vane angles (Figure *3.2* left), except the maximum opened position. An ideal guide vane design shall have a stagnation point at the leading edge when the turbine operates at the design point. The stay vanes are not changed and the guide vane flow inlet angle is fixed so, to shift the stagnation point to the leading edge guide vane profile has to be changed. The other target is keeping the outflow angle unchanged. To achieve this two NACA profiles are used for comparison. One is straight NACA0018 (called as V01), the other is bended NACA0014 (called as V02). Both profiles are analyzed with the all other parts remaining the same. In Figure 3.1, existing guide vane and proposed new guide vane geometries are presented. In Figure 3.2, middle and right plots show the pressure distribution over the V01 and V02 profiles.

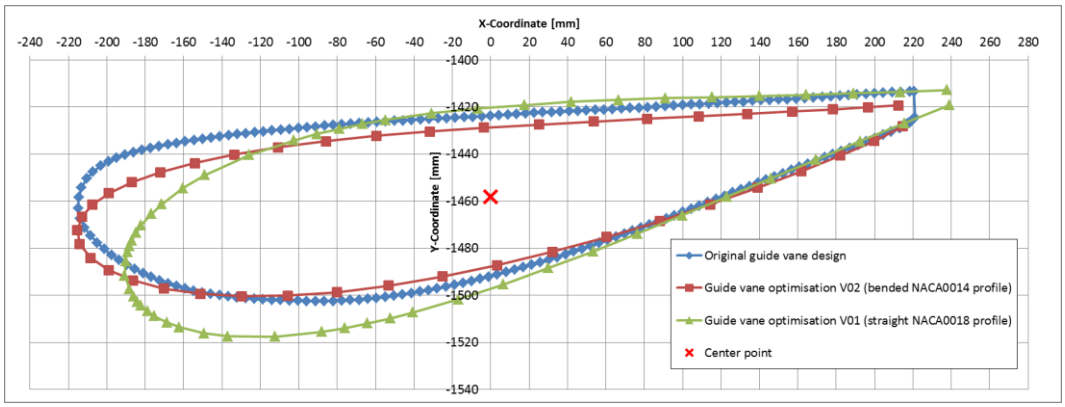

Figure 3.1 : Comparison of different guide vane geometries

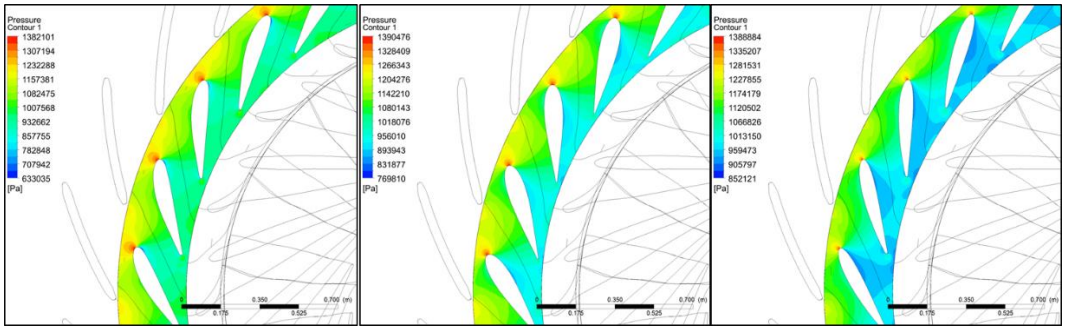

Figure 3.2 : Guide vane stagnation points for different guide vane profiles

It is seen that on both new designs the flow profiles are changed where the V01 profile has the stagnation point directly at the leading edge and V02 profile has it slightly on the suction side but still better than the original guide vane.

In Figure 3.3 (left), the efficiency curves of different guide vane designs are plotted. At the graph on the right side, the spiral case efficiency including the stay vanes are added to the guide vane efficiency values. The V01 profile has better overall efficiency compare to the original one. Below the 35 m^3/s flowrate the difference is more than 1 percent. The V02 profile has almost 0.5 percent higher efficiency over

the whole range than the original guide vane. The maximum flow rate of the turbine is just above 50m^3/s, and thus the annual production will significantly increase with version 1.

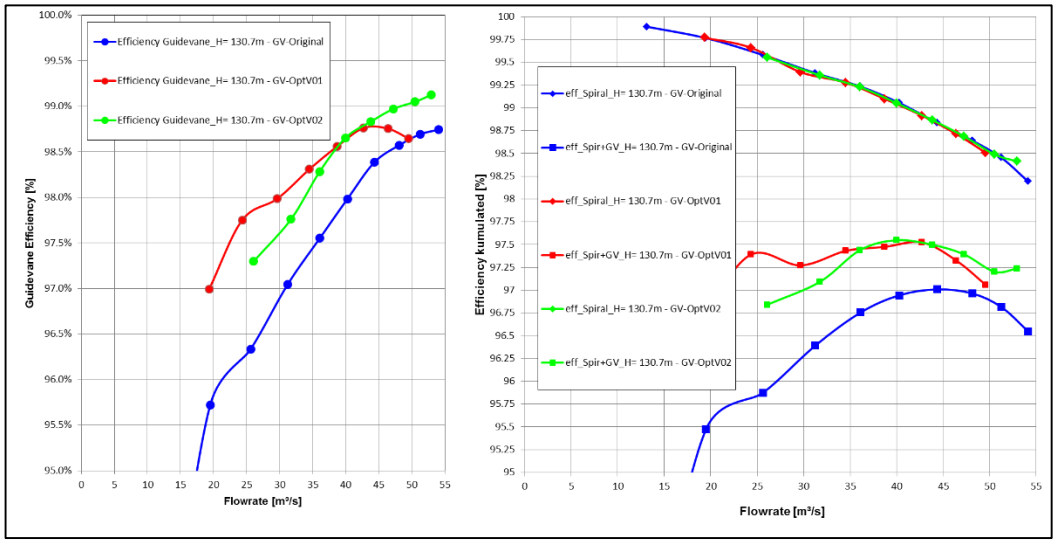

Figure 3.3 : Guide vane efficiency curves

Adjustment torques of guide vanes are also calculated and given in Figure 3.4. The original guide vane profile has a maximum average torque of 5000 Nm at 30 m^3/s flowrate. The maximum and minimum curves represent the torques on different guide vane blades with the same setting. The reason of the different torques on blades is the uneven velocity distribution on the stay vane outlets. V01 has negative torque values and the amplitude is significantly lower than the original so, to adjust the guide vanes bigger servo piston is not needed.

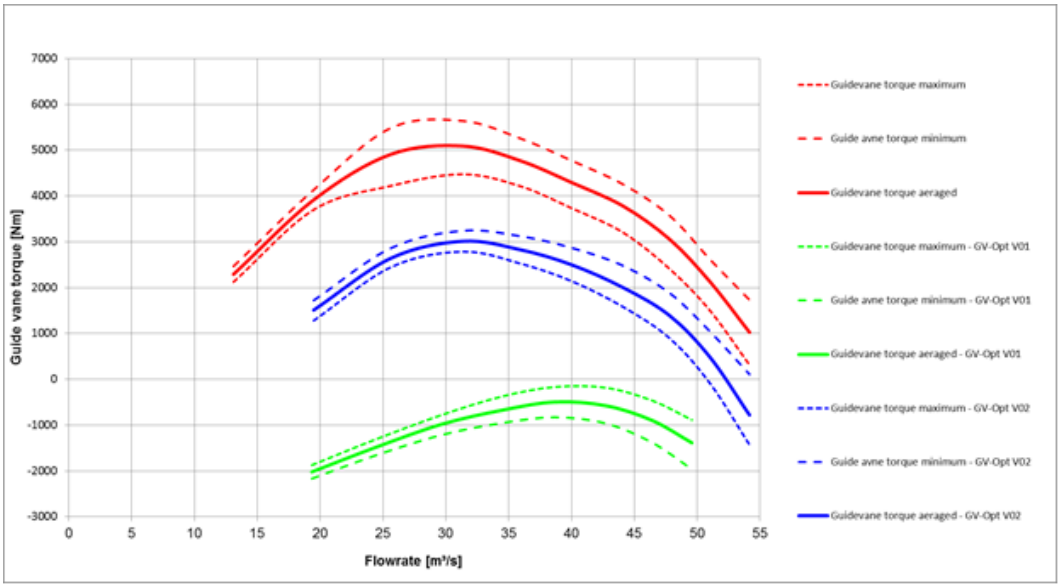

Figure 3.4 : Guide Vane adjustment torques

3.2 Stay Vanes

For the modified stay vane, the existing stay vanes (red in Figure 3.5) were extended upstream (blue in Figure 3.5). An improvement in flow situation could be detected, but this improvement is negligible in terms of efficiency. This improvement is marked in blue circle in Figure 3.6. No separation occurs at the leading edge of the stay vane. The modification could help to avoid damages on the stay vanes (e.g. Figure 3.5 right).

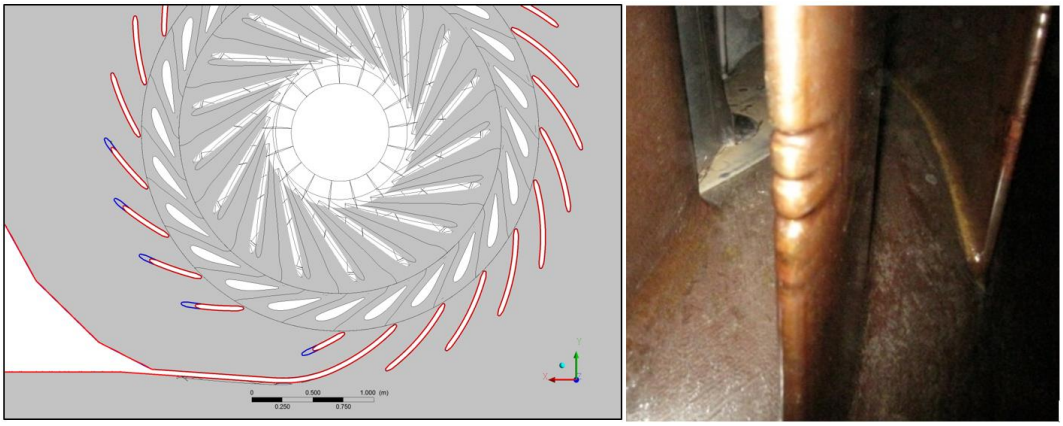

Figure 3.5: Left – stay vane modification, right – damaged stay vane

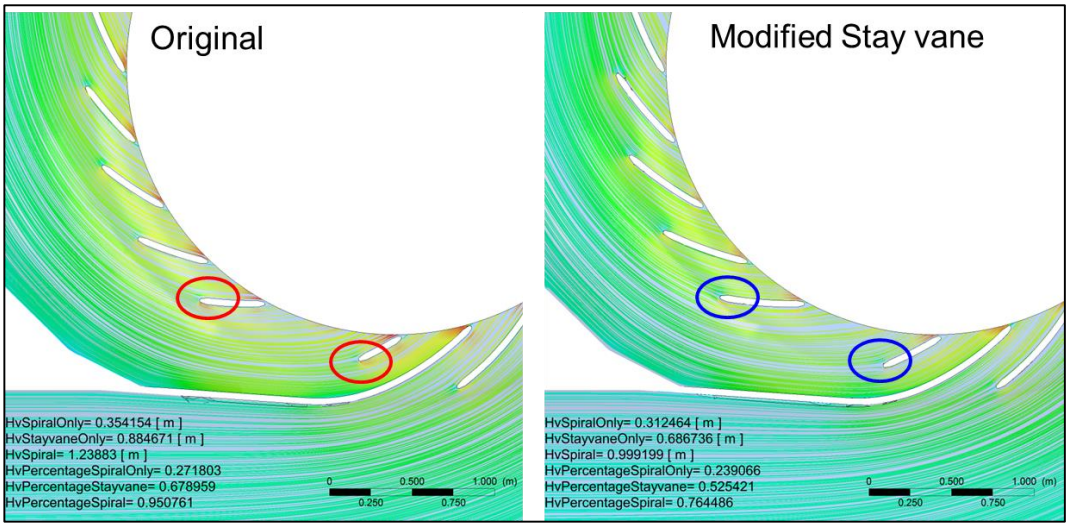

Figure 3.6 : Stay vane modification, streamlines, left – original and right – modified stay vane, optimum point GV 17.5

3.3 Runner

To start with the geometry modifications of the runner, the existing geometry need to be imported into the ANSYS Bladegen, but there is no option in Bladegen to directly import this geometry; program is coded for blade generation from scratch. To import the geometry, couple of files needs to be generated in Bladegen output format. These files are basically txt files, only the txt extension is changed. These steps are explained in reconstruction chapter.

3.3.1 Reconstruction

In BladeGen it is possible to define a meridional section of a runner. On a user-defined number of layers, geometry data of runner profiles can be imported. First of all mean camber line should be defined. This is done by the definition of a curve where the wrap angle „Theta“ is plotted against the meridional length „M“.

Theta-M data file is for Theta angle distribution over meridional view. It contains the theta angle distribution for every cross section curve to define the whole runner blade. These curves are shown in Figure 2.4. Extension of this file should be “.ha”.

Number of cross section curves defines the resolution of the blade geometry. As the number of curves increases, the reconstructed blade geometry gets closer to the actual blade geometry. In Figure 3.7, difference between 4 and 20 cross section lines are shown in meridional view.

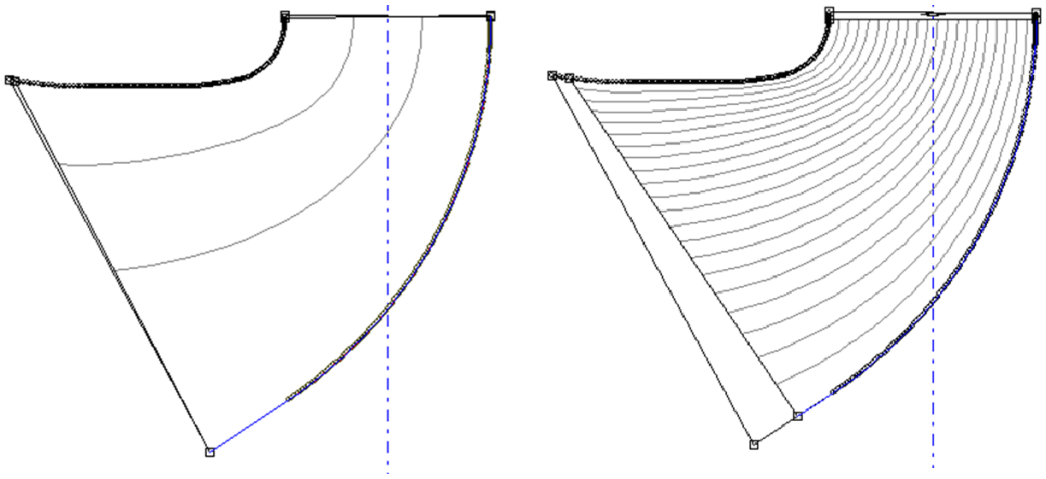

Figure 3.7 : Blade definition in Bladegen with 4 (left) and 20 (right) cross section curves.

For each defined cross section curve thickness data should be loaded. This is done by the definition of a curve where the absolute profile thickness plotted against the meridional length „M“ as alternative NACA-profile data can also be loaded.

Thickness-M data file contains the thickness values over the cross section curves. Extension of this file should be “.ht”.

Third file is z-R data file. It contains the shape of leading and trailing edges of the runner in cylindrical coordinates. Extension of this file should be “.zr”.

Fourth file is also z-R data file but this is for the hub and shroud curves. Extension of this file should also be “.zr”.

File importing starts with the hub and shroud contours and the main meridional view can be obtained. Then the blade leading and trailing edges should be loaded. After selecting the number of cross section curves, theta and thickness distributions should be loaded for each cross section curve.

After these steps, Bladegen gives the 3D model of the runner. This geometry can be exported to Turbogrid for meshing. To change the blade geometry to improve its performance, Bladegen allows the user to manipulate the blade profiles, theta angle distributions and thickness distributions for each cross section curve. In this study

23 different versions are prepared by this modifications and progressive improvement is achieved.

3.3.2 Introduction to the X-Blade-Design

To achieve both of these targets, the idea of the so called X-Blade-Design has to be introduced, which was originally developed and patented (US 4479757) by GE Hydro at the beginning of 1982. Later on in 1998, during the development of the Three Gorges Project in China, the technology has been improved to what is now called X-Blade-Technology [25].

Conventional Francis runner designs are susceptible to cavitation damage on the suction side of the blade, particularly at the leading edge. Such cavitation has been known to cause severe damage to the blade, requiring field repair and in some cases blade modifications which are costly and often difficult to perform [25].

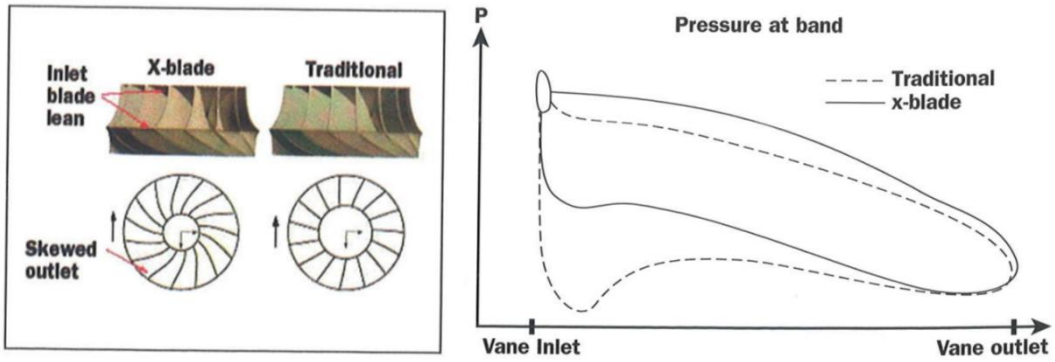

Figure 3.8 : Comparison of a conventional Francis runner with the X-Blade-Design [25], left: 3D design, right: blade loading

In contrast to the conventional Francis runner design, the X-Blade-Design comprises a reversed leading edge and a skewed trailing edge. Figure 3.8 compares the design with a conventional Francis runner, showing the inlet blade lean and the

skewed outlet which are typical identification marks of the X-Blade design. The application of this design philosophy allows for a well-balanced flow field in the passage ways of the runner. Consequently, it results in a more homogeneous pressure distribution on the blade – see blade loading comparison in Figure 3.8.

Due to the experience gained during the last decade of operation, the improved runner design provides superior peak efficiency, better cavitation performance and a wider range of stable operation [26].

3.3.3 Overview of optimization versions

There are two main targets for the optimization of the runner blade: higher turbine efficiency over the whole range of operation and an improved cavitation performance in order to enable secure operation up to a flow rate of $Q = 52$ m³/s.

The main modifications of the original runner blade were carried out for the β-angle distribution, for the location and shape of the trailing edge in the meridional section, and for the initial wrap angle θ at the inlet of the runner, which basically defines the X-Blade shape.

Based on space requirements of the existing turbine the shroud curve of the runner cannot be changed at all. Any potential change would be connected with excessive restructuring works. The hub curve was only slightly changed for some optimization versions to check the impact on the span wise c_m-distribution.

A general overview of all optimization versions is given in Table 3-1 and Table 3-2 where all modifications, the target of the modifications as well as the impact of every modification are documented.

A discussion of the changes and the resulting impact on efficiency, sigma value and blade loading are only carried out for the most important and effective optimization versions. All optimization versions are analyzed by CFD using simple simulation model. For the most successful versions, full model simulations are also carried out.

Table 3-1 : Runner optimization 1/2

Version:	Changed features:	Optimisation targets:	Eta_{max} [%]	$Q_{eta\text{-}max}$ [m^3/s]	$Q_{sigma\text{-}limit}$ [m^3/s]
V00:	Reconstruction of the orginal runner Kadincik2; difference to orginal blade: smoother surface, inaccurate interpretation of angle distrubution (because the shape of the spanwise definition curves in the meridional section can not be changed).		95.2	37	40
V01:	Increased Beta-angle at inlet (especially close to shroud) by ~ 15°; smoothing of " Beta vs. M" - distribution.	Only weak impact on blade loading → X-Blade-Design is necessary.	95.2	37	51
V02:	Based on V01: X-Blade-design; difference between "Theta-Beginning" at hub and shroud accounts for ~3°.	Significantly improved blade loading and higher peak efficiency.	95.8	43.5	52
V03:	Based on V02: Increased of Beta-angle at inlet close to shroud again; smoother slope of Beta-curves at first %30 of blade length.	Blade loading only slightly improved; improvement of part load efficiency	95.9	43.5	52.2
V04:	Based on V03: Reduction of Beta-outlet close to shroud.	cm/cu distribution was significantly improved; best efficiency point shifted to lower flow rate; cavitation performance gets slightly worse.	95.9	37	51.5
V05:	Based on V04: Enlargement of the hub contour in the meridional section.	Hardly any impact on cm and cu	95.9	37	51.5
V06:	Based on V05: Changed thickness distribution to orginal 4-digit-NACA-profiles (with same absolute thickness as orginal blade)	Efficiency curve dropped by ~0.3 percentage points but improved cavitation performance	95.6	40.4	53.5
V07:	Based on V05: Shortening of absolute profile length close to hub and extension of the profile length at mid of blade by changing the shape of the trailing edge in the meridioal section.	Efficiency at best effiency point decreased by ~0.4 percentage points, hardly any influence on c_m/c_u	95.5	37	52
V08:	Based on V05: Smoother, more linear Beta-distribution at shroud and blade inlet.	Improved blade loading at shroud	95.7	37	50.3
V09:	Based on V05: Stronger pronounced X-Blade-design.	Improved blade loading at shroud	96	37	48.5
V10:	Based on V05: Shortening of all profiles by displacement of trailing edge in meridional section.	Higher maximum efficiency at higher flow rate due to reduced blade friction	96	39	49.7
V11:	Based on V09: Repeating the step done with V08 stronger based on V09 (linearisation of Beta similar to another nq50-project (Zekere)).	Improved blade loading	96	37	52
V12:	Based on V09: Combinaton of optimisation steps done for V09 and V10 (stronger X-Blade-Design & shorter profiles in meridional section).	Does the combination of V09 and V10 match for a further improvement	96	40	46.6
V12*:	Based on V12: Modified hub contour in order to combine it with the draft tube version WITHOUT standpipe.	Checking the influence of standpipe on the velocity distribution and on the efficienc level.	96.3	43	48.3
V13:	Based on V11: Increased blade angle at outlet close to hub (to increase cm und to reach cu close to Zero).	More homogeneous cm-/cu-distribution and efficiency curve shifted to higher flow rate.	95.4	37	50.5

Table 3-2 : Runner optimization 2/2

Version:	Changed features:	Optimisation Targets:	Optimization Results:	Eta_{max} [%]	$Q_{eta-max}$ [m^3/s]	$Q_{sigma-limit}$ [m3/s]
V14*:	see	Increased cm close to hub (see target V05)	cm only slightly more homogeneous; eta-curve shifted to higher flow rate by only ~0.1 m^3/s; cavitation performance improved without standpipe.	96.3	43.5	49.3
V15:	Based on V09: Stronger X-Blade design between 50% and 85% span (use of original hub contour).	Improvement of blade loading especially at leading edge.	Efficiency level similar to V09; blade loading and cavitation performance slightly improved; so far best compromise between acceptable efficinecy and acceptable cavitation performance;	95.9	37	49.7
V16:	Based on V09: Linerisation of Beta-curves at outlet close to shroud (use of orginal hub contour)	Improvement of Sigma-curves; additionally,TE appears less skewed viewed from the draft tube.	Better Sigma-values but lower efficiency and stronger overload declie (similar to V11).	95.3	35	53.5
V17:	Based on V09:Displacement of trailing edge close to shroud towards outlet (use of orginal hub contour)	Longer blade close to shroud should result in lower minimal pressure and thus in an improved cavitation performance.	Efficiency level similar to V09; cavitation performance significantly improved but also strong efficiency decrease at overload.	95.8	37	52.5
V18:	Based on V15: Application of the same measures as for V17 (with orginal hub contour)	Acceptable efficiency level (close to V09) and cavitation behaviour similar to V17.	Cavitation performance significantly improved, better efficiency especially at overload strongly reduced.	95.6	37.5	54.3
V19:	Based on V18: Beta-inlet close to shroud increased (in order to reach "Beta-inlet-shroud= Beta-inlet-hub").	Improvement of pressure distrubition especially at shroud.	Cavitation peformance further improved but efficiency further decreased.	95.5	37	56.5
V20:	Based on V15(so far best blade concerning eta and sigma): Slanted trailing edge.	Checking the impact of the trailing edge on eta and sigma.	Efficiency level slightly improved (so far best efficiency in the course of simulatons with standpipe) but cavitation performance significantly decreased.	96.2	38	47.8
V21:	Based on V15(so far best blade concerning eta and sigma): Elliptic trailing edge.	Checking the impact of the trailing edge on eta and sigma.	Cavitation performance improved bu efficiency level slightly decreased.	95.8	39	51.5
V22:	Based on 15: Changed thickness distrubiion to 4-digit-NACA-profiles(same absolute thickness as orginal blade), max. Thickness at 30% camber length.	Checking the impact of the thickness distribution on eta and sigma.	Cavitation performance improved (similar to V06); part load efficiency unchanged, but overload efficiency decreases.	95.8	37	52
V23:	Based on V15: Changed thickness distribution to 4-digit-NACA-profiles (same absolute thickness as original blade), max. Thickness at 15% camber lenght (similar to orginal thickness distribution).	Checking the impact of the thickness distribution on eta and sigma.	Similar efficiency level as V15 with improved cavitation performance.	95.9	37	51.8
V23*:	Based on V23: Simulation with the draft tube version WITHOUT standpipe.	Checking the influence of the standpipe on velocity distribution and on the efficiency level.	Efficiency curve shifted to higher flow rate by ~ $5m^3s$; efficiency increased by ~ 0.5 percentage points. Without standpipe: Slightly more homogeneous cu and cm distribution; cavitation performance slightly better without standpipe!	96.4	42	56
V24:	Based on V15: Changed thickness distrubiion to 4-digit-NACA-profiles(same absolute thickness as orginal blade), max. Thickness at 45% camber length.	Checking the impact of the thickness distribution on eta and sigma.	Part load efficiency unchanged, but overload efficiency decreases; cavitation performance slightly worse.	95.5	37	49.5
V25:	Based on V20: Linearisation of Beta close to outlet at span 0.75	Actually, there are the lowest pressure values at span 0.75 - improvement of sigma with a hopefully accetable decrease of efficiency	Slightly reduced efficiency with only slightly improved cavitation performance.	95.9	39	48

An analysis of the table presented above shows that the first optimization versions (V00 to V03) were created with the aim to improve the blade loading and to reach a more balanced flow field, which is clearly demonstrated in Figure 3.9. The achieved change of the blade loading from V00 (original blade) to the optimization version V04 shows a similar trend as already shown in Figure 3.8 in the course of the introduction of the X-Blade-Design. All the modifications were mainly focused on the inlet part of the blade.

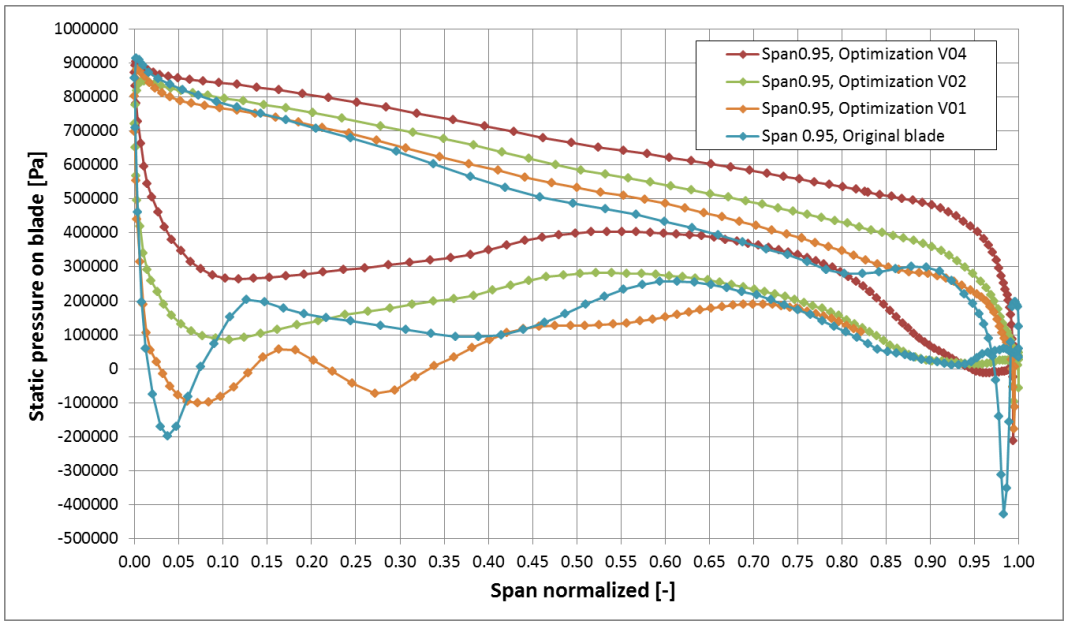

Figure 3.9 : Blade loading comparison of V00, V01, V02 and V04 for the best efficiency point

The next series of runner blade versions (V04 to V08) comprise modifications that were incorporated in order to improve the c_m and c_u-distribution at the outlet of the blade. To reach this target the optimization measures were mainly focused on the outlet part of the blade. With the optimization version V09 an optimized blade

design was found that has an efficiency level as well as a cavitation performance which is much better compared to the original runner blade version. Figure 3.10 shows a comparison of the cm- and cu-distribution of selected blade versions. The presented results demonstrate that the span wise distributions of the meridional velocity component and the swirl component were improved from step to step.

In the course of the next optimization steps (V10 to V19), also the meridional section (especially as far as it concerns the shape of the trailing edge) and the blade angle distribution (comparison of the S-shape with a more linear angle distribution) was changed.

Among all the created optimizations, version V15 stands out particularly sufficient. It seems to be a compromise between acceptable efficiency level and acceptable cavitation performance.

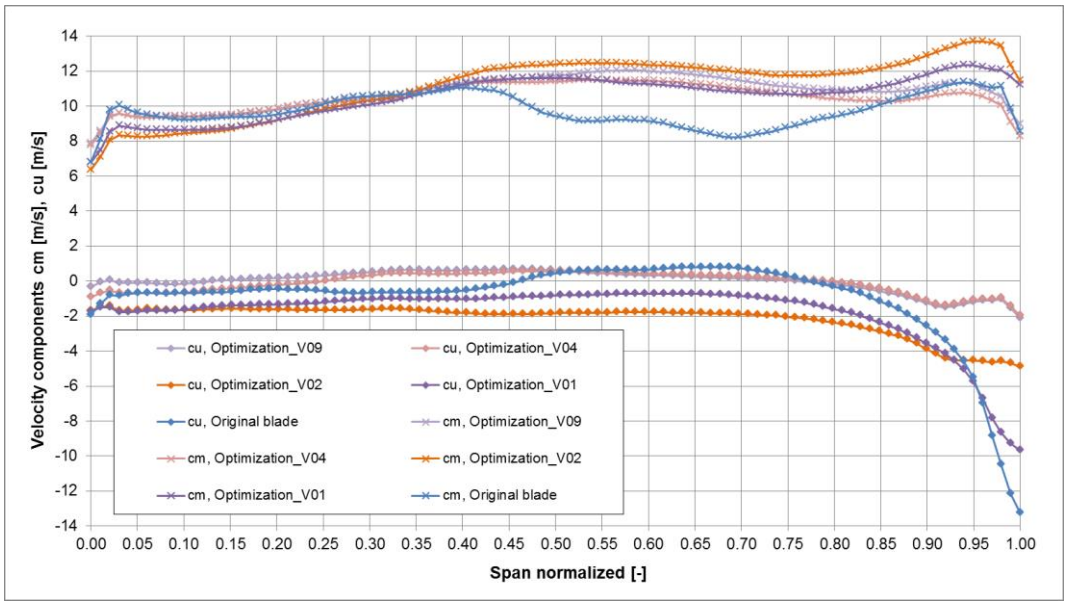

Figure 3.10 : Span wise c_m and c_u-distributions of selected runner blade versions

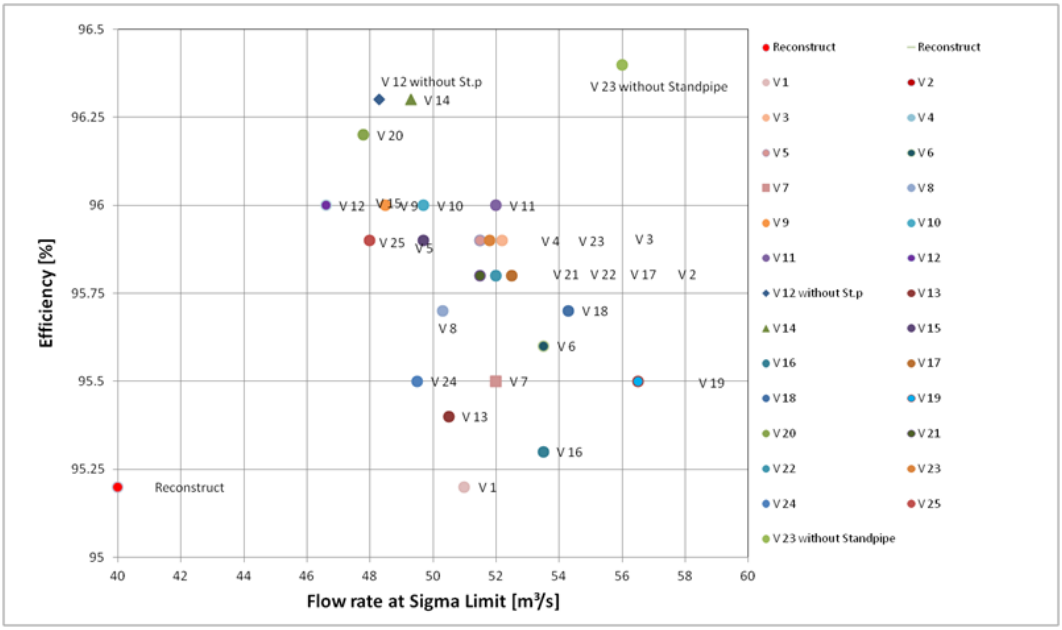

Figure 3.11 : Comparison of the maximum efficiency and the maximum allowable flow rate due to the cavitation limit for all created optimization versions

Based on version V15 a sensitivity analysis concerning the impact of the trailing edge design (see V20 and V21) and the impact of the thickness distribution (V22 to V24) was carried out.

Finally, Figure 3.11 and Figure 3.12 show a comparison of the maximum turbine efficiency, the flow rate at the best efficiency point and the maximum allowable flow rate due to the cavitation limit for all created optimization versions.

It turns out that the optimization version V23* (which is equal to version V23, but without standpipe) reaches the highest efficiency level combined with the best cavitation performance.

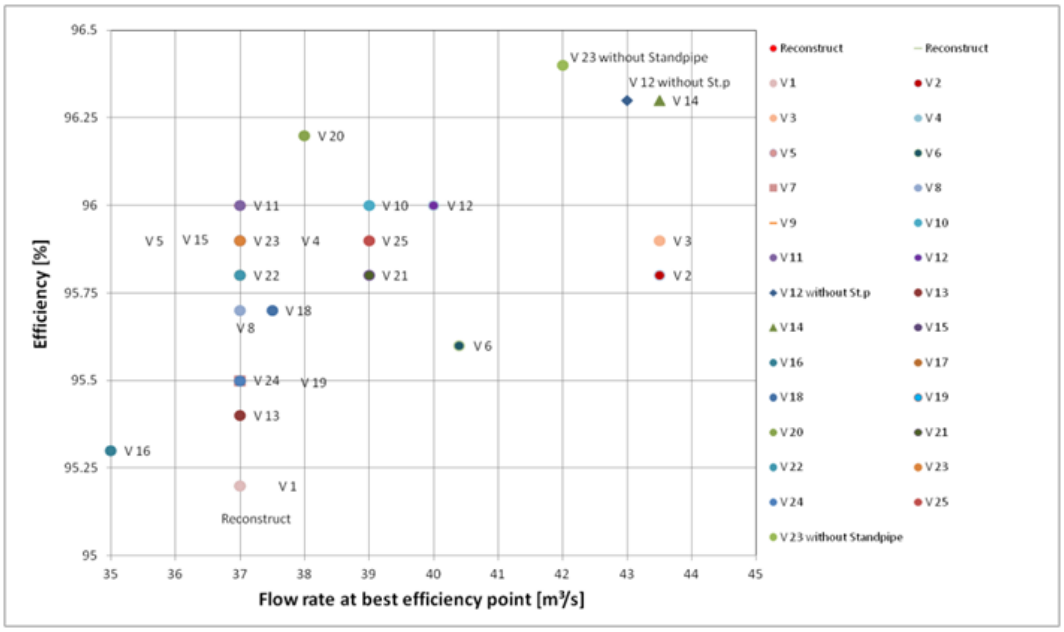

Figure 3.12 : Comparison of the maximum efficiency and the flow rate at the best efficiency point for all created optimization versions

In order to provide an overview of the improvements reached in the course of the optimization process of the runner blade, the following figures were prepared to present a comparison of the basic hydraulic properties of the original runner blade and the final optimization version V23*.

First of all, Figure 3.13 presents the blade loading of the original blade and the version V23* evaluated for 95 percent span at the best efficiency point. The comparison shows that the use of the X-Blade-Design and the implementation of all the other optimization measures led exactly to the changes that were already presented in Figure 3.8.

Furthermore, Figure 3.14 presents the improvements of the span wise distribution of the c_m and c_u-velocity components. Additionally, it turns out that the removal of the standpipe located in the original draft tube results in more balanced velocity distributions. Due to the removal of the standpipe, the mass flow rate and thus the velocity component c_m is increased while it is decreased in the mid of the runner.

Consequently, the increase of the c_m-component close to the hub contour causes a reduction of swirl at the outlet of the runner.

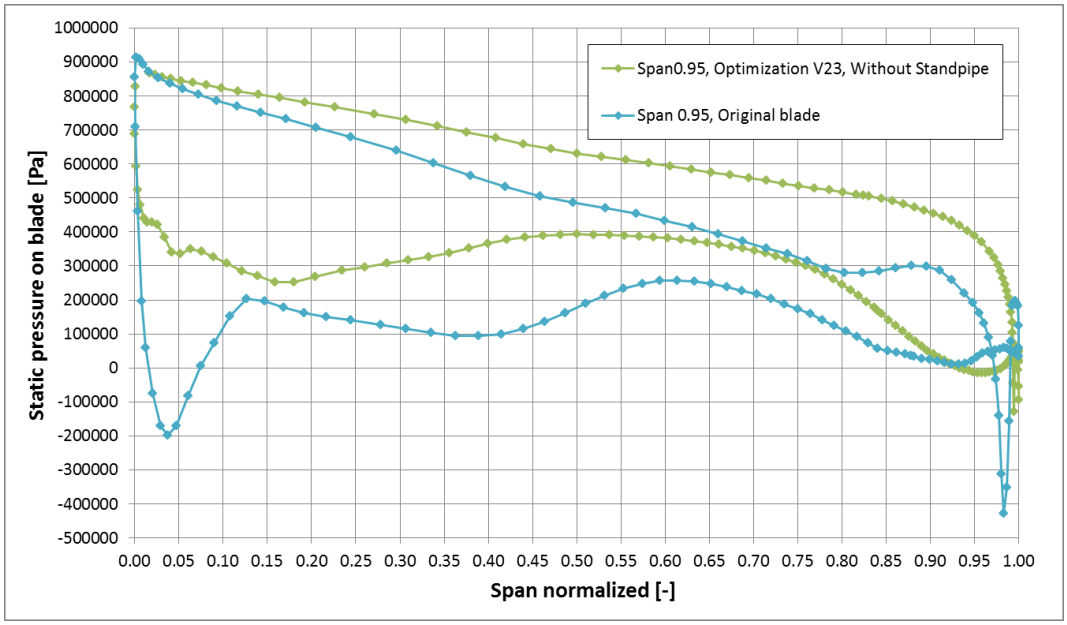

Figure 3.13 : Blade loading comparison of the original runner version and version V23*

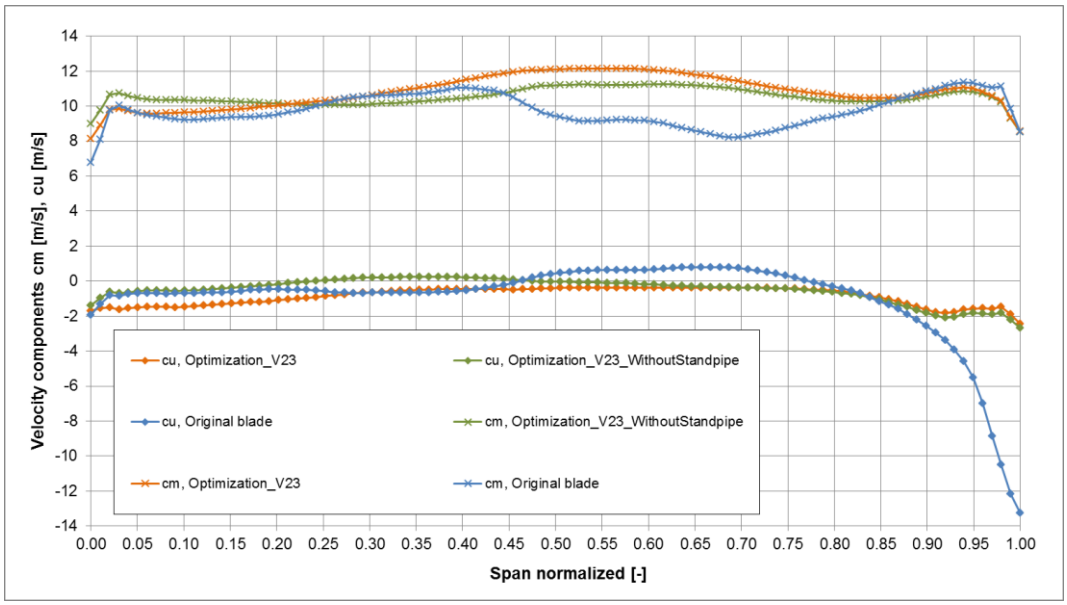

Figure 3.14 : Span wise cm- and cu-distributions for the original blade and the blade versions V23 and V23*

Another improvement achieved in the course of the optimization is the suppression of separation zones in the blade channels that appear close to the shroud contour at the original runner. This is visualized in Figure 3.15, which presents velocity vectors plotted on a turbo surface for 95 percent span. The left picture shows the observed separation zones that were suppressed in the course of the optimizations (see right picture).

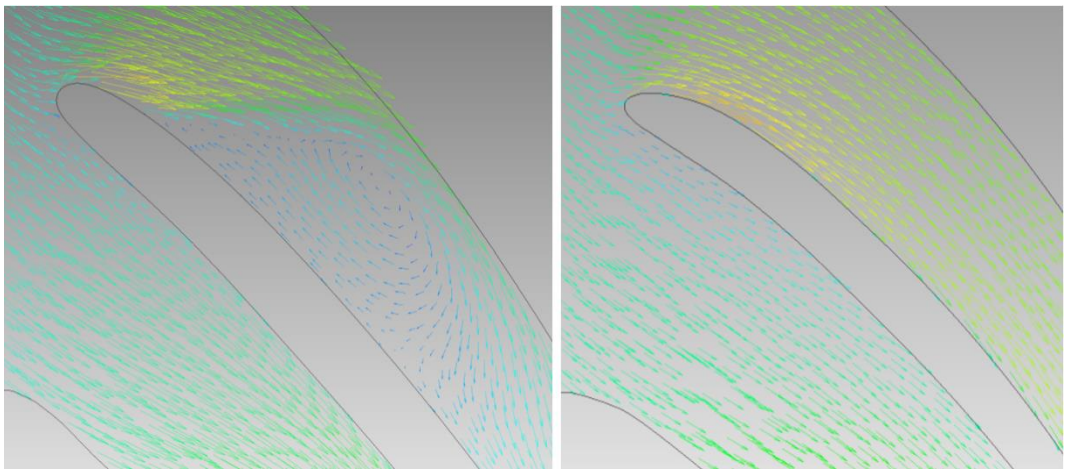

Figure 3.15 : Velocity vectors plotted on a turbo surface for 95 percent span at the best efficiency point of the original runner blade (left picture) and the runner version V23 (right picture)

A final overview of the improvements reached and the geometrical changes implemented in the course of the optimization process is given with the following figures. While Figure 3.16 (original runner) and Figure 3.17 (optimization version V23*) show a 3D view of the runner, Figure 3.18 left (original runner) and Figure 3.18 right (optimization version V23*) present a view onto the runner blades from the draft tube side. The visualizations clearly illustrate that a more homogeneous pressure distribution was reached in the course of the optimization process.

Additionally, it turns out that the changes implemented into the final blade version V23* result in a leading edge and trailing edge design which is well comparable with the identification marks of the X-Blade design already presented in Figure 3.8.

A summary of the efficiency level and cavitation performance reached is given in Figure 3.19 and Figure 3.20. While Figure 3.19 shows the improvements reached as far as it concerns the hydraulic efficiency calculated with the simple CFD model, Figure 3.20 illustrates the achieved improvements of the cavitation performance.

Using the simple CFD model with the optimized runner version V23 and the draft tube version without standpipe finally results in a hydraulic peak efficiency of 96.4% compared to a peak efficiency of 94.25% reached with the original runner. Additionally, it has to be pointed out that the cavitation limit was shifted from Q = 40 m³/s with the original runner to Q = 56 m³/s with the new runner version V23.

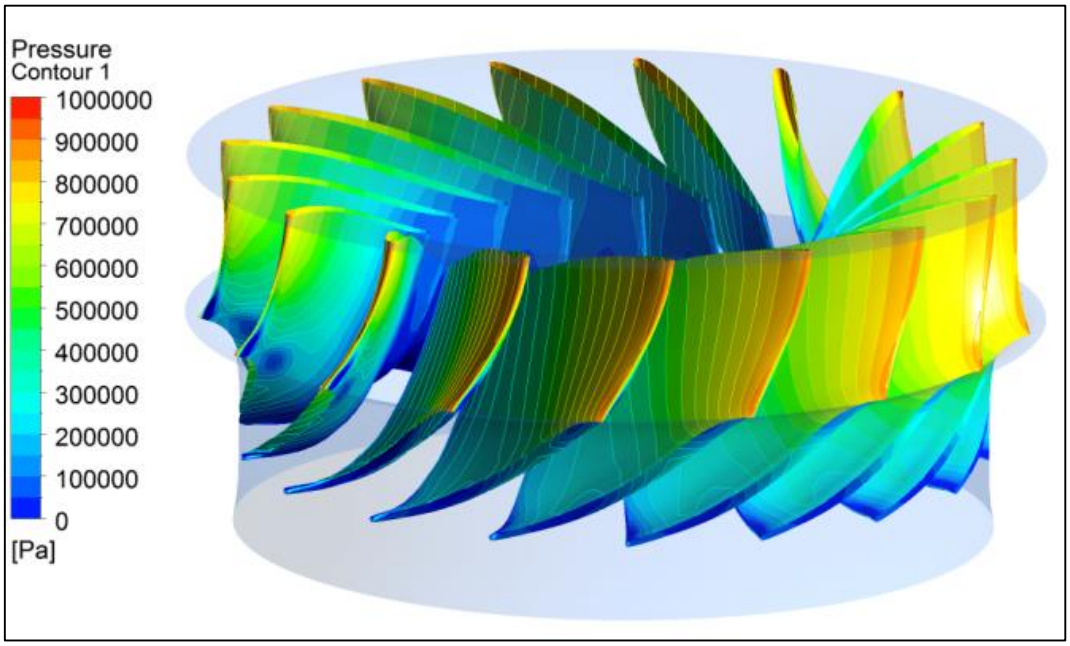

Figure 3.16 : 3D view and pressure distribution of the original runner blade

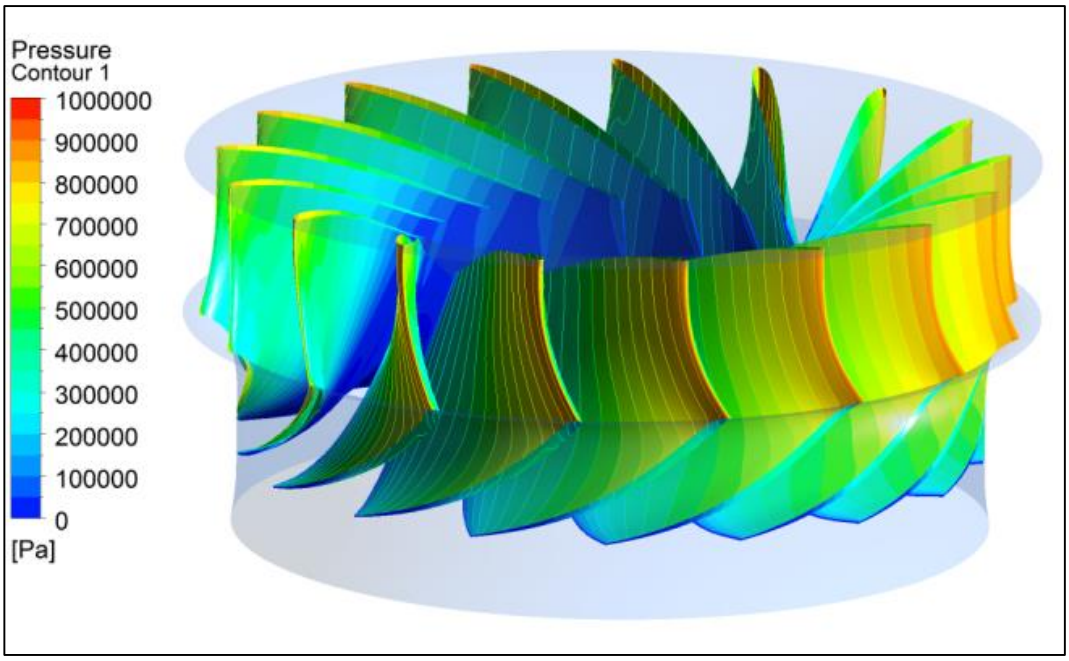

Figure 3.17 : 3D view and pressure distribution of the V23

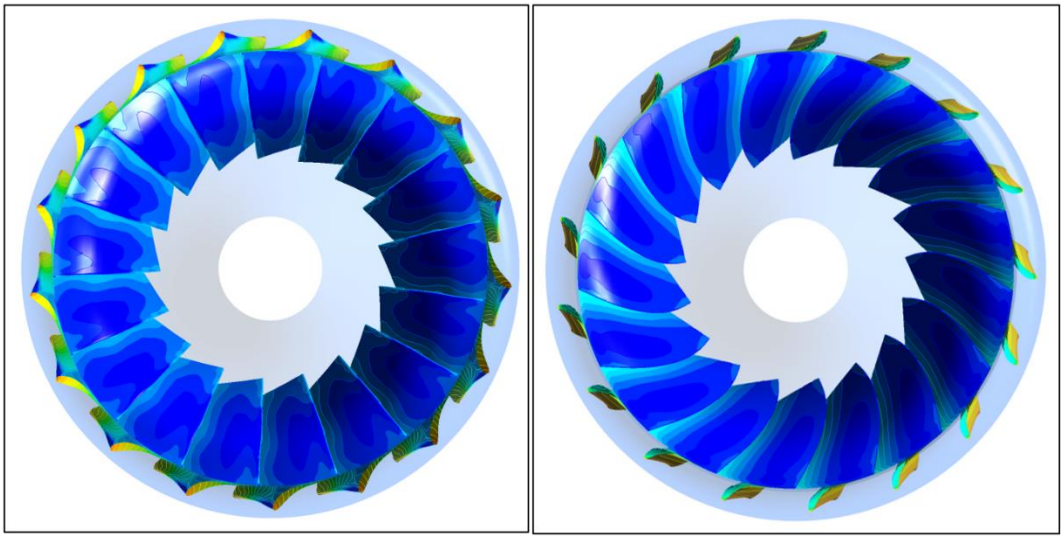

Figure 3.18 : View from downstream (draft tube side) to the original runner blade (left) and of runner V23 (right)

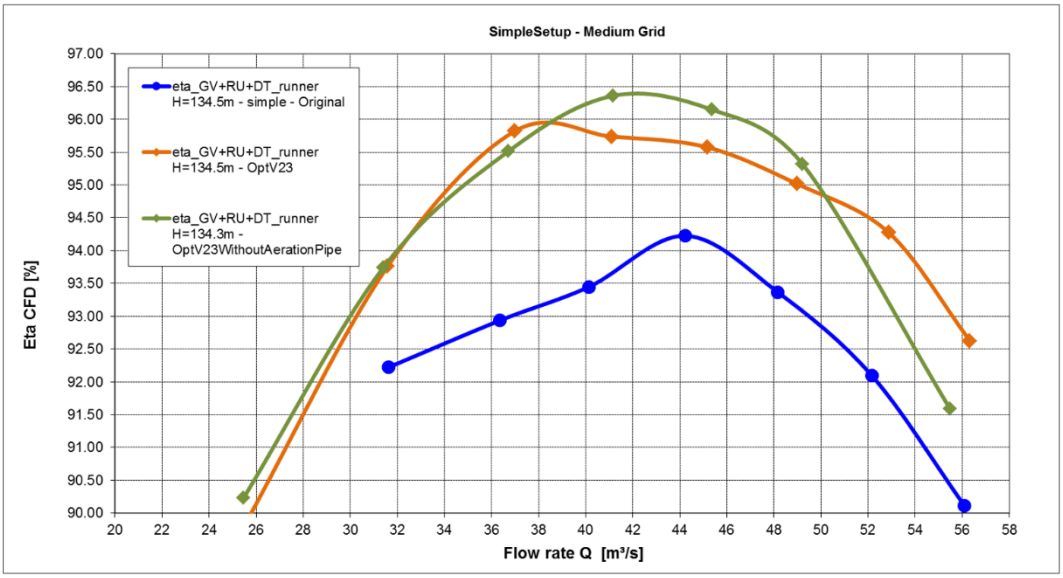

Figure 3.19 : Hydraulic turbine efficiency of the original blade, versions V23 and V23*

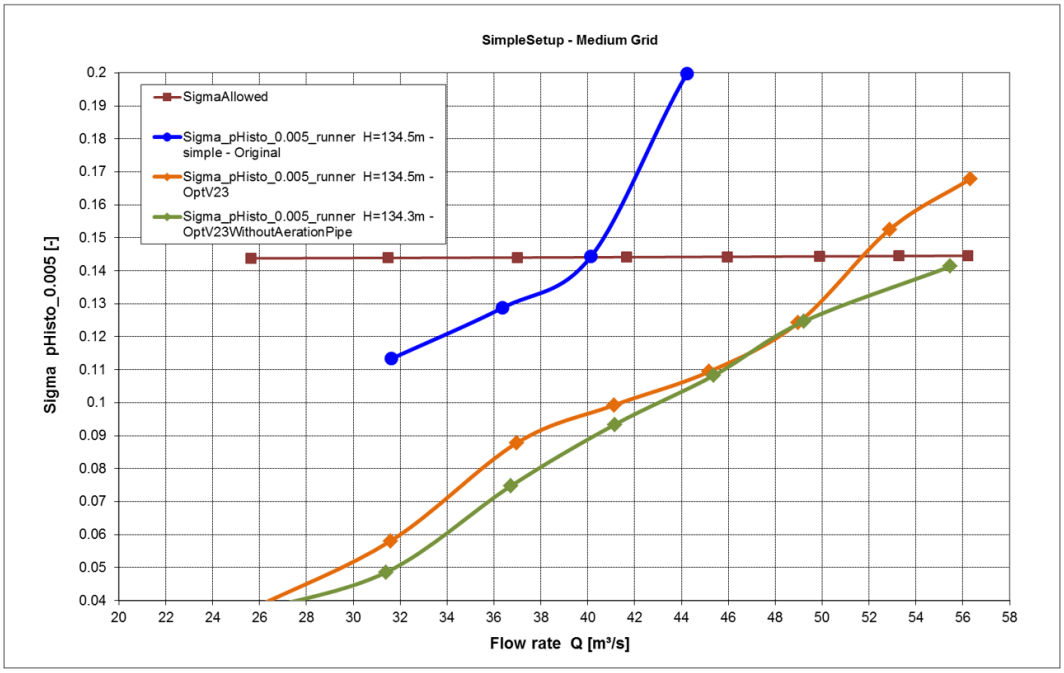

Figure 3.20 : Cavitation performance of the original blade, versions V23 and V23*

3.4 Results of the proposed design

In Figure 3.21, the results of the full model are displayed in comparison to the original design. For the whole operation range up to 52m³/s, the efficiency is improved and also the cavitation performance is on an appropriate level. In Figure 3.22, the cavitation performance is displayed and for the new design the σ_{tubine} -line is up to 53 m³/s below the σ_{plant} value: cavitation free operation up to this flow rate.

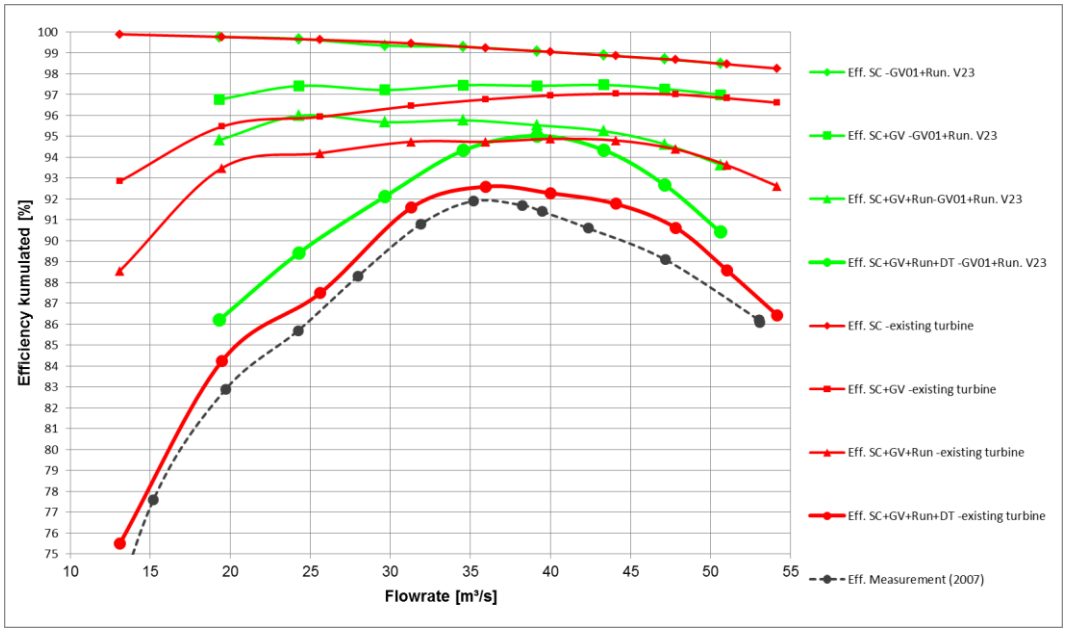

Figure 3.21 : Efficiency splitting for the proposed design V23 without standpipe with guide vane GV Opt V01

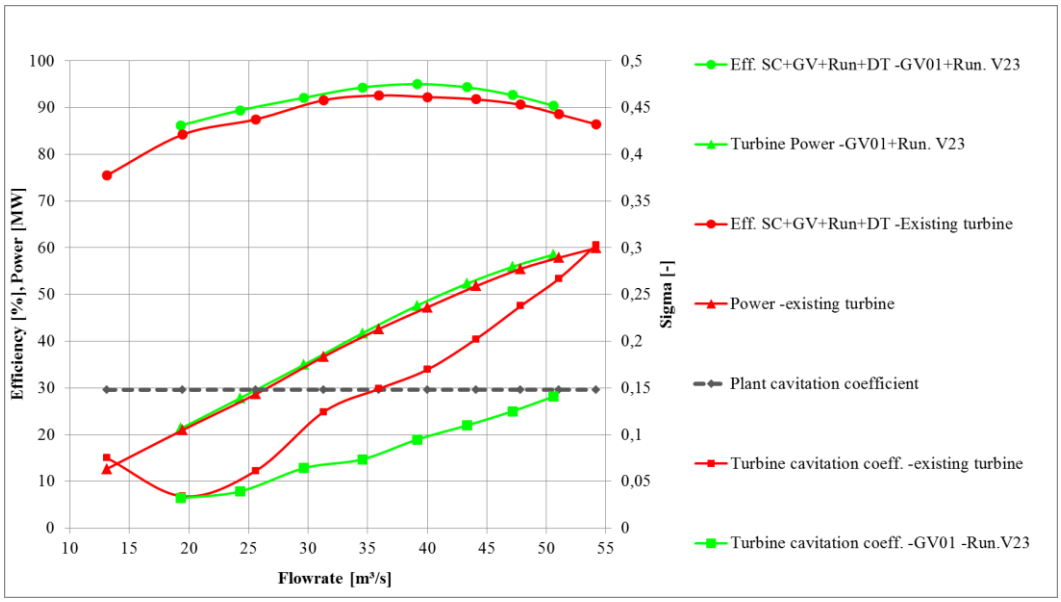

Figure 3.22 : Cavitation performance for the proposed design V23 without standpipe with guide vane GV Opt V01

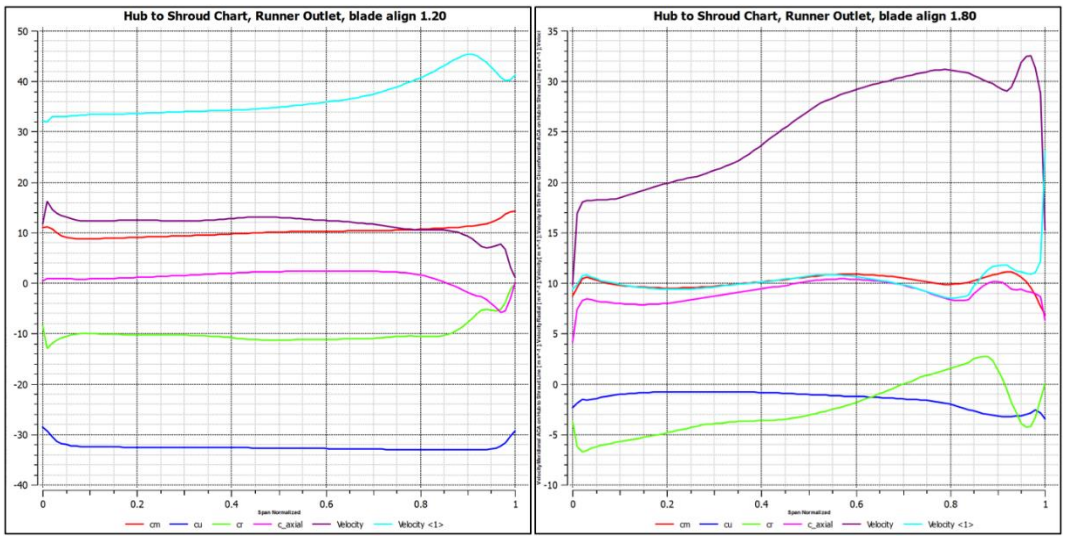

Figure 3.23 : c_m and c_u distributions at upstream (left) and downstream (right) the runner

In Figure 3.23, c_m is shown in red and c_u is shown in blue just before and just after the runner. It can be seen that the c_m-distribution on both locations is relatively constant. Also, the c_u-distribution is very constant, almost the complete the tangential velocity before the runner (rotation anti-clockwise) is converted into torque in the runner.

Finally, different variants were calculated and given in Figure 3.24. Yellow is the same as the final version, but the draft tube is unchanged with the exiting stand pipe. Pink is the final runner version, but with the existing guide vane. The red version stands for the existing hydraulics.

The turbine efficiency hill chart of the final optimization version is shown in Figure 3.25. According to the Francis turbine losses as function of the specific speed, which was already discussed in Chapter 2.5.8, one percentage point was subtracted from the hydraulic efficiency based on CFD in order to obtain the resulting turbine efficiency.

Compared to the original turbine the best efficiency point in the hill chart was shifted from Q = 37 m³/s and H = 124 m to Q = 39.5 m³/s and H = 132m which ideally fits to the operation range of the turbine. The peak efficiency was increased from 92.5 % to 94.2 %. All CFD results achieved in course of the variation of the head level for the optimized version V30 are shown in Table 3-3.

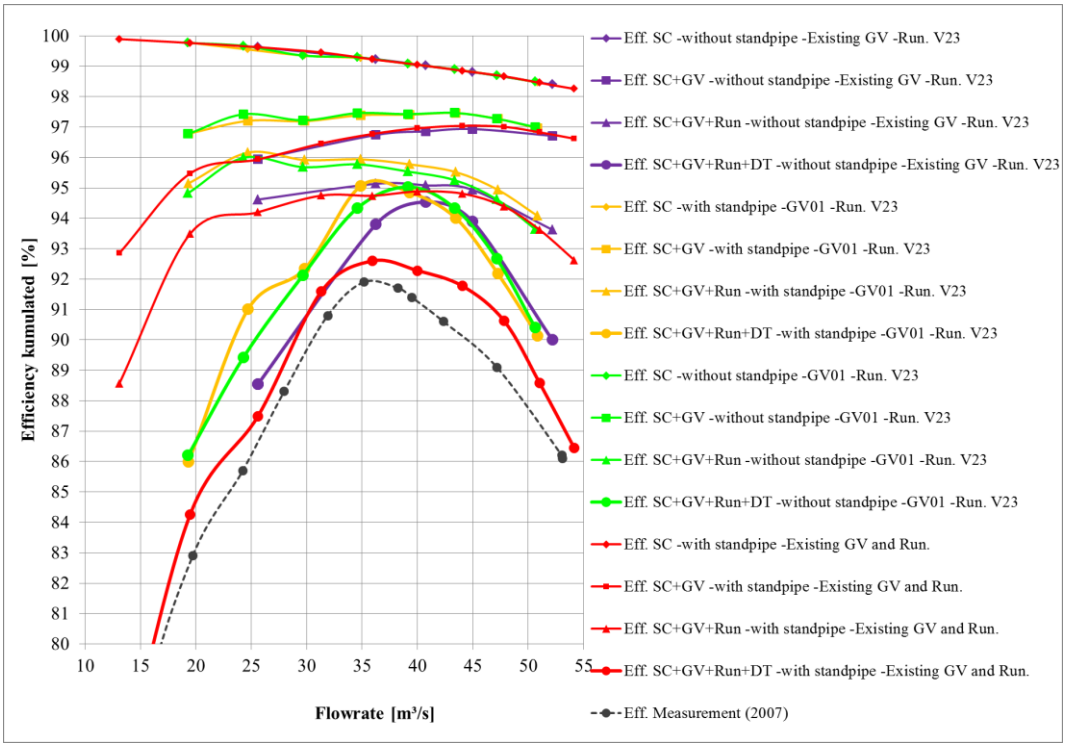

Figure 3.24 : Variants with final version V23

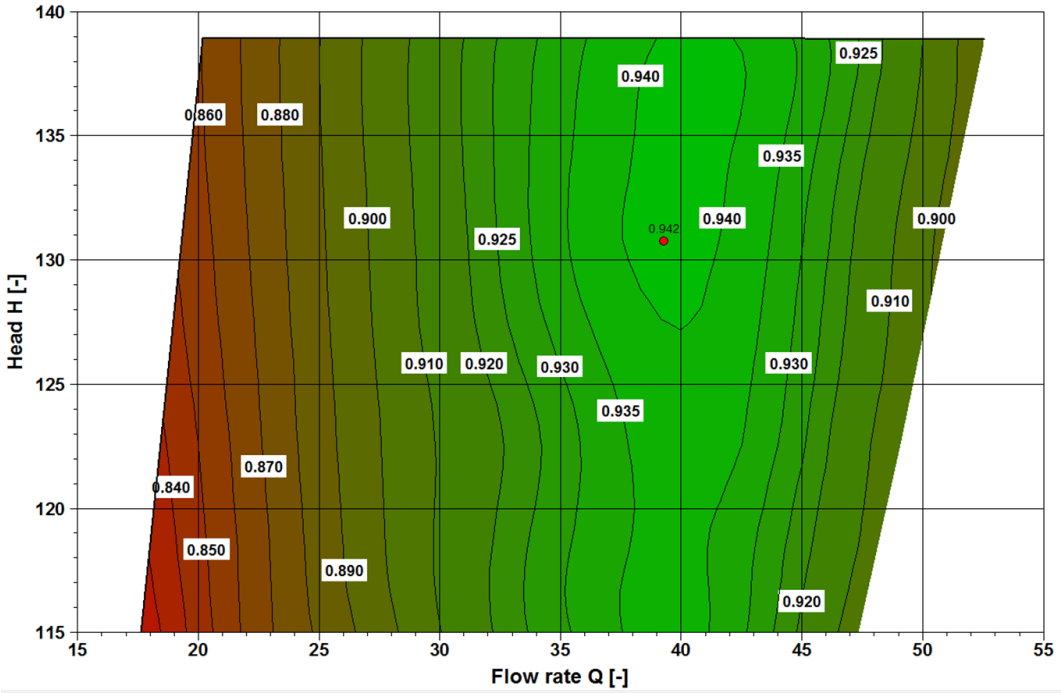

Figure 3.25 : Turbine efficiency hill chart of the final optimization version

Table 3-3 : Hill chart data, optimized version

Q	H	P	eff_{CFD}	PHI	PSI	n_q	Q_{ED}	Q_{11}	n_{ED}	n_{11}	GV-angle	a_0	Servo piston travel
[m³/s]	[m]	[MW]	[%]	[-]	[-]	[rpm]	[-]	[-]	[-]	[-]	[°]	[mm]	[mm]
17.56	114.40	16.34	0.82	0.08	1.37	35.94	0.08	217.97	0.39	394.81	7.5	47.4	141.6
22.15	114.39	21.65	0.86	0.10	1.37	40.36	0.10	244.77	0.39	319.69	10	62.7	169.0
27.10	114.39	27.37	0.89	0.13	1.37	44.65	0.12	270.76	0.39	268.14	12.5	77.7	195.6
31.69	114.39	32.92	0.92	0.15	1.37	48.29	0.14	292.83	0.39	233.46	15	92.4	221.4
36.06	114.39	38.00	0.93	0.17	1.37	51.51	0.16	312.36	0.39	209.62	17.5	106.8	246.5
40.27	114.39	42.68	0.94	0.19	1.37	54.43	0.18	330.06	0.39	192.14	20	121.0	270.9
43.92	114.39	45.95	0.92	0.21	1.37	56.85	0.20	344.73	0.39	181.81	22.5	134.9	294.5
47.18	114.38	48.35	0.91	0.22	1.37	58.92	0.21	357.30	0.39	174.98	25	148.4	317.4
18.45	122.57	18.77	0.84	0.09	1.46	34.98	0.08	212.14	0.37	368.28	7.5	47.4	141.6
23.24	122.57	24.66	0.87	0.11	1.46	39.26	0.10	238.08	0.37	300.17	10	62.7	169.0
28.45	122.56	31.21	0.90	0.13	1.46	43.44	0.12	263.42	0.37	251.55	12.5	77.7	195.6
33.08	122.56	36.97	0.92	0.16	1.46	46.84	0.14	284.09	0.37	221.52	15	92.4	221.4
41.92	122.56	47.62	0.94	0.20	1.46	52.73	0.18	319.78	0.37	183.22	20	121.0	270.9
45.68	122.56	51.11	0.92	0.22	1.46	55.05	0.20	333.83	0.37	173.74	22.5	134.9	294.5
49.07	122.55	53.75	0.90	0.23	1.46	57.06	0.21	346.01	0.37	167.31	25	148.4	317.4
19.33	130.74	21.32	0.85	0.09	1.56	34.11	0.08	206.87	0.36	345.79	7.5	47.4	141.6
24.35	130.74	27.88	0.88	0.11	1.56	38.29	0.10	232.20	0.36	282.73	10	62.7	169.0
29.77	130.73	35.20	0.91	0.14	1.56	42.34	0.12	256.74	0.36	237.38	12.5	77.7	195.6
34.65	130.73	41.83	0.93	0.16	1.56	45.68	0.15	277.01	0.36	208.54	15	92.4	221.4
39.31	130.73	47.88	0.94	0.19	1.56	48.65	0.16	295.03	0.36	188.45	17.5	106.8	246.5
43.54	130.73	52.70	0.94	0.21	1.56	51.20	0.18	310.52	0.36	175.37	20	121.0	270.9
47.35	130.73	56.29	0.92	0.22	1.56	53.40	0.20	323.83	0.36	166.90	22.5	134.9	294.5
50.83	130.72	59.04	0.90	0.24	1.56	55.32	0.21	335.51	0.36	161.05	25	148.4	317.4
20.20	138.91	23.92	0.86	0.10	1.66	33.33	0.08	202.11	0.35	326.94	7.5	47.4	141.6
25.45	138.91	31.23	0.89	0.12	1.66	37.40	0.10	226.82	0.35	267.65	10	62.7	169.0
31.05	138.91	39.29	0.92	0.15	1.66	41.32	0.13	250.56	0.35	225.30	12.5	77.7	195.6
36.04	138.90	46.32	0.94	0.17	1.66	44.51	0.15	269.94	0.35	199.15	15	92.4	221.4
40.81	138.90	52.79	0.94	0.19	1.66	47.37	0.17	287.25	0.35	180.52	17.5	106.8	246.5
45.15	138.90	57.95	0.93	0.21	1.66	49.82	0.18	302.13	0.35	168.35	20	121.0	270.9
49.05	138.90	61.79	0.92	0.23	1.66	51.93	0.20	314.93	0.35	160.42	22.5	134.9	294.5
52.55	138.89	64.50	0.89	0.25	1.66	53.75	0.21	325.99	0.35	155.35	25	148.4	317.4

3.5 Influence on Energy Production

At the end of the optimization study, an energy production calculation is carried out. Improvement on the energy production depends on the parts that will be rehabilitated due to the economic aspects. Two different alternative scenarios are presented. Scenario 1 includes both runner and guide vanes rehabilitation and scenario 2 includes only the runner rehabilitation.

3.5.1 Scenario 1

Original runner is replaced by runner optimization V23, original guide vanes are replaced by optimization V01 and standpipe is also removed since the new runner and guide vanes will generate better draft tube performance and draft tube oscillations will be weaker.

In Figure 3.26, efficiency comparison of the Scenario 1 and the existing turbine is given. Best-fit curves are generated for both efficiency curves and polynomial functions are used for energy production calculations. Curves are also extrapolated on both sides to be able to make calculations where there is no CFD calculation available. In Table 3-4, efficiency curve is divided into 5 MW power intervals and overall energy production is calculated based on the previous 5 year's daily production values. Total average yearly energy production is increased from 179.76 GWh to 184.85 GWh.

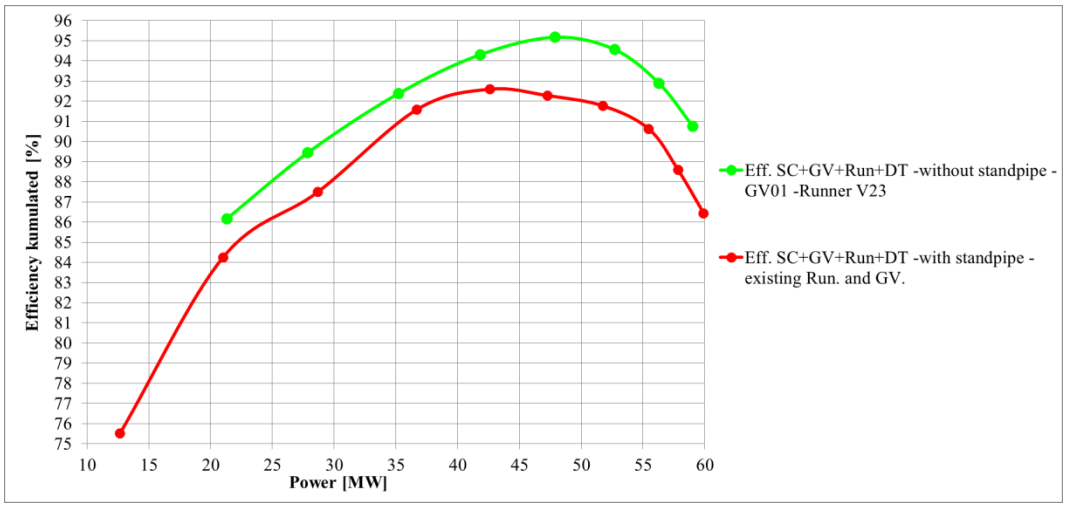

Figure 3.26 : Efficiency comparison of Scenario 1 against existing turbine

Table 3-4 : Averaged efficiency values for 5 MW power segments and overall production calculation

	5 - 10 MW	10 - 15 MW	15 - 20 MW	20 - 25 MW	25 - 30 MW	30 - 35 MW	35 - 40 MW	40 - 45 MW	45 - 50 MW	50 - 55 MW	55 - 60 MW	Sum	
Eff-ratio	1,0917	1,0554	1,0349	1,0236	1,0185	1,0176	1,0193	1,0224	1,0257	1,0282	1,0286		
Existing	0,81	17,80	24,40	22,53	17,26	14,97	11,10	18,46	21,71	22,85	7,89	179,76	GWh
Runner+Guidevane new	0,88	18,78	25,25	23,06	17,58	15,23	11,31	18,87	22,27	23,49	8,12	184,85	GWh
											delta	5,1	GWh

3.5.2 Scenario 2

In scenario 2, original runner is replaced with runner v23 but, guide vanes remained unchanged due to high cost of manufacturing. Standpipe is removed. Total increment in energy production is calculated as 2.34 GWh for one year operation.

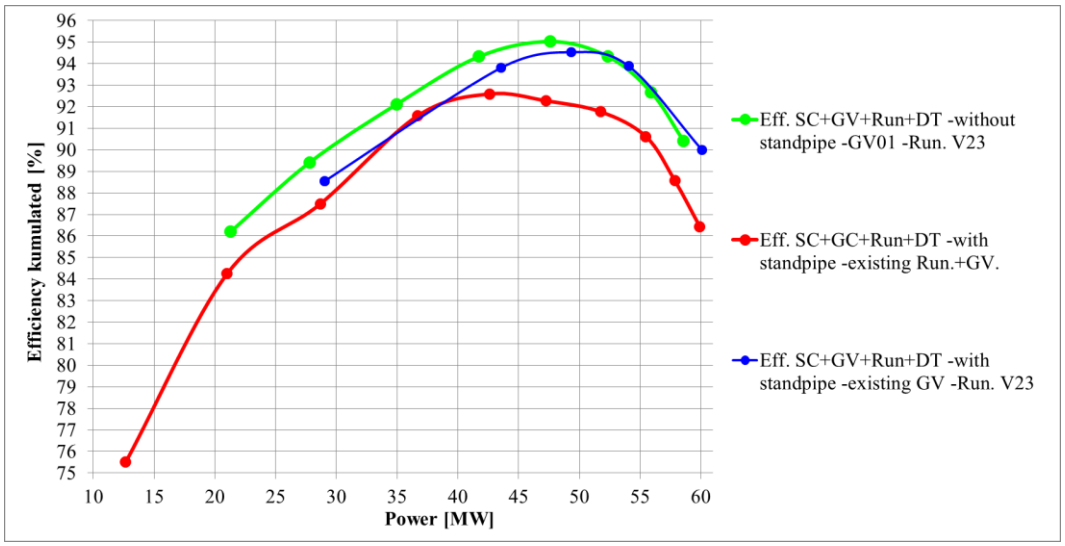

Figure 3.27 : Efficiency comparison of Scenario 2 against existing turbine

Table 3-5 : Averaged efficiency values for 5 MW power segments and overall production calculation

	5 - 10 MW	10 - 15 MW	15 - 20 MW	20 - 25 MW	25 - 30 MW	30 - 35 MW	35 - 40 MW	40 - 45 MW	45 - 50 MW	50 - 55 MW	55 - 60 MW	Sum	
Eff-ratio	1,0917	1,0554	1,0349	1,0236	1,0185	1,0176	1,0193	1,0224	1,0257	1,0282	1,0286		
Existing	0,81	17,80	24,40	22,53	17,26	14,97	11,10	18,46	21,71	22,85	7,89	179,76	GWh
Runner Only	0,50	17,35	25,00	22,76	17,30	15,06	11,24	18,75	22,17	23,67	8,30	182,10	GWh
											delta	2,34	GWh

CHAPTER 4

CONCLUSION

In this study, the turbine of an existing hydropower plant is analyzed. Performance of the existing turbine is evaluated using CFD analysis and an improved new design is proposed with detailed explanations.

In the course of the on-site inspection large cracks around the leading edge of the runner are detected. In the regions, where these cracks were found on the original runner, also zones critical to cavitation were found based on the CFD-simulations. It is likely that these cracks will propagate with ongoing operation time. Thus, the runner has to be changed in the near future in any case.

With the modified stay vane design, no significant improvement could be detected. Only a repair welding and grinding should be done.

For the guide vanes, the symmetrical profile (V01) is considered as the best version. The efficiency improvement reaches 1 % within the flow rate range of less than 35m³/s and is still above the level of the existing one up to a flow rate of 50 m³/s.

The improvements of the runner performance were basically reached by the introduction of an X-Blade design and a smoothed and modified β-angle distribution. An increase of the β-angle at the blade inlet close to shroud led to better inflow conditions. A reduction of the β-angle at the blade outlet close to shroud led to an improved energy conversion of the blade.

Compared to the original turbine, the best efficiency point in the hill chart was shifted from Q = 37 m³/s and H = 124 m to Q = 39.5 m³/s and H = 132m which ideally fits to the operation range of the turbine. The peak efficiency was increased

from 92.5% to 94.2% and cavitation-free operation up to a maximum flow rate of more than 50m³/s.

As a result, a more efficient guide vane and runner is proposed. Since a rehabilitation project is necessary due to the cracks on the runner, a new design with better efficiency and increased overall energy production should be considered for this power plant.

According to the gained experience in this study it is seen that:

- In the mesh independency, since all the efficiency curves have the same maximum point and have the same slope, analysis can be performed only with single discharge value. This will reduce the number of analysis from 40 to 4.
- As explained in the design improvement chapter, modifications that have no significant effect on the efficiency and cavitation performance are detected. Next projects can be done with less runner versions and significant amount of time could be saved.
- Detailed spiral case post processing shown that only the geometrical area distribution of the spiral case sections and the stay vane outlet flow angles shows the necessary information about spiral case performance.

Future Work

A finite element analysis regarding mechanical stresses has to be carried out by an expert.

A model test has to be carried out in order to prove the proposed hydraulic shape. This witness test should be realized according to the IEC 60193 requirements.

REFERENCES

[1] De Leva F. De Servio F., Modern design trends in selecting and designing Francis turbines, Water and Dams Construction (August 1976), 28–35.

[2] Quantz L., Motores hidraulicos, Ed. Gustavo Gil, C/ Enrique Granados,45, 1960.

[3] Vivier L., Turbines hydrauliques et leur regulation, Ed. Albin Michel, Rue. Huygens, Paris, 1966.

[4] Henry P., Calcul et trace de l'aubage de la turbine Francis, IMHEF-LMH EPFL, Av. de Cour 33b, Lausanne Switzerland, 1995.

[5] Bovet Th., Contribution to the study of Francis-turbine runner design, ASME (1962).

[6] Suzuki T. Enomoto Y., Kurosawa S., Design optimization of a Francis turbine runner using multi-objective genetic algorithm, Proceedings of the XXIInd IAHR Symposium on Hydraulic Turbomachinery and Systems, vol. 1, 2004.

[7] Avellan F. Pedretti C. Tomas L. Ferrando L., Kueny JL., Surface parametrization of a Francis runner turbine for optimum design, Proceedings of the XXIInd IAHR Symposium on Hydraulic Turbomachinery and Systems, 2004.

[8] Helali A. Demeulenaere A. Hirsch C. Kueny JL., Lestriez R., Optimal design of a small hydraulic turbine, Proceedings of the XXIInd IAHR Symposium on Hydraulic Turbomachinery and Systems, 2004.

[9] Casey M. Sallaberger M., Eisele K., Accelerated design procedure for Francis runners in rehabilitiation process, Hydropower Dams (2001), 87–92.

[10] Thum S. Schilling R., Design optimization of hydraulic turbomachinery bladinds by multilevel CFD-technique, Proceedings of the XXIst IAHR Symposium on Hydraulic Turbomachinery and Systems (IAHR, ed.), vol. I, IAHR, September 2002, pp. 19–28.

[11] Pedretti C. Tomas L., Automated design of a Francis turbine runner using global optimization algorithms, Proceedings of the XXIst IAHR Symposium on Hydraulic Turbomachinery and Systems (IAHR, ed.), vol. I, IAHR, September 2002, pp. 11–18.

[12] Kaygusuz, K., Sari, A. (2003). Renewable energy potential and utilization in Turkey. Energy Conversion and Management, 44 (3), pp.459-478.

[13] Giesecke, J., Mosonyi, E., Wasserkraftanlagen. Planung, Bau und Betrieb (4th ed.) Berlin: Springer, 2005.

[14] R.T. Knapp, J.W. Daily, F.G. Hammit, Cavitation, McGraw-Hill, New York, 1970.

[15] F. Avellan, M. Farhat, Shock pressure generated by cavitation vortex collapse, Proceedings of the Third International Symposium on Cavitation Noise and Erosion in Fluid Systems, FED-vol. 88, ASME Winter Annual Meeting, San Francisco, CA, 1989, pp. 119–125.

[16] S.C. Li (Ed.), Cavitation of Hydraulic Machinery, vol. 1, Imperial College Press, London, 2000.

[17] J.P. Franc, F. Avellan, B. Belahadji, J.Y. Billard, L. Brianc-on-Marjollet, D. Fre´chou, D.H. Fruman, A. Karimi, J.L. Kueny, J.M. Michel, La Cavitation.

Me´canismes Physiques et Aspects Industriels, Presses Universitaires de Grenoble, 1995.

[18] B. Grindoz, Lois de Similitudes dans les Essays de Cavitation des Turbines Francis, Ph.D. Thesis 714, EPFL, Lausanne, 1991.

[19] HYPERBOLE, https://hyperbole.epfl.ch/SitePages/Home.aspx, Publication Date : 01/12/2013. (accessed 15/08/2016)

[20] Jacob, T., Prenat, J. E.; "Generation of hydro-acoustic disturbances by a Francis turbine model and dynamic behavior analysis", Proceedings of IAHR 15th Symposium on Modern Technology in Hydraulic Energy Production, Vol. 2, paper T4, Belgrade, Yugoslavia, 11-14 September 1990.

[21] FARHAT M., NATAL S., AVELLAN F., PAQUET F., LOWYS P.Y., COUSTON M.; Onboard Measurements of Pressure and Strain Fluctuations in a Model of Low Head Francis Turbine. Part 1: Instrumentation, Proc. of the XXIst IAHR Symposium on Hydraulic Machinery and Systems, Lausanne, Suisse, September 9-12, 2002, pp. 865-872

[22] International Standard IEC 60041, Field acceptance tests to determine the hydraulic performance of hydraulic turbines, storage pumps and pump-turbines, third edition, 1991-11.

[23] Truckenbrodt, E., Fluidmechanik, Springer Verlag, 4. Auflage in nachgedruckter und veränderter Ausstattung, 2008.

[24] International Standard IEC 60193, Hydraulic turbines, storage pumps and pump-turbines – Model acceptance tests, Second Edition, 1999-11.

[25] Billdal J. T., “The X-factor”, International Water Power and Dam Construction. August 2006.

[26] Demers, A., “Francis Turbine “X-Blade” Technology”,. Hydro News, Magazine of Andritz Hydro. No. 15 / 5-2009.

[27] Brekke, H., Hydraulic Turbines: Design, Erection and Operation, Norwegian University of Science and Technology (NTNU). 2001.